

Potential of millimeter- and  
submillimeter-wave  
satellite observations for  
hydrometeor studies

Inaugural-Dissertation  
zur  
Erlangung des Doktorgrades  
der Mathematisch-Naturwissenschaftlichen Fakultät  
der Universität zu Köln

vorgelegt von  
Mario Mech  
aus Lahr

Köln

2008

Berichtersteller: Prof. Dr. S. Crewell  
Prof. Dr. M. Kerschgens

Tag der mündlichen Prüfung: 20.2.2008

# Abstract

The distribution of hydrometeors is highly variable in space and time, since it is the result of a complex chain of processes with scales from microphysical ( $10^{-6}$  m) to synoptical ( $10^3$  m). It is a challenging task to observe these highly variable atmospheric constituents on a global scale with a temporal and spatial resolution sufficient for numerical weather prediction (NWP) and hydrological purposes. This study investigates the potential of the millimeter- and submillimeter-wavelength range on space-borne sensors for hydrometeor and surface precipitation rate observations. The approach is based on simulations with cloud resolving models (CRMs) coupled to a radiative transfer (RT) model. The simulations are performed for mid-latitude cases covering a broad band of precipitation events such as heavy convective and light stratiform winter precipitation.

Realistic atmospheric conditions were simulated with two mesoscale CRMs: the Mesoscale NonHydrostatic model (Meso-NH) on a 10 km and the COSMO-DE (COntsortium for Small-scale MOdeling-DEutschland) on a 2.8 km horizontal resolution. When calculating brightness temperatures for satellite observations with the one-dimensional radiative transfer model MWMOD (MicroWave MODeL), the detailed cloud microphysics and the three-dimensional fields of temperature, humidity, and pressure of the CRMs are considered in the calculation of the interaction parameters.

The model framework has been evaluated by comparing the simulated brightness temperature fields to observations of the Special Sensor Microwave Imager (SSM/I) as well as to those of the Advanced Microwave Sounding Unit-B (AMSU-B). The results show a good agreement as long as the CRMs capture the atmospheric situation correctly. Consequently, by coupling the radiative transfer model for microwave radiation to CRMs it is possible to evaluate these models through comparison to microwave satellite observations.

Brightness temperatures for frequencies between 50 and 428 GHz at nine observation angles have been simulated for five mid-latitude cases at two time steps. In combination with the vertically integrated hydrometeor contents, these brightness temperature simulations have been used to set up a database. On the basis of this database simple retrieval algorithms have been developed to estimate the potential of the millimeter- and submillimeter-wavelength region for precipitation and hydrometeor observations.

The results show, that especially for snow and graupel, the total column content can be retrieved accurately with relative errors smaller than 20% in stratiform precipitation cases over land and ocean surfaces. The performance for rain water path is similar to the one for graupel and snow in light precipitation cases. For the cases with higher precipitation

amounts, the relative errors for rain water path are larger especially over land. The same behavior can be seen in the surface rain rate retrieval with the difference that the relative errors are doubled in comparison to the rain water path.

Algorithms with a reduced number of frequencies show that window channels at higher frequencies are important for the surface rain rate retrieval. These are sensitive to the scattering in the ice phase related to the rain below. For the frozen hydrometeor retrieval, good results can be achieved by retrieval algorithms based only on frequencies at 150 GHz and above which are suitable for geostationary applications due to their reduced demands concerning the antenna size.

# Zusammenfassung

Die Verteilung von Hydrometeoren ist räumlich und zeitlich sehr variabel, da sie das Ergebnis einer komplexen Prozesskette im Bereich von mikrophysikalischen ( $10^{-6}$  m) bis zu synoptischen ( $10^3$  m) Skalen ist. Die Beobachtung dieser hochgradig variablen Atmosphärenbestandteile auf globaler Skala mit einer für die numerische Wettervorhersage (numerical weather prediction, NWP) und hydrologische Anwendungen ausreichenden zeitlichen und räumlichen Auflösung ist eine große Herausforderung. In der vorliegenden Arbeit wird das Potential von weltraumgestützten Sensoren im Millimeter- und Submillimeter-Wellenlängenbereich zur Beobachtung von Hydrometeoren und Niederschlagsraten untersucht. Hierzu werden Simulationen mit wolkenauflösenden Modellen (cloud resolving models, CRMs) an ein Strahlungsübertragungsmodell (radiative transfer, RT) gekoppelt. Die Simulationen wurden für verschiedene Niederschlagsfälle in den mittleren Breiten durchgeführt. Es wird dabei ein breites Band an Niederschlagsereignissen, wie z. B. starke, konvektive und schwache, stratiforme Winterniederschläge, abgedeckt.

Realistische Atmosphärenzustände wurden mit zwei mesoskaligen CRMs simuliert: Méso-NH (Mesoscale NonHydrostatic model) und COSMO-DE (COntortium for Small-scale MOdeling-DEutschland) mit horizontalen Auflösungen von 10 km bzw. 2,8 km. Zur Berechnung der Helligkeitstemperaturen mit dem eindimensionalen Strahlungstransfermodell MWMOD (MicroWave MODeL) wurden die detaillierte Wolkenmikrophysik sowie die dreidimensionalen Felder der Temperatur, der Feuchtigkeit und des Drucks aus den CRMs in die Berechnung der Interaktionsparameter einbezogen.

Das Modellsystem wurde evaluiert, indem simulierte Helligkeitstemperaturfelder mit Beobachtungen vom Special Sensor Microwave Imager (SSM/I) sowie von der Advanced Microwave Sounding Unit-B (AMSU-B) verglichen werden. Die Ergebnisse stimmen gut überein, solange die CRMs die Atmosphärensituation richtig wiedergeben. Durch die Kopplung des Strahlungsübertragungsmodells an CRMs ist es somit möglich, die Qualität der Wolkenmodelle anhand von Satellitenbeobachtungen im Mikrowellenbereich zu bewerten.

Für fünf Niederschlagsfälle in den mittleren Breiten zu zwei Zeitpunkten wurden Helligkeitstemperaturen für Frequenzen zwischen 50 und 428 GHz für neun Beobachtungswinkel simuliert. Kombiniert mit den vertikal integrierten Hydrometeorgehalten wurde aus den simulierten Helligkeitstemperaturen eine Datenbank erstellt. Basierend auf dieser Datenbank wurden einfache Retrievalalgorithmen entwickelt, um das Potential des Millimeter- und Submillimeter-Wellenlängenbereichs zur Niederschlags- und Hydrometeorbeobachtung abzuschätzen.

Die Ergebnisse zeigen, dass besonders für Schnee und Graupel der Gesamtgehalt gut wiedergewonnen werden kann. Dabei treten relative Fehler unter 20 % für schichtförmige Niederschlagsereignisse über Land- und Meeresoberflächen auf. Die Leistungsfähigkeit bei der Ableitung des Regenwasserpfad es ähnelt der für Graupel und Schnee in Fällen mit leichtem Niederschlag. Für Fälle mit größeren Niederschlagsmengen sind die relativen Fehlern besonders über Land größer. Ein ähnliches Verhalten wird für das Niederschlagsretrieval beobachtet, die relativen Fehler sind jedoch im Vergleich zum Regenwasserpfad doppelt so groß.

Algorithmen mit reduzierter Frequenzanzahl zeigen, dass Fensterkanäle bei höheren Frequenzen wichtig für das Niederschlagsretrieval sind. Diese sind sensitiv auf die Streuung an der Eisphase, die mit dem Niederschlag darunter verbunden ist. Für die Ableitung der gefrorenen Hydrometeore konnten gute Ergebnisse mit Algorithmen erzielt werden, die nur auf Frequenzen von 150 GHz und darüber basieren. Diese sind aufgrund ihres geringen Anspruches bezüglich der Antennengröße für geostationäre Anwendungen geeignet.

# Contents

<b>Abstract</b>	<b>iii</b>
<b>Zusammenfassung</b>	<b>v</b>
<b>1 Introduction</b>	<b>1</b>
1.1 Motivation . . . . .	1
1.2 State of the art . . . . .	4
1.3 Focus of the study . . . . .	9
<b>2 Theory of radiative transfer in the microwave region</b>	<b>11</b>
2.1 Radiative transfer equation . . . . .	11
2.1.1 Terminology . . . . .	11
2.1.2 No absorption, no emission, and no scattering . . . . .	12
2.1.3 Including absorption . . . . .	13
2.1.4 Including absorption and scattering by hydrometeors . . . . .	13
2.1.5 A formal solution for the scalar RTE . . . . .	14
2.2 Polarization and Stokes parameters . . . . .	15
2.3 Gaseous absorption . . . . .	18
2.4 Interaction between hydrometeors and microwaves . . . . .	19
2.4.1 Basic quantities of scattering theory . . . . .	20
2.4.2 Scattering parameter computation - Approximations . . . . .	23
2.5 Boundary conditions . . . . .	30
2.5.1 Land surfaces . . . . .	31
2.5.2 Ocean surfaces . . . . .	31
2.6 Solving the radiative transfer equation . . . . .	32
2.7 Dielectric properties . . . . .	33
2.8 Radiative transfer model MWMOD . . . . .	36
2.9 Sensitivity of simulated brightness temperatures to hydrometeors . . . . .	38
<b>3 Microphysics and CRMs</b>	<b>45</b>
3.1 Microphysics of clouds and precipitation . . . . .	46
3.1.1 Hydrometeors . . . . .	46
3.1.2 Microphysical processes . . . . .	46

3.2	Hydrometeors in CRMs . . . . .	48
3.2.1	Méso-NH . . . . .	50
3.2.2	COSMO-DE . . . . .	52
3.2.3	Comparison of the PSD . . . . .	55
<b>4</b>	<b>Satellite simulator</b>	<b>57</b>
4.1	SynSatMic . . . . .	57
4.2	Adopting simulations to AMSU-B geometry . . . . .	60
4.3	Comparison to SSM/I and AMSU-B observations . . . . .	63
<b>5</b>	<b>Data base for retrieval development</b>	<b>67</b>
5.1	Simulated atmospheric cases . . . . .	67
5.2	Analysis of the hydrometeor contents . . . . .	69
5.3	Frequency selection . . . . .	74
5.4	Database . . . . .	75
5.5	Analysis of simulated brightness temperatures . . . . .	76
<b>6</b>	<b>Retrieval approaches</b>	<b>81</b>
6.1	Retrieval algorithms . . . . .	81
6.2	Mutiple regression . . . . .	83
6.3	Frequencies for GEO . . . . .	84
6.4	Best frequency combination . . . . .	86
6.5	Database coverage . . . . .	87
<b>7</b>	<b>COSMO-DE evaluation by SynSatMic</b>	<b>89</b>
7.1	Case study - stratiform precipitation . . . . .	89
7.2	Case study - convective precipitation . . . . .	95
<b>8</b>	<b>Conclusions and Outlook</b>	<b>101</b>
	<b>Bibliography</b>	<b>106</b>
	<b>Erklärung</b>	<b>120</b>
	<b>Lebenslauf</b>	<b>122</b>

# List of Figures

1.1	The electro-magnetic spectrum with data of wavelength and frequency in a logarithmic representation from 0.1 Hz to $10^{24}$ Hz (©Kuphaldt (2007) <a href="http://www.vias.org/fee/">http://www.vias.org/fee/</a> ) . . . . .	2
2.1	Optical thickness (left) due to H <sub>2</sub> O, O <sub>2</sub> , and total (H <sub>2</sub> O + O <sub>2</sub> ) and atmospheric transmittance (right) due to absorption by H <sub>2</sub> O + O <sub>2</sub> for a typical mid-latitude summer atmosphere as a function of frequency in the microwave region for a space-borne receiver. . . . .	18
2.2	Influence of the ozone line absorption in addition to water vapor and oxygen at higher microwaves. Exemplarily the frequency range between 320 and 440 GHz is shown. . . . .	19
2.3	Size parameter for typical cloud droplets ( $d = 20\mu\text{m}$ ), rain drops ( $1000\mu\text{m}$ ), ice crystals ( $60\mu\text{m}$ ), and graupel/snow particles ( $2000\mu\text{m}$ ) in dependence of the frequency between 1 and 1000 GHz. . . . .	21
2.4	Mie efficiencies calculated with Lorenz-Mie theory for frequencies between 1 and 1000 GHz for typical particles: cloud droplet ( $d = 10\mu\text{m}$ at $10^\circ\text{C}$ , top left), rain drop ( $1000\mu\text{m}$ at $10^\circ\text{C}$ , top right, ice crystal ( $60\mu\text{m}$ at $-20^\circ\text{C}$ , middle left), and graupel/snow particle ( $2000\mu\text{m}$ at $-5^\circ\text{C}$ , middle right). The bottom row shows comparisons of the extinction efficiencies (left) and the single-scattering albedo (right). . . . .	25
2.5	Mie efficiencies and single-scattering albedo calculated with Lorenz-Mie theory for different frequencies (50, 89, 150, and 220 GHz) and different particle types/dielectric properties (see sec.2.7): water droplets (top), ice crystals (middle), and graupel/snow particles as a mixing between pure ice and air (bottom). . . . .	26
2.6	Scattering and absorption efficiencies as a function of the size parameter. The relative errors are given with respect to the Lorenz-Mie reference calculations. The right diagrams were calculated for a higher resolution in size parameter range than in the left diagrams. However, the left diagrams show accuracies up to size parameters of $\sim 15$ . . . . .	28

2.7	Real (left) and imaginary (right) part of the dielectric constants for fresh water, pure ice, snow, and wet snow from top to bottom, respectively. The values were calculated between 50 and 500 GHz with the formulas given in section 2.7. The respective colorbar indicates the temperature variation in degrees Celsius. For the calculation of the constants for snow and wet snow a snow density of $0.2 \text{ gm}^{-3}$ has been assumed. . . . .	35
2.8	Cross section of hydrometeor contents [ $\text{gm}^{-3}$ ] of ice crystals, snow, graupel, cloud water, and rain water (from top to bottom) taken from a cross section through the ELBE case simulated with Méso-NH. . . . .	39
2.9	Jacobians [ $\text{Kg}^{-1}\text{m}^3$ ] for perturbations of the snow content (top) for the frequencies (from top to bottom) 89, 150, and 176.31 GHz. . . . .	41
2.10	As Fig. 2.9 but for graupel. . . . .	42
2.11	As Fig. 2.9 but for rain water content. . . . .	43
3.1	Cloud microphysical processes considered in the COSMO-DE three-category ice scheme as an example for the interacting processes ( <i>Doms et al.</i> , 2004). . . . .	48
3.2	Particle size distribution of snowflakes (top) and graupel particles (bottom) for a mixing ration of $3 \times 10^{-3}$ at 265 K. The red line shows the distribution for the COSMO-DE microphysical scheme with respect to the largest diameter; black lines are with respect to spheres. . . . .	56
4.1	Schematic view of the model framework for SynSatMic and the retrieval database. . . . .	58
4.2	Sensitivity of brightness temperature to increase in number of bins at various frequencies (left) as percentage of the highest resolution. The brightness temperature resulting from the calculations with the highest number of discretization points is assumed to be the most accurate. Increase in computation time in seconds with increasing bin number (right). The calculations were performed with a single layer of snow particles (mixing ratio $q_s = 3 \times 10^{-3}$ ) at 550 hPa and 265 K after the COSMO-DE microphysical scheme. . . . .	59
4.3	Comparison of the particle size distributions for the maximum extension (red) and the water-equivalent diameter (black) following the COSMO-DE parameterization. The dashed lines indicate the the particle size distributions after Eqs.3.1 and 3.12: left side for snowflakes, right side graupel particles. . . . .	60
4.4	Geometry considerations for AMSU satellite observations. $\theta_s$ is the scanning angle, $\alpha$ the angle and $r$ denotes the radius of the field of view, respectively. . . . .	61
4.5	Comparison between SSM/I observations (top) and the Atmospheric radiative Transfer Model (ATM) (bottom) at window frequencies 19, 35, and 85 GHz for the Hoek case (see sec. 5.1). . . . .	64

4.6	Comparison between AMSU-B and Meteosat observations (top) and the Atmospheric radiative Transfer Model (ATM) (bottom) at window frequencies 89 and 150 GHz, as well as the Meteosat infrared channel at $11\ \mu\text{m}$ . . . . .	65
5.1	Overview of the different precipitation cases (bold letters in Tab. 5.1) in terms of surface rain rates (in mm/h) and the respective domains considered in this study. In the UKMIL and ALGER cases, the surface rain rates are shown with a cut off above 20 mm/h for presentation reasons. For statistics of the events see Tab. 5.2. . . . .	70
5.2	Distributions of vertically integrated hydrometeor contents ( $\text{kgm}^{-2}$ ) and precipitation rate ( $\text{mmh}^{-1}$ ) for the different precipitation cases (bold letters in Tab. 5.1). The bin widths of the ice, snow, graupel, cloud liquid water, and rain water contents, and the precipitation rate are 0.05, 0.15, 0.3, 0.1, and $0.2\ \text{kgm}^{-2}$ and $2\ \text{mmh}^{-1}$ , respectively. The very high contents mentioned in Tab. 5.2 were single point simulations and have been omitted in this distributions. . . . .	72
5.3	Mean vertical distributions of the different hydrometeor categories in the troposphere. The contents are shown as mixing ratios [kg/kg]. Averages are calculated only from hydrometeor contents that are not zero. The horizontal thick (thin) line represents the mean (maximum/minimum) altitude of the $0^\circ\text{C}$ isotherm. . . . .	73
5.4	Correlation between the different integrated hydrometeor contents and the surface rain rate for all cases and both time steps. The rightmost columns show the correlation between the frozen hydrometeor contents and the surface rain rate. . . . .	74
5.5	Absorption by water vapor and oxygen in terms of optical thickness. Blue lines show the frequencies between 50 and 428.76 GHz selected for the radiative transfer simulations. . . . .	76
5.6	Horizontal distribution of the simulated brightness temperatures for selected frequencies for the Hoek van Holland case on September 11, 2001 at 18 UTC. The upper row shows simulations for frequencies in the oxygen complex between 50 and 60 GHz, the second row in the oxygen band at 118 GHz, the third row at the window frequencies 89, 150, and 176.31 GHz, and the bottom row at the higher window frequencies 340, 398.2, and 428.76 GHz on the wing of the 424.76 GHz oxygen line. . . . .	77
5.7	Correlation between the simulated brightness temperatures at different frequencies and the integrated hydrometeor contents, as well as the surface rain rate. Land pixels (top), ocean pixels (middle), and all pixels (land and ocean; bottom). . . . .	79

6.1	Relative errors of the retrieval are shown for rain, snow, and graupel water path as well as for the surface rain rate. The relative errors are separated into land, ocean, and all pixels for each single case and time step. Here and in the following figures, the denotation for the cases has been changed: A1 corresponds to ALGER02, A2 to ALGER07, E1 to ELB06, etc.. The columns indicated by <i>All</i> represent the retrieval performance for all cases and time steps merged together. . . . .	84
6.2	Comparison of the performance in terms of relative errors between hydrometeor retrievals including all frequencies and the one based on algorithms including only frequencies at 150 GHz and above for land and ocean surface types together. For the denotation of the cases see Fig. 6.1. . . . .	85
6.3	Tests of the representativeness of the database for rain water path, graupel water path, snow water path, and surface rain rate are shown. Dev1, Dev2, Dev3, Dev4, and Dev5 are the training datasets for the retrieval development built by excluding the case shown rightward of each development dataset. The resulting coefficients are applied to retrieve the amounts of the actual quantities of the excluded case. The performance of the retrievals is shown in terms of relative errors. For the Algiers flood case, the relative errors are truncated. . . . .	88
7.1	Vertically integrated water categories (water vapor, cloud water, ice crystals, graupel, snow, and rain) in [ $\text{kgm}^{-2}$ ] for August 3, 2006 simulated with COSMO-DE at 11 UTC for a run initialized at 00 UTC. . . . .	90
7.2	AMSU-B observation (left) and SynSatMic simulation (right) for 150 GHz on August 3, 2006 at 11 UTC. . . . .	93
7.3	Brightness temperature distribution for 150 GHz on August 3, 2006 at 11 UTC separated into ocean and land pixels: AMSU-B observation (magenta) and SynSatMic simulation (blue). . . . .	93
7.4	Same as Fig. 7.2 but for 182.31 GHz. . . . .	94
7.5	Same as Fig. 7.3 but for 182.31 GHz. . . . .	94
7.6	Vertically integrated water categories (water vapor, cloud water, ice crystals, graupel, snow, and rain) in [ $\text{kgm}^{-2}$ ] for August 28, 2006 simulated with COSMO-DE as an 14 hour forecast valid for 14 UTC. . . . .	97
7.7	AMSU-B observation (left) and SynSatMic simulation (right) for 89 GHz on August 28, 2006 at 14 UTC. . . . .	98
7.8	Brightness temperature distribution for 89 GHz on August 28, 2006 at 14 UTC separated into ocean and land pixels: AMSU-B observation (pink) and SynSatMic simulation (blue). . . . .	98
7.9	Same as Fig. 7.7 but for 176.31 GHz. . . . .	99
7.10	Same as Fig. 7.8 but for 176.31 GHz. . . . .	99

# List of Tables

2.1	Softness parameters (SP) for the calculation of the equal-sphere diameter to derive the scattering cross section $\sigma_{sca}$ . The SP are averaged over different shapes of the corresponding particles. . . . .	30
3.1	Parameters of the PSD of the Méso-NH microphysical scheme after <i>Caniaux et al.</i> (1994). . . . .	52
3.2	Parameters of the PSD of the COSMO-DE microphysical scheme after <i>Doms et al.</i> (2004) with $a_m^h$ in $\text{kgm}^{-b}$ being a particle specific form factor and $\rho_w$ the bulk density for water. . . . .	54
5.1	Overview of the different cases considered for the database of mid-latitude precipitation events. Output times written in bold letters have been used in Figs. 5.1 and 5.2 for the surface rain rate and hydrometeor statistics. . . . .	68
5.2	Hydrometeor statistics for all cases: maximum precipitation rate ( $i_{\max}$ ), mean precipitation rate ( $\langle i \rangle$ ) only for pixels with precipitation and percentage of profiles with precipitation ( $f_i$ in %) of type $i$ , where $i$ is rain <R>, graupel <G>, and snow <S>. Output times written in bold letters have been used in Figs. 5.1 and 5.2. . . . .	71
5.3	List of frequencies considered for the database between 50 and 428.76 GHz relevant for planned satellite missions. . . . .	75
6.1	Performance of the rain water path, and rain rate retrieval in terms of correlations, relative errors, and root mean square error (RMS) for a combination of the five frequencies resulting in the lowest relative error and for a retrieval based on all frequencies. The five frequencies are sorted according to their importance beginning with the most important one. . . . .	86



# Chapter 1

## Introduction

### 1.1 Motivation

From a simple point of view hydrometeors are just collections of water molecules in the atmosphere. However their formation is one of the most complex processes of the atmospheric water cycle.

In more detail, hydrometeors are a product of condensation or deposition of atmospheric water vapor, whether formed in the free atmosphere or at the earth's surface. A large number of different hydrometeor types exists that may be classified in different ways. *Glickman* (2000) categorizes them into: 1) liquid or solid water particles formed and remaining suspended in the air, for example, damp (high relative humidity), haze, cloud, fog, ice fog, and mist; 2) liquid precipitation, for example, drizzle and rain; 3) freezing precipitation, for example, freezing drizzle and freezing rain; 4) solid (frozen) precipitation, for example, snow, hail, ice pellets, snow pellets (soft hail, graupel), snow grains, and ice crystals; 5) falling particles that evaporate before reaching the ground, for example, virga; 6) liquid or solid water particles lifted by the wind from the earth's surface, for example, drifting snow, blowing snow, and blowing spray. Depending on temperature, vertical velocity, available water vapor, and condensation nuclei, different formation processes can occur resulting in the various hydrometeor types with different phases, sizes, shapes, and life times. While the processes of formation are influenced by a large number of variables, and are therefore very complex, the question of whether or not a hydrometeor is falling down can be reduced to the relation between the particles buoyancy and its weight. On its way towards the earth's surface, a particle can grow or shrink by different processes (collision with other particles, evaporation, melting, ...). Thus it is not easy to answer the question, whether the precipitation reaches the earth's surface and contributes to the surface precipitation rate.

This complex chain of processes to form hydrometeors and eventually to generate precipitation implicates that the precipitation at the ground and the hydrometeors in the atmosphere have a high variability in space and time. Therefore, to fulfill the needs for precipitation observation with a sufficient temporal and spatial resolution for applications,

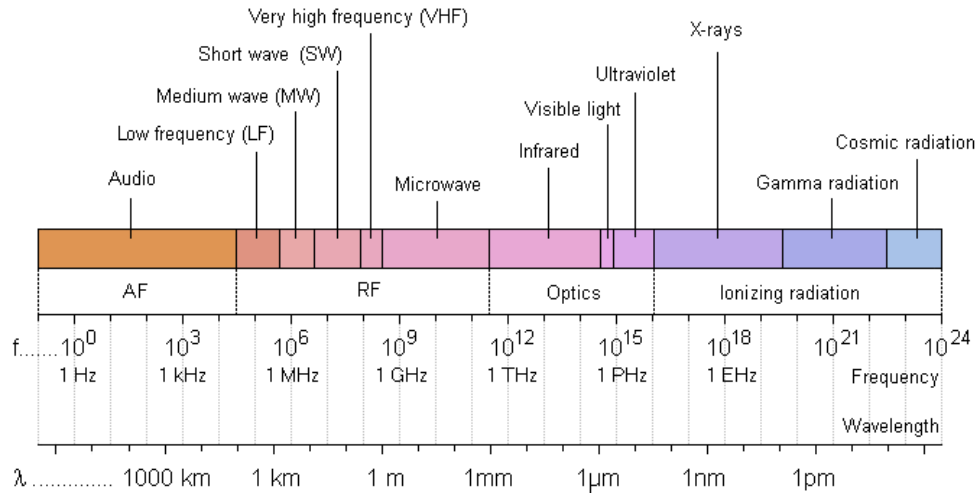


Figure 1.1: The electro-magnetic spectrum with data of wavelength and frequency in a logarithmic representation from 0.1 Hz to  $10^{24}$  Hz (©Kuphaldt (2007) <http://www.vias.org/feee/>)

like numerical weather prediction (NWP), now-casting (NWC), or hydrological purposes, is a challenging task (Rizzi *et al.*, 2006).

The first precipitation observation systems, that were used to provide routinely long-term measurements of precipitation, are rain gauges. These measure precipitation at single points, mostly as accumulated daily sums. Unfortunately, only few online rain gauges are operational. Most rain gauges must be operated by man power resulting in an unsatisfactory coverage, especially over ocean and in sparse inhabited areas (Huffman *et al.*, 1997).

In well-developed countries, ground-based radar networks provide precipitation observations with a temporal resolution of about five minutes over large areas with high spatial resolution. However, due to many error factors involved in the measurement process, a homogeneous quality radar precipitation composite will not be available in the near future, even for Europe.

Due to their geostationary orbits, space-borne observation systems in the visible (VIS) and infrared (IR) wavelength range provide a good temporal and areal coverage with an acceptable spatial resolution. Since clouds and precipitation are opaque at these high frequencies, observations in the VIS and IR wavelength range only provide information about the upper boundary of cloud and precipitation systems (Levizzani *et al.*, 2001). Therefore, it is almost impossible to conclude on the precipitation at the ground or even more on the hydrometeor profiles.

By applying frequencies in the microwave region, defined as the electro-magnetic radiation with wavelengths between 1 mm and 1 cm (frequencies between 0.3 and 300 GHz, see Fig. 1.1), a more complete view of the vertical structure of the atmosphere can be gained. Especially space-borne systems operating in the lower microwave region (below 40 GHz) on

low Earth orbits (LEO,  $h \approx 833$  km) can penetrate clouds and atmospheric water vapor. Established sensors in this frequency range are the TRMM (Tropical Rainfall Microwave Mission) Microwave Imager (TMI) (*Kummerow et al.*, 1998) and the conical scanning (constant observation angle of  $53^\circ$ ) Special Sensor Microwave Imager (SSM/I) (*Hollinger et al.*, 1987) flown on the Defense Meteorological Satellite Program (DMSP). The latter one is in use for operational data assimilation of precipitation at the European Center for Medium Range Weather Forecast (ECMWF) (*Bauer et al.*, 2006) and at the United Kingdom’s national weather service (Met Office). Another prominent sensor in the lower microwave region is the Advanced Microwave Sounding Unit-A (AMSU-A) (*Robel*, 2006) operating on the National Oceanic and Atmospheric Administration (NOAA) satellites NOAA-15 to -17. It is a cross-track scanning instrument (observation angles between  $-48^\circ$  and  $+48^\circ$ ) used for global temperature profiling. Although these techniques can provide direct information about the precipitation, they have some disadvantages, making them not feasible for many NWP and hydrological applications. Their orbits have no rapid revisiting times and the applied frequencies can not provide high horizontal resolutions. Furthermore, due to their measurement principles, based on the emission differences between radiatively cold ocean and warm precipitation, they are only applicable over sea surfaces.

Microwave sensors with higher frequencies like the 85.5 GHz channel of SSM/I, the 89 GHz channel of AMSU-A, or the AMSU-B sensor on NOAA 15-17 with frequencies between 89 and 182.31 GHz, already operating in LEO, provide advantages compared to the lower microwave ranges: clouds are still partially transparent and due to the reduced influence of the surface through increased water vapor continuum absorption, they can be used for precipitation retrieval over land and ocean (*Ferraro et al.*, 2000). Moreover, by applying higher frequencies at same antenna sizes the horizontal resolution can be increased<sup>1</sup>. But by their low orbit heights, the time between two consecutive overpasses over one specific location is large for NWP or hydrological purposes (three to six hours with three operational AMSU-B sensors). Furthermore, at higher microwave frequencies the composition of signal retrieved by a space-borne sensor is rather complex: the radiance is emitted by the precipitation within and underneath the cloud and scattered at the frozen particles in the upper parts of the cloud system.

The problem of the low revisiting frequency could be avoided by observations from geostationary orbits (GEO,  $h \approx 36000$  km). But with feasible antenna sizes of 3-4 m, the horizontal resolution for the highest AMUS-B frequency would decrease to 24-18 km. To achieve precipitation observations with spatial resolutions in the order of current forecast models, the simplest solution would be to equip satellites on GEO with larger antennas. Since the costs of satellites are driven by the size of their antennas for diameters larger than 3 m, this approach would not be affordable. Therefore, frequencies with wavelengths in the submillimeter range (above 300 GHz, see Fig. 1.1) are worthwhile to be considered for the operation on future GEO satellites, given the typical antenna sizes.

---

<sup>1</sup>The relationship between horizontal resolution often measured by the half-power beamwidth (HPBW)  $\theta_{\text{HPBW}}$ , applied wavelength  $\lambda$  and antenna diameter  $D$  in microwave remote sensing can be approximated with 10% accuracy to  $\theta_{\text{HPBW}} = 1.5\lambda/D$ , (e.g. *Janssen*, 1993, chap. 1.3)

The major problem for precipitation retrievals based on observations in the higher frequency range, is to understand the afore mentioned indirect signal received from the precipitation due to the increased scattering at the frozen particles aloft. Since only few measurements by aircrafts are available at these high frequencies, only intensive modeling of the relationship between cloud ice and precipitation at submillimeter-wavelengths can help to identify the information content of observations at these frequencies (*Bizzarri, B. et al., 2005*).

The main objective of this thesis is to asses the potential of satellite based observations with passive sensors in the millimeter- and submillimeter-wavelength region for hydrometeor observations for the mid-latitudes. Much effort has been put so far in the precipitation retrieval development for tropical regions where precipitation is generated in warm clouds. In the mid-latitudes, most precipitation is generated through the ice phase making the precipitation retrieval development much more complex. The key to solve this problem is the understanding of the relationship between cloud ice and precipitation at higher microwave frequencies. Therefore, combined cloud resolving model (CRM) and radiative transfer simulations will be performed, resulting in a database of simulated brightness temperatures with corresponding hydrometeor profiles usable for retrieval algorithm development. The coupled model approach serves as a satellite simulator for the microwave range that is used as an evaluation tool for the quality of microphysical schemes in CRMs, by comparing the resulting brightness temperature fields to satellite observations.

The following section will give an overview of recent related research activities before outlining the strategy of this study in the last section of this chapter.

## 1.2 State of the art

The history of microwave remote sensing of precipitation with satellites can be tracked back to the early 70's, where the polar-orbiting Nimbus-5 satellite with the Electrically Scanning Microwave Radiometer (ESMR) on board has been launched. Equipped with a sensor at 19.35 GHz, it was the first time that observations with frequencies became available, that could penetrate water vapor and clouds, but were still sensitive to atmospheric liquid water. The first work by *Wilheit et al. (1977)* utilizing this frequency band for precipitation retrieval achieved promising results.

First dual polarizing sensors at 18 GHz and 37 GHz usable for precipitation retrieval became available on the following Nimbus satellites ESMR (only 37 GHz on Nimbus-6, 1975) and on the successor instrument SMMR (Scanning Multichannel Microwave Radiometer on Nimbus-7, 1978).

In the following years, the interest of microwave remote sensing primarily focused on remote sensing of meteorological surface data beside precipitation. This changed when the conical Special Sensor Microwave Imager (SSM/I; *Hollinger et al., 1987*) on board the F-8 satellite of the Defence Meteorological Satellite Program (DMSP) became operational. On SSM/I, the center frequencies are 19.35(v+h), 22.235(v), 37.0(v+h), and 85.5(v+h) GHz (v and h indicates vertical and horizontal polarization, respectively). Algorithms for re-

trieving precipitation rates over ocean are based on the brightness temperature increase through emission by the precipitation layer over the radiatively cold ocean. Therefore, the SSM/I frequencies below 40 GHz (e.g. *Prabhakara et al.*, 1992) are used. By including scattering signals at 85.5 GHz precipitation retrieval became even possible over land (*Grody*, 1991). The rainfall products derived from SSM/I are widely used for a variety of applications ranging from short-term rainfall potential assessment (*Ferraro*, 1997; *Ferraro et al.*, 2002) to global, monthly monitoring. Thereby, monthly rainfall rates derived from SSM/I brightness temperature measurements show correlations in excess of 0.8 with rain gauge measurements for the tropics and summer seasons of the mid-latitudes and over land. The root mean square (RMS) errors are typically 75% of the mean rainfall with a slight positive bias (*Ferraro*, 1997). The results are worse for high-latitudes and transition seasons. Over ocean, the correlations are similar but with a RMS of 50% and a small negative bias.

The AMSU-A (15 frequencies up to 90 GHz) and -B (89.0, 150.0, 176.31, 180.31, and 182.31 GHz) sensors on the NOAA satellites became operational in 1998. Since that time many studies investigating the impact of hydrometeors on passive microwaves focus on their frequency bands, although the sensors were primarily design for temperature and humidity profiling (e.g. *Chen and Staelin*, 2003; *Ferraro et al.*, 2000; *McCollum and Ferraro*, 2003). *Bennartz and Bauer* (2003) performed simulations at 85, 150, and 183 GHz for three different mid-latitude precipitation events to investigate the response of the brightness temperature to variations in hydrometeor contents and surface emissivities. They found that the 150 GHz channel exhibits the most influence by ice particle scattering. Sounding channels in the H<sub>2</sub>O absorption band around 183.31 GHz are strongly affected by the water vapor in and above the cloud, whereas the brightness temperatures observed in channels around 85 GHz are much more sensitive to variations in the surface emission. They suggest that combinations of 85, 150, and 183.31-7 GHz are most appropriate for observing precipitation in mid- to high-latitudes.

In preparation for the European contribution to the Global Precipitation Mission (EGPM; *Mugnai*, 2003), *Bauer and Mugnai* (2003) and *Bauer et al.* (2005) investigated retrieval errors of cloud and precipitating hydrometeor contents from space-borne observations for microwave frequencies. In their study, channels in atmospheric windows between 18 and 150 GHz and in oxygen absorption complexes near 50-60 and 118 GHz were examined by performing radiative transfer simulations on ECMWF short-range forecasts. They found that algorithms applying sounding channels in the oxygen bands at 60 and 118 GHz show much more stable results for the retrieval of rain-, snow-, and cloud water profiles especially over land than algorithms based on single window channels.

The major limitation with passive microwave instruments on geostationary orbits is the difficulty in reaching acceptable spatial resolution with reasonable antenna sizes. The use of higher frequencies makes it possible to reduce the antenna aperture for a given size. The National Space Agency (NASA-NOAA) Geosynchronous Microwave Sounder Working Group developed the project of a submillimeter-wavelength GEosynchronous Microwave sounder and imager (GEM) equipped with a 2 m scanning antenna, with channels in the oxygen bands (54, 118, and 425 GHz) and in the water vapor lines (183 and 340/380 GHz)

(*Staelin et al.*, 1998). The Geostationary Observatory for Microwave Atmospheric Sounding (GOMAS) project was also proposed recently to the European Space Agency (ESA) as a Next Earth Explorer core mission with similar channels but a 3 m antenna, providing a spatial resolution of 20 km at 220 GHz (*Bizzarri, B. et al.*, 2005). These satellite projects recognize the importance of millimeter- and submillimeter-wavelength observations for cloud and precipitation characterization from geosynchronous orbits.

In response to a 2002 NASA Research Announcement calling for proposals to develop technologies to enable new observational capabilities from geostationary orbits, the Geostationary Synthetic Thinned Aperture Radiometer (GeoSTAR) was proposed by *Tanner et al.* (2004) and *Lambrigsten et al.* (2004). GeoSTAR synthesizes a large aperture to provide high spatial resolutions from GEO. By such antenna concepts, it would be possible to achieve spatial resolutions around 50 km at 50 GHz requiring a 4 m antenna from GEO. This is similar to common antennas but with the advantage of observing the whole disk from GEO and no limitation in aperture size. Thus technically any resolution would be possible (for example 10 km at 183 GHz with three sticks of 4 m equipped with 600 sensors). As a disadvantage it can be considered that by a single synthesized aperture only one frequency band can be observed. Furthermore the calibration of such a complex systems is computationally expensive *Tanner et al.* (2007).

Observations in the submillimeter range (above 300 GHz) have been of more and more interest in the recent years. On the one hand, higher frequencies could significantly increase the poor spatial resolution. On the other hand, the higher the frequency the more sensitive they are to the ice phase of the atmospheric water cycle, an effect very interesting for cirrus observations (*Bühler et al.*, 2005a). Unfortunately, not many instruments and therefore measurements for retrieval development are available in this frequency range. The few datasets that are available were collected by airborne based instruments. The Millimeter-wave Imaging Radiometer (MIR; *Racette et al.*, 1996; *Wang et al.*, 2001) with four channels from 89 to 340 GHz and the Compact Scanning Sub-millimeter Imaging Radiometer (CoSSIR; *Evans et al.*, 2005) with twelve frequencies between 183 and 640 GHz are both designed for determining ice water path (IWP) and particle size in upper-tropospheric ice clouds. Retrieval studies based on the data collected with the CoSSIR instrument during the Cirrus Regional Study of Tropical Anvils and Cirrus Layers Florida Area Cirrus Experiment CRYSTAL-FACE campaign showed good results for retrievals of the integrated IWP based on the lower channels. Although the submillimeter-wave channels (380, 487, and 640 GHz) were noisier than anticipated, the CoSSIR data demonstrated the high (*Evans et al.*, 2003; *Evans et al.*, 2005) sensitivity of the submillimeter channels to ice cloud particles as compared with the lower frequencies.

Due to the sparse data availability above 190 GHz for precipitating cases, retrieval studies can only be conducted on the basis of simulated datasets. This is often done by the so called model-to-satellite approach where radiative transfer simulations are performed on detailed CRM outputs to simulated brightness temperature observations. Such datasets have already been successfully created for older satellite missions like TRMM launched in 1997. Thereby a dataset of simulated brightness temperatures for tropical cases has been developed at TRMM-TMI frequencies from 10 to 85 GHz based on detailed mesoscale

cloud model outputs. Many TRMM rainfall algorithms are related to this dataset named GPROF (Goddard PROFiling; *Kummerow et al.*, 2001). Recently, *Crewell et al.* (2005) and *Prigent et al.* (2005) created a database of brightness temperatures (from 50 to 425 GHz) with corresponding hydrometeor profiles for mid-latitude precipitating cases (*Chaboureaud et al.*, 2007) to estimate the potential of the millimeter- and submillimeter-wavelength range. They reported a high potential especially for the retrieval of integrated snow and graupel contents (*Mech et al.*, 2007).

A similar work like the study presented herein was performed by *Defer et al.* (2007). Within a coupled model framework between mesoscale cloud modeling and a radiative transfer model, millimeter- and submillimeter-wavelengths between 23.8 and 875 GHz were investigated for their use for rain detection and rain rate retrieval from geostationary sensors. They found that combinations of frequencies in this range satisfy the requirements of NWC and NWP.

Since the millimeter and submillimeter observations are not expected to sense directly the precipitation close to the ground but more the scattering in the upper parts of the cloud systems, detailed knowledge about the relationship between the cloud microphysics and the precipitation down below is important. This requires the simulation of the atmospheric state with state-of-the-art mesoscale CRMs (*Lafore et al.*, 1998; *Doms and Schättler*, 2002). Several research studies (*Evans et al.*, 1995; *McCumber et al.*, 1991) indicated, that microphysical schemes with five hydrometeor phases adequately represent the atmospheric state for the standpoint of passive microwave signatures. The five hydrometeor phases are generally classified as bulk amounts of cloud water, rain water, cloud ice, snow (or ice aggregates), and graupel (including hail).

A key factor in the simulation of millimeter- and submillimeter-wave brightness temperatures is the knowledge of the influence of cloud microphysical properties and their parameterizations on the radiation at microwave frequencies. Therefore, this topic has been investigated by many authors. *Skofronick-Jackson et al.* (2002) studied the sensitivity of computed microwave brightness temperatures to changes in the microphysical parameters by using six microphysical cloud parameterizations with respect to changes in hydrometeor size parameters and frozen particle ice-air-water ratios. The comparisons generally showed that increasing the weight of water or rain enhances the brightness temperatures and that cooling at higher frequencies (220 GHz) arises when using parameterizations producing larger ice concentrations.

The impact on microwave brightness temperatures of assumptions made about the ice microphysics has been investigated by *Doherty et al.* (2007). They compared the different treatment of ice microphysics by varying the assumptions about the ice density and particle size distribution shape at AMSU-B frequencies with two radiative transfer models (Radiative Transfer for the Television infrared observation satellite Operational Vertical Sounder (TOVS) (RTTOV; *Saunders et al.*, 1999) and the Atmospheric Radiative Transfer System (ARTS; *Bühler et al.*, 2005a)). They found that an approach based on a combination of a size-dependent density and cloud temperature dependent size distributions and ice water content give the best results for a frontal winter storm with heavy precipitation over the UK.

*Seo and Biggerstaff* (2006) examined the impact of different microphysical schemes on the retrieval of cloud properties based on passive microwave observations using three-dimensional, non-hydrostatic, adaptive-grid cloud models. They concluded that the uncertainty in the surface rain rate retrieval does not depend on the microphysical scheme except for stratiform cases. In contrast, the uncertainty in the retrievals differs significantly for the bulk water quantities for cloud water, cloud ice, and snow and the latent heating. This is caused by the systematic differences in the treatment of bulk quantities between the parameterization schemes together with the low correlation between those properties and the passive microwave brightness temperature.

The higher the considered frequencies, the higher is the influence of the different shapes of the ice particles on the scattering signatures. Since the calculation of the scattering parameters is not only a matter of accuracy but also of computation time, a lot of effort has been put into the field of approximating the scattering properties. By the Discrete Dipole Approximation (DDA; *Draine and Flatau*, 2000) and the T-matrix approach (*Mishchenko et al.*, 1996) methods exist that allow directly the calculation of scattering properties for non-spherical particles. Thereby a more accurate description of the particles is possible with the DDA with a lack in computational efficiency. Since computer power is still limited and calculations often need to be performed for many profiles, it is desirable to solve the scattering problem at non-spherical particles analytically by applying the Lorenz-Mie theory. Therefore the non-spherical shape is included by parameterizations modifying the size or the density (*Bennartz and Petty*, 2001; *Liu*, 2004; *Kim et al.*, 2007). Brightness temperatures achieved with radiative transfer simulations based on such approximations showed improved agreement with satellite observations at AMSU-B frequencies (*Meirolid-Mautner et al.*, 2007; *Kim et al.*, 2007).

The author of this thesis has contributed to the state-of-the-art in this research area by the following studies:

- Within the EUMETSAT funded study for the Meteosat Third Generation (MTG) "Simulation study of precipitating clouds from geostationary orbits with passive microwaves" by *Crewell et al.* (2005) the basic coupling of the models and the database development has been performed, together with first potential analyses,
- within the ESA-ESTEC project "Development of an radiative transfer model for the frequency range between 200 and 1000 GHz" by *Sreerekha et al.* (2005) a single-scattering database for the DDA has been created and included into the ARTS radiative transfer model,
- in *Chaboureau et al.* (2007) the atmospheric cases simulated with Méso-NH are described in more detail,
- by *Meirolid-Mautner et al.* (2007) the quality of the simulated brightness temperature fields are evaluated,
- and by *Mech et al.* (2007) the information content of the millimeter-wavelength range for hydrometeor retrieval is investigated.

## 1.3 Focus of the study

The last section revealed, that precipitation observations over large areas with high temporal resolution should in principle be possible with geostationary satellite observations. Because current technology limits the satellite antenna to about 3 m, the low microwave frequencies used on polar orbiters for precipitation observations would lead to large, unacceptable footprints ( $> 50$  km). In order to achieve a sufficient horizontal resolution for future hydrological and meteorological applications, higher microwave frequencies could be used. For example, the horizontal resolution achievable with receivers on a GEO satellite at a frequency of 183 GHz is 24 km, at 380 GHz 12 km, and at 425 GHz 10 km.

As preparation for such future satellite missions, the potential for hydrometeor retrieval from observations in the millimeter- and submillimeter-wavelength region is investigated. Therefore, realistic simulations with CRMs combined with radiative transfer calculations for relevant frequencies are performed. Such calculations have not been carried out for the mid-latitudes so far by other authors. Their studies concentrating on the mid- to high-latitudes used models with coarser resolution and less detailed cloud microphysics (*Bauer et al.*, 2005). Hence, the created database consisting of hydrometeor profiles together with simulated brightness temperatures for the mid-latitudes is unique. Based on this database, the potential that higher millimeter-waves provide for hydrometeor observations in the mid-latitudes is investigated by developing simple retrieval approaches.

The second point the study is focussing on is the possibility of evaluating CRM outputs by satellite observations in the passive microwave region. Therefore the framework consisting of CRM output and radiative transfer simulations has been extended by a post-processor to convolute the simulated brightness temperatures with satellite observation geometries and antenna pattern functions.

In chapter 2, the basic ideas of radiative transfer in the microwave region along with the sensitivity of the main interaction parameters will be presented as the basis of the MicroWave MODel (MWMOD). Chapter 3 reveals the microphysical schemes and the parameterizations of the particle size distributions (PSDs) for the five hydrometeor categories implemented within the applied CRMs Méso-NH (Mesoscale Non-Hydrostic model) and COSMO-DE (COnsortium for Small-scale MOdeling-DEutschland). The Synthetic Satellite simulator for the Microwave range (SynSatMic) will be introduced in chapter 4. Chapter 5 will give a description and an analysis of the database consisting of five simulations of precipitating cases at two time steps for the mid-latitudes and the corresponding simulated brightness temperatures at 18 millimeter and submillimeter frequencies. Results of simple retrieval approaches to estimate the potential of this frequency range are shown in chapter 6. After demonstrating the usage of SynSatMic as an evaluation tool for CRMs (chap. 7), a conclusions is given in the final chapter 8 of this thesis.



# Chapter 2

## Theory of radiative transfer in the microwave region

The propagation of electro-magnetic energy through the atmosphere is described by the vector radiative transfer equation (VRTE). This equation describes how the radiant intensity is modified by emission and extinction processes while traversing the medium. The extinction processes can thereby be separated into parts for the reduction of the radiant energy by absorption and parts for the redistribution by scattering. Especially the scattering processes in the higher microwave region at hydrometeors with dimensions in the range of the wavelength can be very complex; the particle shape and orientation have a non-negligible influence on the scattering properties. The individual parts of the VRTE and their impact on the radiance or brightness temperature at a given location are shortly discussed in this chapter. Before the radiative transfer model applied in this study is presented, a short discussion on various methods for the scattering calculations is given. In a final section the sensitivity of the simulated brightness temperatures to different hydrometeors influencing the radiative transfer is investigated. Throughout this thesis  $\nu$ , the frequency in GHz, is used as the unit to describe electro-magnetic wave characteristics. The theory presented here is mainly drawn from the recent comprehensive review *Thermal microwave radiation: Applications for remote sensing* by Mätzler (2006) and the meteorological training course lecture series by ECMWF *Introduction to microwave radiative transfer* by Bauer (2002). Detailed derivations related to some concepts discussed here can also be found in these and therein cited references.

### 2.1 Radiative transfer equation

#### 2.1.1 Terminology

In general, when considering radiative transfer in the atmosphere, the radiation is expressed by the spectral radiance: it is the amount of light passing through or emitted by a particular (unit) area within a solid angle and has the units  $\text{Wm}^{-2}\text{sr}^{-1}\text{s}$ . For thermal radiation, it

is common to transform radiant intensities into brightness temperatures  $T_b = T$ ; i.e. the temperature  $T$  related to the thermal radiation with the radiance  $I_\nu$  defined by the Planck's law  $B_\nu$ :

$$I_\nu = B_\nu(T) = \frac{2h\nu^3}{c^2(\exp(h\nu/k_bT) - 1)}. \quad (2.1)$$

where  $h = 6.62607 \times 10^{-34}$  Js is the Planck constant,  $k_b = 1.38065 \times 10^{-23}$  J/K is the Boltzmann constant and  $c = c_0/n'$  the phase velocity with  $n'$  as the real part of the complex refractive index,  $c_0 = 2.997925 \times 10^8$  m/s the speed of light in vacuum. Since natural bodies are seldom black bodies (emissivity  $\epsilon = 1$ ), the brightness temperature  $T_b$  is defined as the temperature a blackbody must have to exactly emit the intensity  $I$ ,

$$T_b = B^{-1}(I). \quad (2.2)$$

An approximation often used in microwave radiometry is the Rayleigh-Jeans approximation

$$B_\nu = \frac{2k_bT\nu^2}{c^2}, \quad (2.3)$$

adaptive in situations where  $h\nu/k_bT \ll 1$ . This condition is valid in almost the whole microwave region with typical temperatures in the lower atmosphere. Through this approximation, a linearity between radiance and brightness temperature is achieved.

The complex refractive index  $n$  is a position dependent quantity of a medium

$$n = n' + in'', \quad (2.4)$$

where the real part  $n'$  is a measure for the relative speed ( $n' = c_0/c$ ) of an electromagnetic wave in a medium. The imaginary part  $n''$  describes the intensity of interaction in terms of absorption of an electro-magnetic wave traversing the medium. Both quantities are frequency dependent.

### 2.1.2 No absorption, no emission, and no scattering

For a ray of light propagating through a medium along the path  $s$  without absorption (this implies the refractive index  $n = n'$  being real) and scattering, the quantity

$$I_{1\nu} := \frac{I_\nu}{n'^2} \quad (2.5)$$

would be a constant along the propagation path  $s$ . The specific intensity  $I_\nu$  changes as a result of variations in the refractive index, but  $I_{1\nu}$  is conserved (To simplify matters, the index 1 will be omitted throughout the following discussion).

### 2.1.3 Including absorption

If absorption and emission, respectively due to Kirchoff's law, occur, while a pencil of radiation is traversing a medium, it will be weakened and intensified by interacting with the medium. Through the imaginary part the position dependent absorption coefficient

$$\gamma_a = 2k \cdot n'' , \quad (2.6)$$

with units  $\text{m}^{-1}$  can be defined, where  $k = 2\pi\nu/c$  is the wave number. Using this absorption coefficient the reduction of radiant intensity  $I_\nu$  over an infinitesimal step  $ds$  is

$$\frac{dI_\nu(s)}{ds} = -\gamma_a(s)I_\nu(s) \quad (2.7)$$

and, by applying Kirchoff's law of thermal radiation (absorption and emission are in local equilibrium), the intensification through emission is

$$\frac{dI_\nu(s)}{ds} = \gamma_a(s)B_\nu(s) \quad (2.8)$$

with  $B_\nu$  as the normalized Planck function defined by Eqs. 2.1 and 2.5. The emitted radiance defined through  $B_\nu$  is dependent on the physical temperature  $T(s)$ . By combining Eqs. 2.7 and 2.8 and by using the Rayleigh-Jeans approximation (Eq. 2.3), i.e. the linearity between  $I_\nu$  and  $T_b$ , the radiative transfer equation (RTE) including absorption and emission common for microwave radiometry in terms of brightness temperature

$$\frac{dT_b}{ds} = \gamma_a(s)(T(s) - T_b(s)) \quad (2.9)$$

is achieved.

### 2.1.4 Including absorption and scattering by hydrometeors

Up to this point the RTE (Eq. 2.9) only contains losses and gains through absorption and emission by atmospheric gases. If hydrometeors are present in the ray path of light, the parameter describing the weakening of intensity is the extinction coefficient

$$\gamma_e = \gamma_a + \gamma_s . \quad (2.10)$$

It is the sum of the absorption coefficient ( $\gamma_a$ ), related to gases and hydrometeors, and the scattering coefficient ( $\gamma_s$ ), which is characteristic for the interacting medium and dependent on environmental parameters. The ratio between scattering and extinction coefficient is defined as the single-scattering albedo

$$\varpi_0 = \frac{\gamma_s}{\gamma_e}, \quad (2.11)$$

giving a measure for the fraction of scattered radiation, while  $(1 - \varpi_0)$  is the fraction of absorbed (emitted) radiation.

The source term for intensification of radiation is now

$$\varepsilon_\nu(s) = \gamma_a(s) \cdot B_\nu(s) + \frac{\gamma_e(s)}{4\pi} \int_{4\pi} p(\theta, \phi, \theta', \phi') \cdot I_\nu(s, \theta', \phi') \cdot d\Omega', \quad (2.12)$$

the sum of the emission by the hydrometeors (first term) and the radiation scattered into the ray path (second term). The integral in the second term contains the normalized radiance  $I_\nu$  at path position  $s$  propagating in all directions, as defined by the spherical coordinates  $(\theta', \phi')$ , integrated over the whole ( $4\pi$ ) solid angle  $\Omega = (\theta, \phi)$ . The so-called phase function  $p(\theta, \phi, \theta', \phi')$  describes the transfer of radiance from direction  $(\theta', \phi')$  to the direction  $(\theta, \phi)$  of the considered propagation path.

Using the expression for the sources (Eq. 2.12) and the coefficient for the losses through extinction (Eq. 2.10) the basic RTE (Eq. 2.9) can be extended to

$$\frac{dI_\nu(s)}{ds} = -\gamma_e(s) \cdot I_\nu(s) + \gamma_a \cdot B_\nu(s) + \frac{\gamma_e(s)}{4\pi} \int_{4\pi} p(\theta, \phi, \theta', \phi') \cdot I_\nu(s, \theta', \phi') \cdot d\Omega'. \quad (2.13)$$

As shown in subsection 2.1.3 the intensity  $I_\nu$  can be expressed by the brightness temperature  $T_b$  following the Rayleigh-Jeans approximation and the blackbody emission  $B_\nu$  through  $T$ . If the frequency index  $\nu$  is omitted, Eq. 2.13 can be written in a manner more common in the microwave radiative transfer

$$\frac{dT_b(s)}{ds} = -\gamma_e(s) \cdot T_b(s) + \gamma_a \cdot T(s) + \frac{\gamma_e(s)}{4\pi} \int_{4\pi} p(\theta, \phi, \theta', \phi') \cdot T_b(s, \theta', \phi') \cdot d\Omega'. \quad (2.14)$$

This is the scalar RTE in terms of brightness temperature.

### 2.1.5 A formal solution for the scalar RTE

With the expression for the absorption coefficient (Eq. 2.6), the optical thickness  $\tau(s)$  of a medium can be defined as the integrated absorption coefficient over the ray path of light propagating through the medium from  $s$  to  $s_2$

$$\tau(s) = \int_s^{s_2} \gamma_e(s') ds'. \quad (2.15)$$

By dividing Eq. 2.12 through  $\gamma_e$  and recalling that  $\gamma_a/\gamma_e = (1 - \varpi_0)$  the source function  $J_\nu$  is defined and the RTE (note that  $d\tau = -ds\gamma_e$ ) is simplified to

$$\frac{dI_\nu}{d\tau} - I_\nu = -J_\nu. \quad (2.16)$$

Multiplication with  $e^{-\tau}$  and application of the product rule of derivation lead to

$$\frac{d}{d\tau}(e^{-\tau}I_\nu(\tau)) = -e^{-\tau}J_\nu. \quad (2.17)$$

In remote sensing applications, a solution to this equation is sought after at the receiver position ( $\tau = 0$ ). Therefore the differential equation (Eq. 2.17) has to be integrated from the surface ( $\tau = \tau_*$ ) to the top of the atmosphere (TOA) at  $\tau = 0$ :

$$I_\nu(\tau = 0) = I_\nu(\tau = \tau^*)e^{-\tau^*} + \int_0^{\tau^*} e^{-\tau}J_\nu(\tau)d\tau, \quad (2.18)$$

with  $\tau^* = \int_0^{s_{top}} \gamma_e ds'$  the total optical thickness. By applying the Rayleigh-Jeans approximation this becomes

$$\begin{aligned} T_b(0) &= T_b(\tau^*)e^{-\tau^*} \\ &+ \int_0^{\tau^*} \left[ (1 - \varpi_0)T(\tau) + \frac{1}{4\pi} \int_{4\pi} p(\theta, \phi, \theta', \phi') \cdot T_b(\tau, \theta', \phi') \cdot d\Omega' \right] e^{-\tau} d\tau. \end{aligned} \quad (2.19)$$

Eq. 2.19 gives a term for the brightness temperature a receiver at the top of the atmosphere ( $\tau = 0$ ) looking downward towards the earth's surface ( $\tau = \tau^*$ ) would see, if the radiation is extenuated by absorption and scattering on the way ( $\tau^*$  to 0) through the atmosphere and intensified by emission at temperature  $T$  and by scattering at particles.

## 2.2 Polarization and Stokes parameters

The RTE derived in the previous sections describes the propagation of radiant intensities through a medium in terms of a scalar quantity. Since electro-magnetic radiation can be polarized by many interaction processes in the microwave range, like polarizing surface reflectivity and scattering at non-spherical particles, the RTE needs to be formulated in a manner that polarization states can be described.

Electro-magnetic radiation propagates in a medium as transverse waves. The direction of oscillation of the space and time dependent electric field vector  $\vec{E}(\vec{x}, t)$  and the phase difference between the components describes the state of polarization of an electro-magnetic wave. If a right-handed system defined by mutually orthogonal vectors  $\vec{n}$ ,  $\vec{e}_v$ , and  $\vec{e}_h$  is

assumed, pointing into propagation direction, arbitrary vertical and horizontal respectively, the components of an electric field vector for vertical and horizontal direction can be denoted by  $E_v$  and  $E_h$ . The components of the complex electric field can then be expressed by

$$E_v = a_v \exp[-i(\xi + \delta_v)] \quad (2.20a)$$

and

$$E_h = a_h \exp[-i(\xi + \delta_h)]. \quad (2.20b)$$

$a_v$  and  $a_h$  are the amplitudes of the electric field components,  $\delta_v$  and  $\delta_h$  the phases,  $\xi = \vec{k}\vec{x} - \omega t$ ,  $\vec{k} = 2\pi/\vec{\lambda}$  the wave number vector,  $\vec{\lambda}$  the wavelength,  $t$  the time,  $\omega$  the circular frequency, and  $i = \sqrt{-1}$ . Elliptically polarized waves can be completely described by this set of equations (Eqs. 2.20a and 2.20b) (linear and circular polarization are specific cases of elliptical polarization).

As mentioned before, the scalar intensity does not carry any information on the polarization. To be able to describe the intensity and polarization of an electro-magnetic wave, three additional quantities have to be defined to form a set of four quantities called Stokes parameters. These quantities build the components of the Stokes vector

$$\vec{I} = \begin{pmatrix} I \\ Q \\ U \\ V \end{pmatrix} = \frac{1}{Z_0} \begin{pmatrix} \left\langle \frac{E_v E_v^* + E_h E_h^*}{2} \right\rangle \\ \left\langle \frac{E_v E_v^* - E_h E_h^*}{2} \right\rangle \\ \langle \text{Re}(E_v E_h^*) \rangle \\ \langle \text{Im}(E_v E_h^*) \rangle \end{pmatrix}. \quad (2.21)$$

$\langle \dots \rangle$  denotes time averaging,  $Z_0 = \sqrt{\mu/\varepsilon}$  the impedance of the medium,  $\mu$  the magnetic permeability and  $\varepsilon$  the dielectric permittivity.

An alternative definition, called modified Stokes parameters, keeps the intensities of the vertical and horizontal polarization separate and replaces I and Q by:

$$I_v = \frac{I + Q}{2} \quad (2.22)$$

$$I_h = \frac{I - Q}{2} \quad (2.23)$$

The Stokes parameters as defined in here are in terms of intensities  $I_h$  and  $I_v$ , for horizontal and vertical polarization, respectively. In this case, the factor 2 in the numerator of Eq. 2.1 has to be omitted for the conversion of intensities to brightness temperatures since there is only one polarization mode. In particular radiative transfer codes are normalized to represent radiances.

Through the Stokes parameters polarization can be characterised as

$$\begin{aligned} Q^2 + U^2 + V^2 &= I^2 && \text{fully polarized} \\ Q^2 + U^2 + V^2 &\leq I^2 && \text{partially polarized} \\ Q &= U = V = 0 && \text{totally unpolarized} \end{aligned} \quad (2.24)$$

and with

$$p = \frac{\sqrt{Q^2 + U^2 + V^2}}{I} \quad (2.25)$$

a measure of the degree of polarization is defined.

To describe the interaction of polarized radiation with particles, the  $2 \times 2$  amplitude matrix  $\vec{S}(\vec{n}, \vec{n}')$  depending on both, the direction of the incident wave,  $\vec{n}$ , and of the scattered wave,  $\vec{n}'$ , with complex components is introduced. It transforms the electric field vector  $[E_v^{inc}, E_h^{inc}]^T$  of the incident wave into the electric field vector  $[E_v^{sca}, E_h^{sca}]^T$  of the scattered wave in the far-field (distance to particle is large compared to its dimension):

$$\begin{bmatrix} E_{v'}^{sca} \\ E_{h'}^{sca} \end{bmatrix} = \frac{\exp(ikR)}{R} \vec{S}(\vec{n}, \vec{n}') \begin{bmatrix} E_v^{inc} \\ E_h^{inc} \end{bmatrix}, \quad (2.26)$$

where  $\vec{n}$ ,  $\vec{e}_v$ , and  $\vec{e}_h$  correspond to the incoming direction and  $\vec{n}'$ ,  $\vec{e}_{v'}$ , and  $\vec{e}_{h'}$  to the propagation direction of the scattered wave.

The transformation from incoming system to scattered system can be performed as well in terms of the Stokes vector  $\vec{I} = [I, Q, U, V]^T$  and the Stokes vector of the scattered wave  $\vec{I}' = [I', Q', U', V']^T$ . The matrix performing this operation is a  $4 \times 4$  matrix with real elements usually called Mueller matrix  $\vec{F}$ . In case of a collection of particles, the average of all Mueller matrices is usually called phase matrix  $\vec{Z}$ . For deeper insight into the derivation of this matrices see *Tsang et al.* (1985) and *Mishchenko et al.* (2002).

To state the RTE for polarized radiation at specific frequency, expressions for the absorption, emission, and extinction describing these processes in terms of the Stokes vector  $\vec{I}_\nu$  are needed. The extinction matrix  $\langle \Sigma_\nu \rangle$  can be derived from the amplitude scattering matrix (see *Tsang et al.*, 1985 and *Mishchenko et al.*, 2002). The absorption vector  $\langle \vec{a}_\nu \rangle$  follows from the extinction and the ensemble-averaged phase matrix  $\langle \vec{Z}_\nu \rangle$ . The emission vector is achieved by building the product of Planck function  $B_\nu(T)$  and the absorption vector. The RTE of polarized radiation, called the VRTE, then reads

$$\begin{aligned} \frac{d\vec{I}_\nu(\vec{n})}{ds} &= -\langle \Sigma_\nu(\vec{n}, T) \rangle \vec{I}_\nu(\vec{n}, T) \\ &+ \langle \vec{a}_\nu(\vec{n}, T) \rangle B_\nu(T) + \int_{4\pi} d\Omega' \langle \vec{Z}_\nu(\vec{n}, \vec{n}', T) \rangle \vec{I}_\nu(\vec{n}', T). \end{aligned} \quad (2.27)$$

This equation is valid for monochromatic radiative transfer in the microwave region.

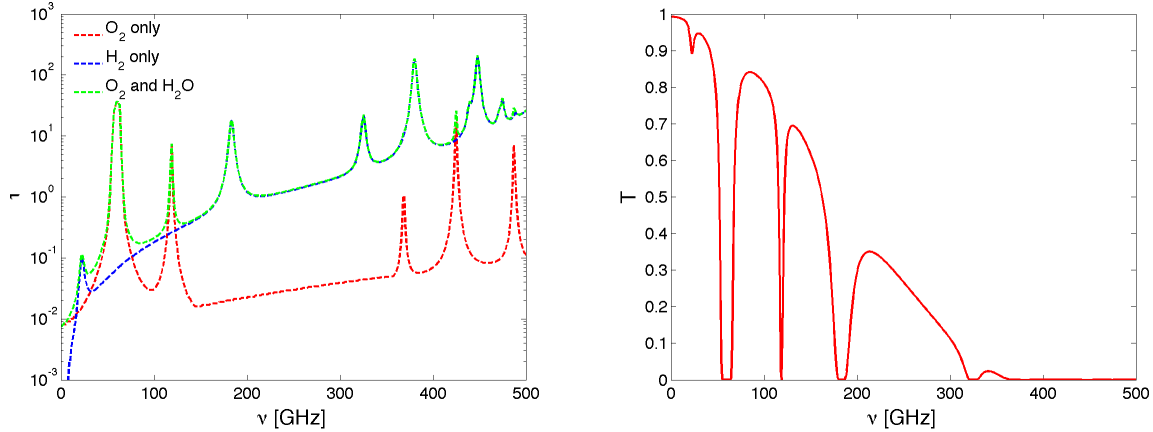


Figure 2.1: Optical thickness (left) due to  $\text{H}_2\text{O}$ ,  $\text{O}_2$ , and total ( $\text{H}_2\text{O} + \text{O}_2$ ) and atmospheric transmittance (right) due to absorption by  $\text{H}_2\text{O} + \text{O}_2$  for a typical mid-latitude summer atmosphere as a function of frequency in the microwave region for a space-borne receiver.

### 2.3 Gaseous absorption

For the propagation of microwave radiation through the atmosphere, the assumption of constant intensity  $I_\nu$  throughout the path does not hold. Even if clear-sky conditions (no hydrometeors apparent) are assumed, atmospheric gases like water vapor ( $\text{H}_2\text{O}$ ) and molecular oxygen ( $\text{O}_2$ ) exhibit significant absorption. The absorption by the most abundant gas nitrogen ( $\text{N}_2$ ) is small compared to  $\text{H}_2\text{O}$  and  $\text{O}_2$ . Due to their small particle size scattering at microwaves will not be significant.

With the expression for the absorption coefficient (Eq. 2.6), the optical thickness  $\tau(s)$  of a medium (Eq. 2.15) has been defined as the integrated absorption coefficient over the ray path of light propagating through the medium. The absorption by the molecules is related to transitions between rotational and vibrational resonance states. They occur at specific frequencies characteristic for each molecule and their intensity is dependent on environmental parameters like temperature and density. Fig. 2.1 shows the optical thickness  $\tau(s)$  and the optical transmittance due to gaseous absorption defined by

$$T = \frac{I(s)}{I_0} = \frac{I_0 \exp(-\tau(s))}{I_0}, \quad (2.28)$$

the ratio between attenuated intensity  $I(s)$  and incident intensity  $I_0$ .

In the lower microwave region (below 40 GHz), a weakly absorbing, pressure-broadened water vapor line at 22.235 GHz is dominant. Moving to higher frequencies a window region with highest transmittance at around 31.4 GHz is followed by a strong oxygen absorption complex around 60 GHz caused by magnetic dipole transitions resulting in a complete opaque atmosphere (transmittance  $T = 0$ ). The decrease in transmittance towards the center of the complex is often used for temperature profiling of the atmosphere (i.e. AMSU-A).

At 118.75 GHz the total gas absorption is dominated by an oxygen line. Above 120 GHz water vapor absorption again becomes dominant with the line center at 183.31 GHz, an absorption line used by AMSU-B for humidity profiling. Frequencies above 200 GHz exhibit a strong continuum absorption by water vapor resulting in optical thicknesses above 1 and transmittance below 0.3. Therefore these frequencies are not usable for surface observations. The strong continuum absorption is intersected by additional water vapor absorption lines at 320, 380.2, 440 GHz, some weak at 470 GHz, and oxygen lines at 360, 424.76, and 480 GHz.

In this study the absorption model by *Liebe et al.* (1993) is applied that considers contributions by water vapor, oxygen, and nitrogen. However in the higher microwave region narrow absorption lines by trace gases (mainly ozone) become relevant. Fig. 2.2 shows the effect on the brightness temperature for a nadir looking space-borne receiver calculated with the Atmospheric Radiative Transfer Simulator (ARTS; *Bühler et al.*, 2005a) on a 1 MHz resolution based on absorption coefficient from the BERNese Atmospheric Multiple Catalog Access Tool (BEAMCAT; *Feist*, 2004). Even though their influence is not very strong, it should not be disregarded in radiative transfer simulations at higher microwave frequencies.

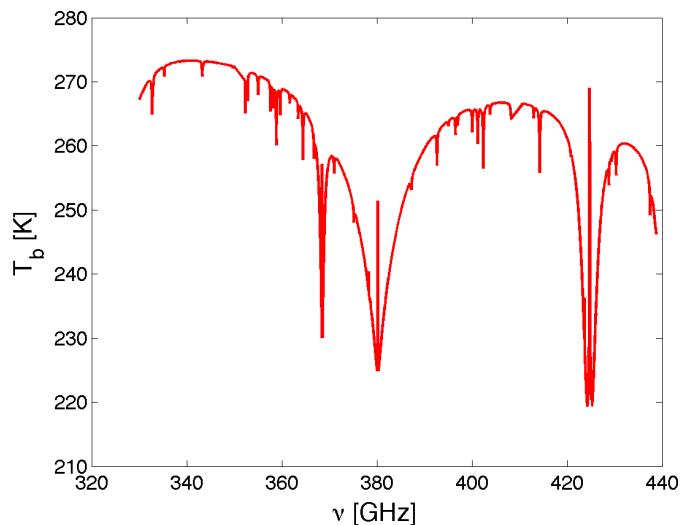


Figure 2.2: Influence of the ozone line absorption in addition to water vapor and oxygen at higher microwaves. Exemplarily the frequency range between 320 and 440 GHz is shown.

## 2.4 Interaction between hydrometeors and microwaves

In the previous section, the interaction of microwave radiation with the gaseous atmosphere through absorption has been described. Hydrometeors can influence the transfer of microwave radiation through the atmosphere in two ways; on the one hand through

absorption and emission and on the other hand through scattering at particles. Both processes are strongly dependent on the frequency and the complex index of refraction. Furthermore, the shape of ice particles and their orientation have a strong influence on their single-scattering properties, that are too complex to describe mathematically.

While at lower frequencies (below 60 GHz), frozen hydrometeors are transparent to microwave radiation, the signal is marginally influenced by absorption and emission at liquid precipitation due to its large imaginary part of the refractive index (see sec. 2.7). Scattering at liquid and solid particles is almost not present (see Fig. 2.4). At frequencies above 60 GHz outside strong absorption complexes, scattering effects at frozen particles begin to dominate the signal up-welling at the top at the atmosphere. Thus the signal emanating through emission in the liquid, precipitating layers in the lower parts of a precipitation system are masked by scattering at ice layers aloft. Apart from the frequency, the strength of this interaction through scattering is strongly dependent on particle properties like size, shape, and orientation.

Depending on the relation between particle size and interacting wave, described by the size-parameter (or Mie-parameter)

$$\chi = \frac{2\pi nr}{\lambda}, \quad (2.29)$$

where  $r$  is the radius of the smallest circumscribing sphere of the particle,  $n$  the complex refractive index of the surrounding medium ( $\sim 1$  for air), and  $\lambda$  the wavelength of the interacting wave, the theory of scattering computation is describe by either the Rayleigh theory ( $\chi \ll 1$ ) or geometric optics approximation ( $\chi \gg 1$ ). Typical size parameters of hydrometeors for the frequency range between 1 and 500 GHz are shown in Fig. 2.3. For particles like hydrometeors with their size in the range of the wavelength, exact solutions of Maxwell's equations need to be found.

### 2.4.1 Basic quantities of scattering theory

The amplitude scattering matrix (Eq. 2.26) is the basic quantity to be computed when solving the scattering problem of a single particle. From its components, called the amplitude scattering functions (ASFs), every other quantity, relevant to describe the interaction process can be deduced. The matrix links the incident electric wave to the scattered electric wave in the far-field:

$$\begin{pmatrix} S_{11} & S_{12} \\ S_{21} & S_{22} \end{pmatrix} = \begin{pmatrix} f_{vv}(\theta_s, \phi_s, \theta_i, \phi_i) & f_{vh}(\theta_s, \phi_s, \theta_i, \phi_i) \\ f_{hv}(\theta_s, \phi_s, \theta_i, \phi_i) & f_{hh}(\theta_s, \phi_s, \theta_i, \phi_i) \end{pmatrix}. \quad (2.30)$$

In contrast to Eq. 2.26, the directions of incident and scattered wave vector are described by  $(\theta_i, \phi_i)$  and  $(\theta_s, \phi_s)$ . For scattering processes at spherical particles, the ASFs can be computed by the Lorenz-Mie theory. Since the polarization state of the electric wave is not modified by the scattering process at spherical particles, the matrix is diagonal

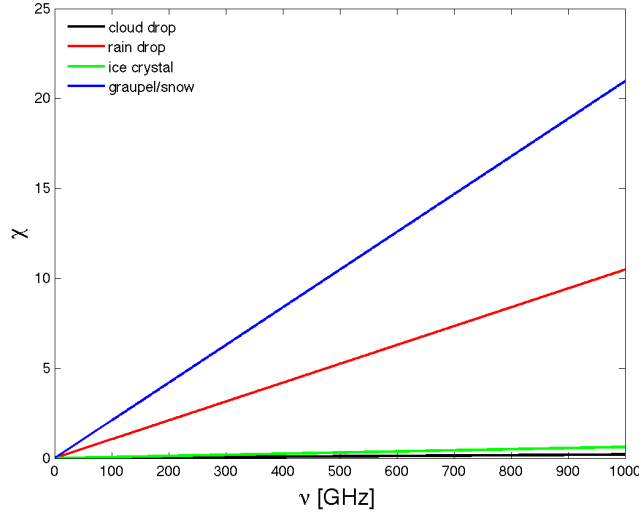


Figure 2.3: Size parameter for typical cloud droplets ( $d = 20\mu\text{m}$ ), rain drops ( $1000\mu\text{m}$ ), ice crystals ( $60\mu\text{m}$ ), and graupel/snow particles ( $2000\mu\text{m}$ ) in dependence of the frequency between 1 and 1000 GHz.

( $f_{hv}(\theta_s, \phi_s, \theta_i, \phi_i) = f_{vh}(\theta_s, \phi_s, \theta_i, \phi_i) = 0$ ). For non-spherical particles, various numerical models exist that approximate the ASFs (Mishchenko, 1993; Draine and Flatau, 2003; Liu, 2004; Kim et al., 2007; Mishchenko et al., 2007; etc.).

Once the ASFs (Eq. 2.30) are known, the scattering phase matrix elements can be calculated with the help of the definition of the Stokes parameter (Eq. 2.21)

$$\vec{P}(\theta_s, \phi_s, \theta_i, \phi_i) = \begin{pmatrix} |f_{vv}|^2 & |f_{vh}|^2 & \text{Re}(f_{vh}f_{vv}) & -\text{Im}(f_{vh}^*f_{vv}^*) \\ |f_{hv}|^2 & |f_{hh}|^2 & \text{Re}(f_{hh}f_{hv}) & -\text{Im}(f_{hh}^*f_{hv}^*) \\ 2\text{Re}(f_{vv}f_{hv}^*) & 2\text{Re}(f_{vh}f_{hh}^*) & \text{Re}(f_{vv}f_{hh}^* + f_{vh}f_{hv}^*) & -\text{Im}(f_{vv}f_{hh}^* - f_{vh}f_{hv}^*) \\ 2\text{Im}(f_{vv}f_{hv}^*) & 2\text{Im}(f_{vh}f_{hh}^*) & \text{Im}(f_{vv}f_{hh}^* + f_{vh}f_{hv}^*) & \text{Re}(f_{vv}f_{hh}^* - f_{vh}f_{hv}^*) \end{pmatrix} \quad (2.31)$$

For a distribution of particles, the phase matrix of the particle collection can be calculated by averaging over the scattering phase matrices of the distribution of particles

$$\langle \vec{P} \rangle(\theta_s, \phi_s, \theta_i, \phi_i) = \sum_{\text{particles}} \vec{P}(\theta_s, \phi_s, \theta_i, \phi_i), \quad (2.32)$$

where  $\sum_{\text{particles}}$  is the average of a distribution in terms of size, shape, and orientation. The averaged phase matrix  $\langle \vec{Z} \rangle$  describes the angular distribution of electro-magnetic waves scattered by particles. It is the term which enters the VRTE (Eq. 2.27).

If an ensemble of spherical particles is considered, the extinction matrix is diagonal. For a collection of non-spherical particles, this is not true. To deduce the extinction matrix, the

elements of the scattering amplitude matrix (Eq. 2.31) need to be evaluated in the forward direction ( $\theta_s = \theta_i = \theta$  and  $\phi_s = \phi_i = \phi$ )

$$\langle \sum \rangle (\theta, \phi) = \frac{2\pi n_0}{k} \begin{pmatrix} 2Im(\langle f_{vv} \rangle) & 0 & Im(\langle f_{vh} \rangle) & -Re(\langle f_{vh} \rangle) \\ 0 & 2Im(\langle f_{hh} \rangle) & Im(\langle f_{hv} \rangle) & Re(\langle f_{hv} \rangle) \\ 2Im(\langle f_{hv} \rangle) & 2Im(\langle f_{vh} \rangle) & Im(\langle f_{vv} + f_{hh} \rangle) & -Re(\langle f_{hh} - f_{vv} \rangle) \\ 2Re(\langle f_{hv} \rangle) & -2Re(\langle f_{vh} \rangle) & -Re(\langle f_{vv} - f_{hh} \rangle) & Im(\langle f_{vv} + f_{hh} \rangle) \end{pmatrix}, \quad (2.33)$$

with angular brackets denoting the average over the orientation and the size distribution of the particles,  $n_0$  the number of particles per unit volume,  $k_e^v(\theta, \phi) = n_0(4\pi/k)Im\langle f_{vv} \rangle$ ,  $k_e^h(\theta, \phi) = n_0(4\pi/k)Im\langle f_{hh} \rangle$ , and  $k$  the extinction coefficient for vertical and horizontal components, respectively.

After Kirchhoff's law in local thermodynamic equilibrium, spectral directional absorption is equal to spectral directional emission. For an ensemble of particles, the absorption vector can be defined by using the extinction matrix (Eq. 2.33) and the phase matrix (Eq. 2.31) as

$$\langle \vec{a}(\vec{r}) \rangle = \begin{pmatrix} k_e^v(\vec{r}) - \int_{4\pi} [\langle \vec{P} \rangle_{11} + \langle \vec{P} \rangle_{21}] (\vec{r}, \vec{r}') d\Omega' \\ k_e^h(\vec{r}) - \int_{4\pi} [\langle \vec{P} \rangle_{12} + \langle \vec{P} \rangle_{22}] (\vec{r}, \vec{r}') d\Omega' \\ -2\langle \sum \rangle_{13}(\vec{r}) - 2\langle \sum \rangle_{23}(\vec{r}) + 2 \int_{4\pi} [\langle \vec{P} \rangle_{13} + \langle \vec{P} \rangle_{23}] (\vec{r}, \vec{r}') d\Omega' \\ 2\langle \sum \rangle_{14}(\vec{r}) + 2\langle \sum \rangle_{24}(\vec{r}) - 2 \int_{4\pi} [\langle \vec{P} \rangle_{14} + \langle \vec{P} \rangle_{24}] (\vec{r}, \vec{r}') d\Omega' \end{pmatrix}. \quad (2.34)$$

For decoupled third and fourth components of the Stokes vector the phase matrix, absorption vector, and the extinction reduce to

$$\vec{P}(\theta_i, \phi_i, \theta_s, \phi_s) = \begin{pmatrix} |f_{vv}|^2 & |f_{vh}|^2 \\ |f_{hv}|^2 & |f_{hh}|^2 \end{pmatrix}, \quad (2.35)$$

$$\langle \vec{a}(\vec{r}) \rangle = \begin{pmatrix} k_e^v(\vec{r}) - \int_{4\pi} [\langle \vec{P} \rangle_{11} + \langle \vec{P} \rangle_{21}] (\vec{r}, \vec{r}') d\Omega' \\ k_e^h(\vec{r}) - \int_{4\pi} [\langle \vec{P} \rangle_{12} + \langle \vec{P} \rangle_{22}] (\vec{r}, \vec{r}') d\Omega' \end{pmatrix}, \quad (2.36)$$

and

$$\langle \sum \rangle (\theta, \phi) = \frac{2\pi n_0}{k} \begin{pmatrix} 2Im(\langle f_{vv} \rangle) & 0 \\ 0 & 2Im(\langle f_{hh} \rangle) \end{pmatrix}. \quad (2.37)$$

In case of particles with a spherical shape or randomly orientation within an ensemble, the absorption and scattering cross sections and therefore the extinction cross section do not depend on direction and polarization. Thus, they can be represented by simple scalar numbers named efficiencies. These are defined as

$$Q_a = \frac{\sigma_a}{\pi r^2}, \quad (2.38)$$

$$Q_s = \frac{\sigma_s}{\pi r^2}, \quad (2.39)$$

and

$$Q_e = \frac{\sigma_e}{\pi r^2}, \quad (2.40)$$

which are the *radiative* cross sections divided by their geometric cross sections. Thereby, the extinction efficiency is a measure of how effective a particle can block a beam of light in relation to its size. Examples of the efficiencies calculated with the Lorenz-Mie theory will be shown in the following subsection.

### 2.4.2 Scattering parameter computation - Approximations

When dealing with radiative transfer calculations in cloudy atmospheres, interaction processes between the radiation and gas molecules and between radiation and hydrometeors have to be considered. The influence of gases is described by their absorption coefficients. The effect of hydrometeors is included through their single-scattering properties, namely the absorption vector, the scattering matrix, and the extinction matrix. The intensity of the interaction between radiation and hydrometeors depends on various parameters like size, phase, orientation, shape, and refractive index of the particles, as well as on the considered wavelength.

As long as spheres are considered, the single-scattering properties can be accurately calculated by the Lorenz-Mie theory (*Mie*, 1908), since even frequencies in the submillimeter range together with particles with dimension around 1 cm do not result in size parameters larger than 60 (see Eq. 2.29). For sufficient small particles, the single-scattering calculations can be performed by the Rayleigh approximations (e.g. *Bohren and Clothiaux*, 2006).

To achieve this goal for non-spherical particles, two approaches have been used so far. One is to assume a known particle shape and therefore to describe it as accurately as possible by approximations like the T-matrix method (*Mishchenko et al.*, 1996) or the discrete dipole approximation (DDA; *Draine and Flatau*, 2000). The second one is based on the Lorenz-Mie theory for the calculation of the single-scattering properties of spherical particles. Thereby, the problem of scattering at non-spherical particles is approximated

through modified diameters, and therefore densities, and dielectric properties (e.g. *Liu and Curry, 2000; Evans et al., 2002; Bennartz and Petty, 2001; Kim et al., 2007*).

In the following subsection some of the mostly common used methods to calculate the single-scattering properties in microwave region will be described.

### Lorenz-Mie theory

When homogeneous spheres (or coated spherical objects) are considered the single-scattering properties in the microwave range can be described analytically by a series of spherical harmonics. The expansion coefficients to this series are named Mie-coefficients and only dependent on the complex index of refraction of the sphere  $n$  and the dimensionless size-parameter  $\chi$  as described in Eq. 2.29. Details of the derivation of the function and the coefficients describing the scattering properties can be found in *Bohren and Clothiaux (2006)* or *Petty (2006)*.

Fig. 2.4 shows examples of the single-scattering properties in terms of efficiencies (see Eqs. 2.38-2.40) and single-scattering albedo calculated with the Lorenz-Mie theory for typical particles. The particles and the corresponding size parameters are described in Fig. 2.3 (water droplet, ice crystal, rain drop, and graupel/snow particle) for frequencies between 1 and 1000 GHz. In general, independent of particle type the absorption and scattering efficiencies increase with increasing frequency due to the size parameter dependence, and the larger the particles the stronger their influence on the radiation. For cloud droplets, absorption is the dominant process throughout the frequency range. Below 20 GHz, the interaction of rain drops with the radiation is due to absorption. Above 20 GHz absorption efficiency equals scattering efficiency resulting in a single-scattering albedo of 0.5. Rain drops have in general a much greater extinction efficiency than frozen particles below 50 GHz and a much lower single-scattering albedo. This is the reason why remote sensing technics working at lower frequencies are essentially sensitive to water emission. At higher frequencies (above 50 GHz), graupel/snow extinction becomes comparable to rain extinction. Graupel and snow particles are strong scatterers (single-scattering albedo is close to 1 above 10 GHz). Together with rain drops, they dominate the signal in the microwave frequency range. Since ice crystals are small with a very small imaginary part of the refractive index, there is almost no absorption present at frequencies below 300 GHz and their effect is negligible compared to other hydrometeors. Above 300 GHz, their influence gets noticeable through increased scattering efficiency.

In Fig. 2.5 the dependency of the single-scattering properties to particle dimension at window frequencies in the millimeter-wavelength range is shown. The results were again obtained with Lorenz-Mie theory and reflect that small particles are almost transparent, especially for the solid and mixing (graupel/snow) phase at lower frequencies. Larger graupel or snow particles ( $d > 2$  mm) have a single-scattering albedo close to 1, whereas liquid particles converge to 0.5 as the size parameter gets larger. At this relatively low frequencies, ice crystals are hardly detectable.

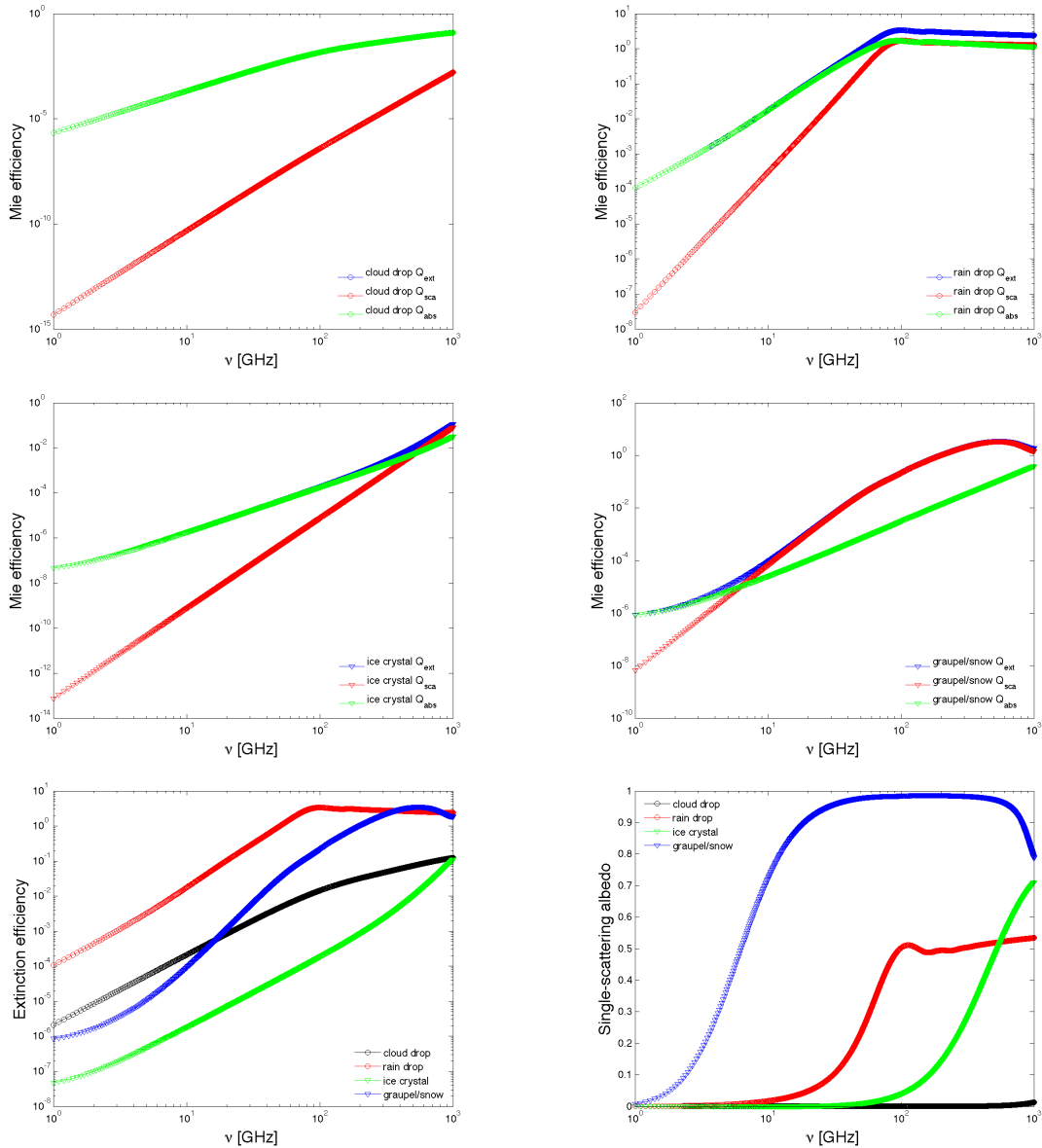


Figure 2.4: Mie efficiencies calculated with Lorenz-Mie theory for frequencies between 1 and 1000 GHz for typical particles: cloud droplet ( $d = 10 \mu\text{m}$  at  $10^\circ\text{C}$ , top left), rain drop ( $1000 \mu\text{m}$  at  $10^\circ\text{C}$ , top right), ice crystal ( $60 \mu\text{m}$  at  $-20^\circ\text{C}$ , middle left), and graupel/snow particle ( $2000 \mu\text{m}$  at  $-5^\circ\text{C}$ , middle right). The bottom row shows comparisons of the extinction efficiencies (left) and the single-scattering albedo (right).

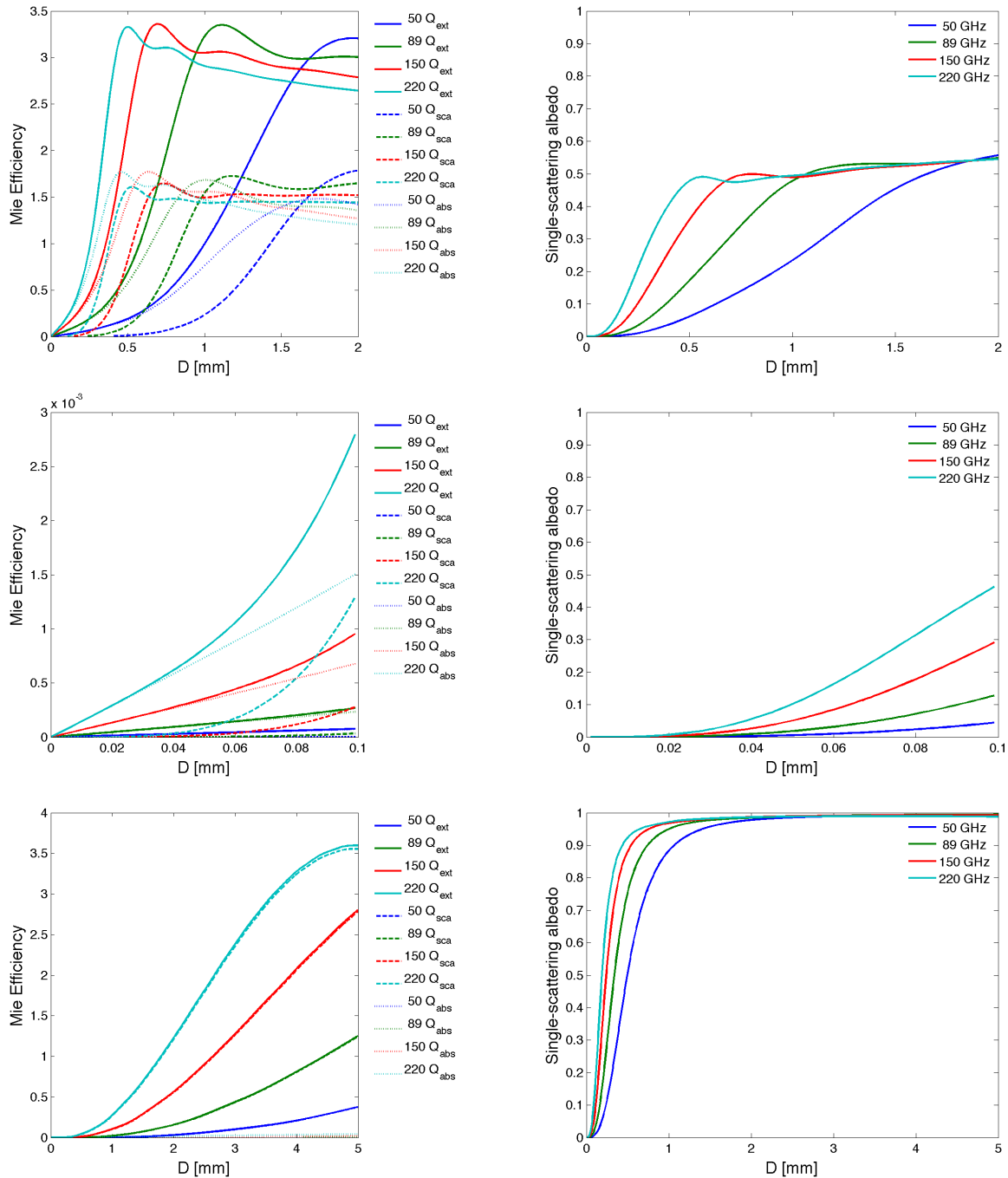


Figure 2.5: Mie efficiencies and single-scattering albedo calculated with Lorenz-Mie theory for different frequencies (50, 89, 150, and 220 GHz) and different particle types/dielectric properties (see sec. 2.7): water droplets (top), ice crystals (middle), and graupel/snow particles as a mixing between pure ice and air (bottom).

### T-matrix

The scattering properties for non-spherical, rotationally symmetric particles with an additional symmetry to their plane of rotation can be described by the T-matrix method (*Mishchenko et al.*, 1996). For the calculation of the single-scattering properties, the Extended Boundary Condition Method (EBCM; *Waterman*, 1971) is applied. For spheres, the formulations used in the T-matrix method reduce to the one describing the Lorenz-Mie theory.

Calculations with the T-matrix method show the importance of considering the shape of frozen hydrometeors and the Chebychev shaped (*Czekala et al.*, 1999) falling rain drops in the scattering calculations. It can be seen that there is a significant impact on the intensity and the polarization signal of microwave radiation in the atmosphere.

### Discrete dipole approximation

The Discrete Dipole Approximation (DDA) is an approximation of a continuous target by a finite mesh of polarizable elements/dipoles. This method for describing the scattering properties of arbitrarily shaped particles is widely used in microwave radiometry (see *Evans and Stephens*, 1995a; *Liu*, 2004) and astrophysics. It was first developed by *Purcell and Pennypacker* (1973). *Draine and Flatau* (2000) reviewed the method and compiled well-documented code to this approximation that is freely available under <http://arxiv.org/abs/astro-ph/0008151v4>.

By using the DDA it is possible to calculate the electro-magnetic scattering and absorption of arbitrarily shaped particles, as long as the distance between the single dipoles is small compared to the considered wavelength. The method is not well suited for particles with very large complex refractive indices since these require much narrower distance between the dipoles thereby requiring much more memory size. The technique was used by *Evans and Stephens* (1995a) to investigate the impact of particle shape and orientation on the scattering properties of different ice habits by computing the single-scattering properties at different frequencies. They found that the extinction increases dramatically with frequency and that the difference in extinction coefficients can be up to a factor of three between the various shapes (smallest for rosettes and highest for solid columns). Since oriented plates polarize most, they result in the highest polarization difference followed by rosettes and columns. The highest scattering ratio (a measure for the forward scattering) can be found for solid columns with decreasing value for thinner particles.

The authors of the DDA code (*Draine and Flatau*, 2000) note that accurate calculations of electro-magnetic scattering are possible for size-parameters less than 15 and when the complex refractive index  $n$  of the scattering medium is not larger compared to unity ( $|n - 1| < 1$ , *Draine and Flatau*, 2000). Within the ESA (European Space Agency) funded study "Development of Radiative Transfer model for the frequency range between 200 and 1000 GHz" (*Sreerekha et al.*, 2005) validation calculations for the DDA have been performed. It was found that single-scattering properties calculated with the DDA code and Lorenz-Mie theory for spherical particles and frequencies, so that  $|n|kd < 0.5$ , with  $k$  as

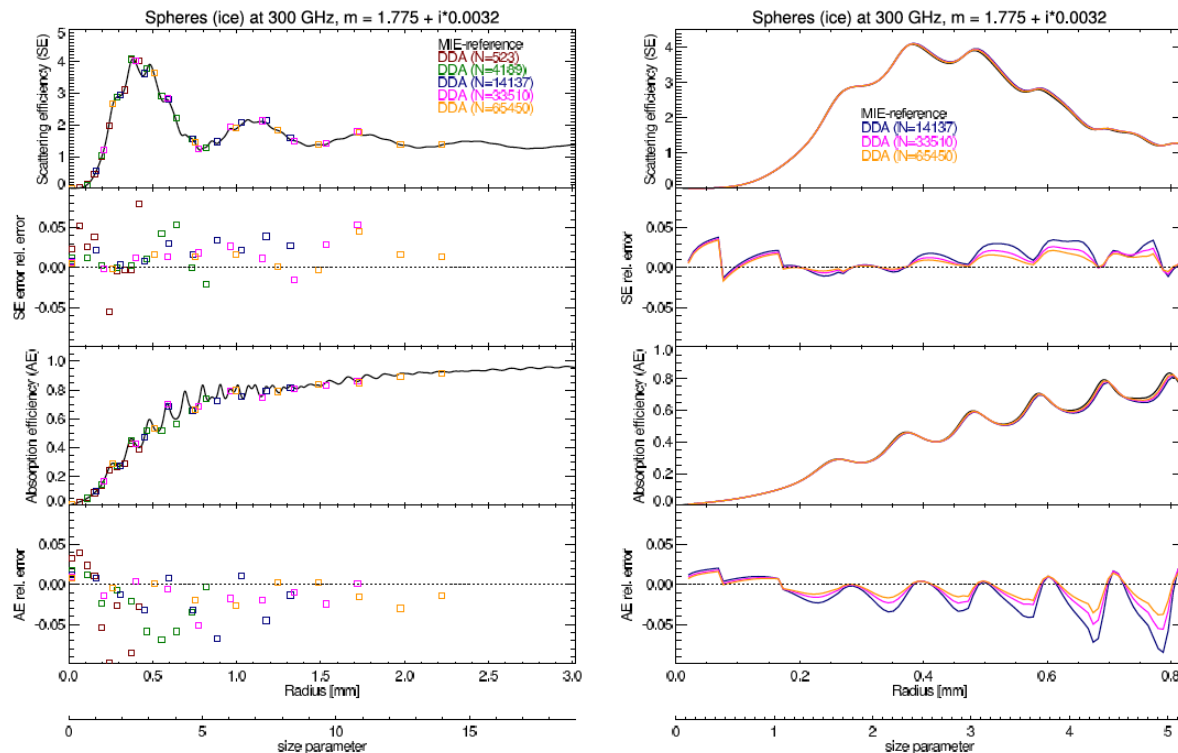


Figure 2.6: Scattering and absorption efficiencies as a function of the size parameter. The relative errors are given with respect to the Lorenz-Mie reference calculations. The right diagrams were calculated for a higher resolution in size parameter range than in the left diagrams. However, the left diagrams show accuracies up to size parameters of  $\sim 15$ .

the wave number and  $d$  as the dipole separation, agree well (see Fig. 2.6). Similar results have been achieved by *Liu* (2004). The accuracy of DDA calculations depends strongly on the number of dipoles  $N$ : the larger the number, the more accurate the calculated single-scattering properties. On the other hand, the computation time scales with the number of dipoles, so that an optimal number needs to be found. For a given number of dipoles  $N$ , the accuracy of the DDA approximations depends mainly on the refractive index: smaller refractive indices can be described more accurately.

### Parameterizations

The Lorenz-Mie calculations for the single-scattering properties are much more time efficient than methods describing the particle shapes "more exactly". Therefore it is worth to seek for parameterizations of the particle properties that allow the calculations of the single-scattering properties by the Lorenz-Mie formalism, even though the particles are non-spherical. This means that the shape is assumed as a sphere and the non-spherical character is included in the density or dielectric property assumptions. Various approaches to parameterizations of the properties of non-spherical particles exist (e.g. *Liu and Curry*,

2000; *Evans et al.*, 2002; *Bennartz and Petty*, 2001; *Kim et al.*, 2007), whereof the one by *Liu* (2004) will be presented in this subsection.

**Liu - equal-mass sphere approximation** To describe the single-scattering properties of non-spherical ice and snow particles, *Liu* (2004) approximates the non-sphericity by assuming equivalent spheres. These spheres have the same mass as the approximated non-spherical particles and a radius and density between a 'solid-sphere' and a 'soft-sphere' particle description. Their dielectric properties are described by the Maxwell-Garnett mixing formula (Eq. 2.56). The diameter of the equivalent mass-spheres is described with a quantity named "softness parameter" (SP) defined as

$$SP = \frac{D - D_0}{D_{max} - D_0}, \quad (2.41)$$

where  $D$ ,  $D_0$ , and  $D_{max}$  are the diameters of the equivalent sphere, the solid-sphere, and the soft-sphere, respectively. Hereby, solid means an equal-mass sphere with the density  $0.916 \text{ gm}^{-3}$  of solid ice. The equal-mass soft-sphere is described by a spherical particle with diameter being equal to the maximum dimension of the non-spherical particle and reduced density. This means that the particle is inflated by keeping the mass constant, so that the density decreases. The SP can be derived by finding a particle diameter so that its single-scattering properties after Lorenz-Mie theory fit to the one calculated with the DDA approximation for an more exact description of the particle. The SP varies with the particle shape, the frequency, and the single-scattering property. Values for two different habits implemented in the applied RT model are shown in Tab. 2.1.

In the microphysical scheme of Méso-NH the cloud ice particles are assumed to be solid-spheres with a density of  $0.916 \text{ gm}^{-3}$ . Therefore, the assumed diameter corresponds to a solid-sphere diameter. For particles with a solid-sphere diameter  $D_0 > 45 \mu\text{m}$ , a relation for the maximum diameter  $D_{max}$  is given by *Liu and Curry* (2000) in terms of the solid-sphere diameter  $D_0$  as

$$D_{max} = 2.71D_0^{0.737}. \quad (2.42)$$

Smaller particles are assumed to produce no significant scattering signal in the considered microwave region. The diameter  $D$  of the approximated particle is given by Eq. 2.41 and its density can be deduced from the equivalent mass assumption through

$$\rho = \frac{D_0}{D} \cdot 0.916. \quad (2.43)$$

For snowflakes, a generalized  $\gamma$ -distribution function with respect to maximum diameter  $D_{max}$  is assumed and discretized into appropriate bins. The density of each single particle varies with its size and is defined by

Frequency (GHz)	Rosettes	Snowflakes
	$\sigma_{sca}$	$\sigma_{sca}$
85.5	0.54	0.33
150.0	0.36	0.27
220.0	0.26	0.22

Table 2.1: Softness parameters (SP) for the calculation of the equal-sphere diameter to derive the scattering cross section  $\sigma_{sca}$ . The SP are averaged over different shapes of the corresponding particles.

$$\rho(D_{max}) = \frac{6m}{\pi D_{max}^3} \quad (2.44)$$

with the mass  $m$  as

$$m = aD_{max}^{b-3}. \quad (2.45)$$

For snowflakes  $a$  is 0.02 and  $b$  is 19.6. The solid-sphere diameter for these particles can be calculated by assuming equal masses. According to Eqs. 5a and 5b of *Liu* (2004), the diameter of the solid-sphere for these snowflakes is given by

$$D = D_{max}(\rho_{max}/\rho_e)^{(1/3)}. \quad (2.46)$$

Thereby, the effective density  $\rho_e$  is defined as the mass of the particle divided by the volume of a circumscribing sphere. With the values for SP in Tab. 2.1 and Eq. 2.41, the equal-sphere diameter for snowflakes can be derived and the single-scattering properties calculated by the Lorenz-Mie theory.

## 2.5 Boundary conditions

When dealing with radiative transfer in the atmosphere either for ground based, airborne or space-borne applications, appropriate boundary conditions have to be applied in the RTE.

Downwelling radiation from space is commonly approximated by  $B(2.7\text{K})$  for all incident angles. It is the background radiation for upward looking sensors.

The signal of a microwave sensor observing the earth's surface is composed of surface and atmospheric contributions. When considering the radiative transfer for satellites, the lower boundary conditions, i.e. the earth's surface, are a crucial point in the RTE (Eq. 2.14). For the microwave window regions below 200 GHz and in the absence of hydrometeors, the atmosphere is to a high degree transparent and the effect of the surface on the up-welling

brightness temperature can not be neglected. The amount of radiation emitted by the earth's surface depends on surface parameters like surface type, soil moisture, roughness, its temperature, and, in addition on observation frequency, geometry, and polarization. For frequencies between 200 and 1000 GHz or close to absorption complexes, the surface effect is shaded and the signal is dominated by the atmospheric contributions.

For radiative transfer calculations for the millimeter- and submillimeter-wavelength region and in the mid-latitudes, it is reasonable to consider continental (emissivity  $\epsilon \approx 0.9$ ) and sea surfaces ( $\epsilon \approx 0.4 - 0.7$ ) separately.

### 2.5.1 Land surfaces

Since the microwave emissivity of land surfaces depends on a large number of highly variable parameters, that are poorly known and not readily observable, an accurate modeling is very complex. Even if these parameters were available, the emissivity calculations would be computationally expensive since multiple scattering needs to be included. Furthermore, many different surface types can be seen within the footprint of a satellite receiver ( $\approx 16\text{km}$  for AMSU-B) that all have to be included to accurately model the emissivity corresponding to this area.

An approach to infer on the microwave surface emissivity is to use clear-sky satellite measurements in the desired frequency range, and removing the remaining atmospheric effects. This approach has been adopted by *Prigent et al.* (1997) based on SSM/I satellite measurements over the whole global and every season resulting on monthly mean global land surface emissivity maps for the SSM/I frequencies. Furthermore, algorithms were developed that allow the interpolation to emissivities at interjacent microwave frequencies. For frequencies greater than 85.5 GHz (highest SSM/I channel), the surface emissivity is assumed to be constant at the value for 85.5 GHz. Due to the nonexistence of measurements and an increase of the atmospheric absorption resulting in a reduction of the surface impact, this assumption should be valid except for very wet land surfaces (*Janssen*, 1993, chap. 6).

### 2.5.2 Ocean surfaces

Ocean surfaces in general have an emissivity much lower than land surfaces but have strong polarizing effects. Since radiative transfer models for the microwave region were developed, various approaches to model the ocean surface emissivity were successfully pursued. The crucial parameters that influence the emissivity are the ocean wave activity with the corresponding foam coverage induced by the wind in the lowest level, the surface temperature, the salinity of the salt water, and the observation frequency and angle.

In this study the FAST Emissivity model (FASTEM), developed by *English and Hewison* (1998), is employed. With FASTEM, the permittivity over ocean surfaces is calculated using laboratory measurements of the Debye parameters (*Lamkaouchi et al.*, 1997). The reflectivity is multiplied by a small scale roughness factor, which is parameterized depending on the 10 m wind speed. The surface roughness is also modeled based on the 10 m wind speed and is added to the vertical and horizontal reflectivity.

## 2.6 Solving the radiative transfer equation

In remote sensing applications from space, a solution of the radiative transfer problem needs to be found by starting with the three-dimensional fully polarized VRTE stated in Eq. 2.27. In this equation, the scattering process is described by the phase matrix depending on the incoming and outgoing direction, i.e.  $(\theta', \phi')$  and  $(\theta, \phi)$ . Together with the three positions in space, Eq. 2.27 is a seven dimensional set of equations. Even more, through the mixing between the component intensities of the Stokes vector by scattering and extinction, this set of four integro-differential equations is coupled. In most applications, this problem can be simplified by making assumptions on the atmosphere and shape and orientation of the scattering particles.

If a plan-parallel azimuthally isotropic and horizontally homogeneous atmosphere is assumed the radiation in the VRTE (Eq. 2.27) only depends on  $z$  and  $\theta$  and not on the full set of seven dimensions  $(x, y, z, \theta, \phi, \theta', \phi')$ . Due to the azimuthal symmetry (constant radiation in azimuth directions), the phase matrix can be integrated over  $2\pi$  and the interaction between the first two and the third and fourth Stokes component vanishes. Thus, the scattering phase matrix Eq. 2.31 reduces to Eq. 2.35, the absorption vector Eq. 2.34 to Eq. 2.36, and the extinction matrix Eq. 2.33 to Eq. 2.37, respectively.

Hence, for a one dimensional problem, the VRTE (Eq. 2.27) can be reduced to (*Tsang et al.*, 1985)

$$\frac{d\vec{I}(z; \theta)}{dz} = \vec{I}(z; \theta)e^{-\tau_*/\mu} + \int_0^{\tau_*} J(\tau'; \mu) \exp^{-\tau'/\mu} \frac{d\tau'}{\mu}. \quad (2.47)$$

$$I(0; \mu) = I(\tau_*; \mu) \exp^{-\tau_*/\mu} + \int_0^{\tau_*} J(\tau'; \mu) \exp^{-\tau'/\mu} \frac{d\tau'}{\mu} \quad (2.48)$$

is a solution where the first term on the right-hand site describes the surface contribution attenuated to the top and the second one the internal contribution of the atmosphere either through scattering or emission.

The solution of the VRTE for a non-scattering atmospheres can be found analytically. If scatterers are present in the ray path of light, numerical algorithms need to be applied to find solutions of Eq. 2.27. For this purpose, a variety of algorithms exist. The Matrix Operator Method (MOM) is mainly applied to one-dimensional problems (*Liu et al.*, 1991), while the Discrete Ordinate Method (DOM) and Spherical Harmonics DOM (SHDOM) are also applied to three-dimensional problems (*Evans and Stephens*, 1995a; *Evans and Stephens*, 1995b). Monte-Carlo methods are used mainly for three-dimensional modeling (*Liu and Simmer*, 1996; *Roberti et al.*, 1994)

In the applied RT model (see sec. 2.8), the VRTE is solved by an iterative method. In its initialization step, the scattering source is neglected and the down-welling radiation is calculated for all levels beginning from top to bottom by including emission and absorption. When reaching the lower boundary, the reflection of down-welling radiation is calculated

and added to the surface emission. Then the ray path of light is reversed and the up-welling radiation for all levels and directions is calculated. For non-scattering atmospheres, this procedure provides already the full solution.

If scattering hydrometeors are present, further iterations including the scattering source functions are required. Again, each layer is considered from top to bottom and backward. Thereby the scattering coefficients are applied to the radiation field from the previous iteration step and the resulting radiation field is calculated for all angles. The emission, absorption, and reflection contributions remain the same, but the scattering source term is adjusted in each iteration step. After each iteration, the resulting radiation field is compared to the one of the previous iteration. If the maximum difference at all levels and directions is below a initially defined value, the iterations are stopped and the last radiation field is converted into brightness temperatures by using the inverse Planck function (Eq. 2.1).

In order to obtain multiple scattering solutions, the iterative method uses an automatic re-scaling of the vertical level thicknesses. In each layer, single-scattering is assumed and multiple-scattering is included by the number of iterations being performed. The algorithm obtains correct results for multiple-scattering as long as the assumption of single-scattering in each layer and iteration step is valid. The optical thickness resulting from scattering plus absorption cross section is used as an indicator of the probability for a scattering process taking place in the layer. If a single layer has an optical thickness above an adjustable threshold value, the layer is divided into sub-layers until the optical thickness of each layer is smaller than the threshold value. By that single-scattering in each layer and iteration step is ensured.

## 2.7 Dielectric properties

For electro-magnetic waves propagating through a medium, the dielectric, magnetic, and refractive properties of the medium are important in several ways. Therefore, an accurate knowledge of these quantities is important. The complex refractive index  $n = n' - in''$  is simply the square root of the dielectric constant (dielectric permittivity) and the magnetic permeability

$$n = \sqrt{\varepsilon\mu}, \quad (2.49)$$

where

$$\varepsilon = \varepsilon' - i\varepsilon'' \quad \text{and} \quad \mu = \mu' - i\mu''. \quad (2.50)$$

For remote sensing in the atmosphere the magnetic permeability is approximately unique ( $\mu \approx \mu_0 = 1$ , where  $\mu_0$  is the permeability of vacuum). The real part of the refractive index  $n'$  gives a measure for the speed of light in a medium, and the imaginary

part  $n''$  describes how electro-magnetic waves are absorbed. The dielectric constant depends on the considered frequency and is a function of bulk properties of the medium like temperature, pressure, etc..

For a homogeneous medium like water or pure ice, where homogeneous means in the sense that structural features of the medium are much smaller than the wavelength of the interacting electro-magnetic wave, the Debye-equations can be applied to describe the dielectric constant

$$\varepsilon' = \varepsilon_\infty + \frac{\varepsilon_s - \varepsilon_\infty}{1 + 4\pi^2\nu^2\tau^2} \quad \text{and} \quad \varepsilon'' = \frac{2\pi\nu\tau(\varepsilon_s - \varepsilon_\infty)}{1 + 4\pi^2\nu^2\tau^2}, \quad (2.51)$$

with  $\nu$  as the frequency of the electro-magnetic field,  $\varepsilon_s$  the permittivity of the polar liquid in a static electric field  $\nu \rightarrow 0$ ,  $\tau$  the relaxation time of the polar molecule within the viscous medium, and  $\varepsilon_\infty$  the permittivity at an infinite frequency. Since the permittivity is temperature dependent, the Debye parameters depend on temperature as well.

Although measurements and calculations of the parameters  $\varepsilon_s$ ,  $\varepsilon_\infty$ , and  $\tau$  to Eq. 2.51 do not coincident with a sufficient accuracy, experiments show that the Debye expressions are an appropriate approximation, at least for the lower microwave frequencies. For higher frequencies, only few, not very accurate datasets are available to infer on the parameters for the Debye-equations. Therefore, interpolation functions are needed to describe the dielectric properties and the refractive index.

The refractive indices for water and pure ice show completely different characteristics. While water has a very large imaginary part in the lower microwave region and is therefore highly absorbing, ice has almost no absorption (see Fig. 2.7). The real part of water is much larger than for ice and shows a very strong temperature dependence in the lower microwave region.

In this study, the function given by *Manabe et al.* (1987) for the refractive index is used for cloud droplets and rain drops

$$\varepsilon_{water}(T, \nu) = \frac{\varepsilon_0 - \varepsilon_1}{1 - i(\nu/\gamma_1)} + \frac{\varepsilon_1 - \varepsilon_2}{1 - i(\nu/\gamma_2)} + \varepsilon_2 \quad (2.52)$$

with  $\nu$  the frequency in GHz,  $\theta = 1 - 300/T$ ,  $\varepsilon_0 = 77.66 - 103.3\theta$ ,  $\varepsilon_1 = 0.0671\varepsilon_0$ ,  $\varepsilon_2 = 3.52 + 7.52\theta$ ,  $\gamma_1 = 20.20 + 146.4\theta + 316\theta^2$ , and  $\gamma_2 = 39.8\gamma_1$ .

For pure ice the refractive index is calculated after *Mätzler* (2006)

$$\begin{aligned} \varepsilon'_{ice} &= 3.1884 + 9.1 \cdot 10^{-4}(T - 273K) & \text{for } 243 \leq T \leq 273K \\ \varepsilon'_{ice} &= 3.1 & \text{for } T < 243K \end{aligned} \quad (2.53)$$

for the real part. The imaginary part is given by

$$\varepsilon''_{ice} = \frac{\alpha}{\nu} + \beta\nu, \quad \text{with} \quad \alpha = (0.00504 + 0.0062\theta) - \exp(-22.1\theta), \quad (2.54)$$

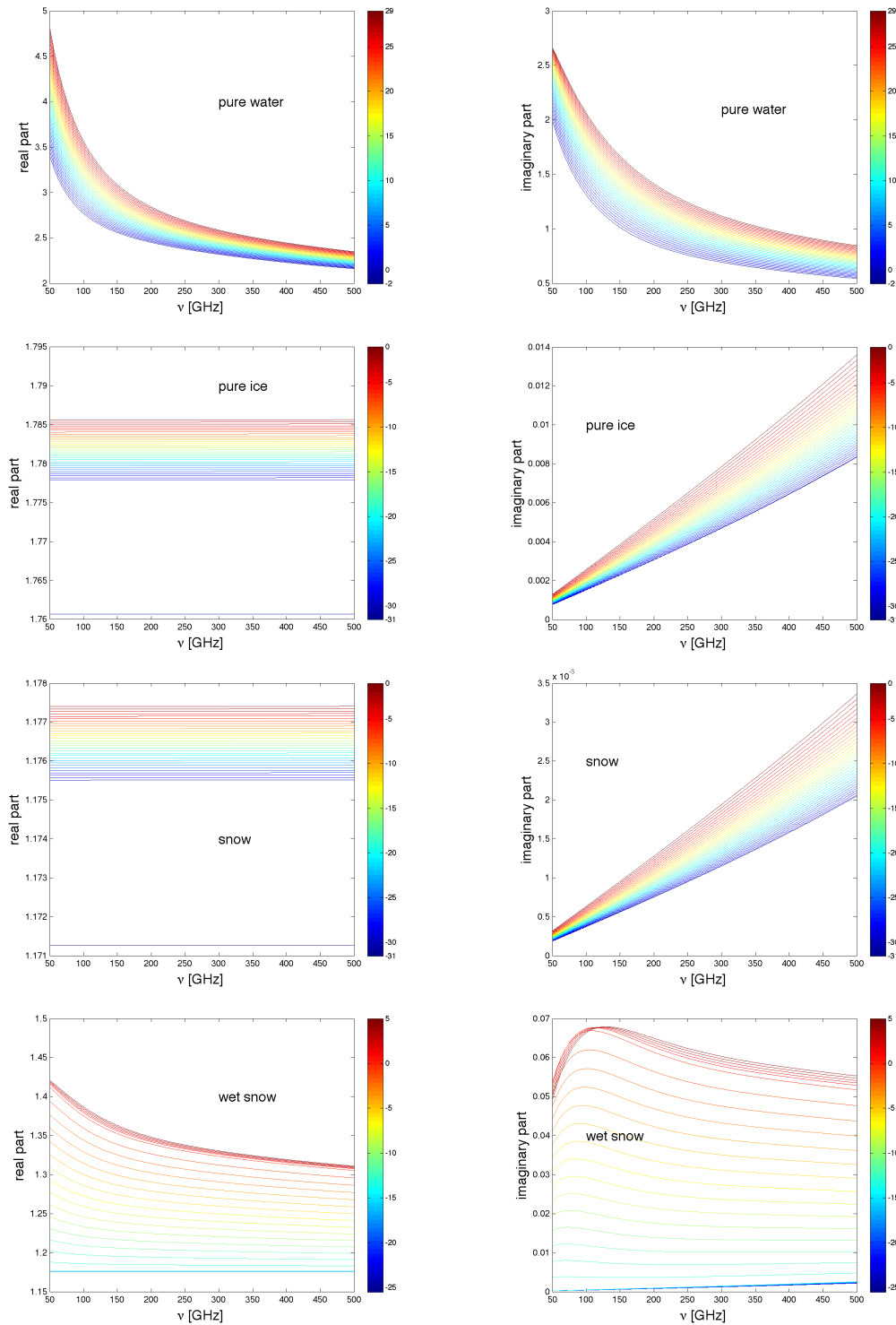


Figure 2.7: Real (left) and imaginary (right) part of the dielectric constants for fresh water, pure ice, snow, and wet snow from top to bottom, respectively. The values were calculated between 50 and 500 GHz with the formulas given in section 2.7. The respective colorbar indicates the temperature variation in degrees Celsius. For the calculation of the constants for snow and wet snow a snow density of  $0.2 \text{ gm}^{-3}$  has been assumed.

where  $\theta = 300/T - 1$ . The parameter  $\beta$  is defined by

$$\beta = \frac{0.0207}{T} \frac{\exp(335/T)}{(\exp(335/T) - 1)^2} + 1.16 \cdot 10^{-11} \nu^2 + \exp(-9.963 + 0.0372(T - 273.16)). \quad (2.55)$$

To calculate the dielectric constants for heterogeneous hydrometeors, like snow or graupel as composites of ice and air, some dielectric mixing theory is required. For precipitation-sized particles, the explicit Maxwell-Garnett mixing formula is often used. It gives the effective dielectric constant of a mixture as a function of the dielectric constants of the host material and of the inclusions. For snow and graupel, the host material is air ( $\varepsilon_0$ ) with ice inclusions ( $\varepsilon_1$ ), so that the effective permittivity  $\varepsilon_{eff}$  (*Skofronick-Jackson et al.*, 2002) is given by

$$\varepsilon_{eff} = \varepsilon_0 + \left( 1.0 + \frac{3.0v \left( \frac{\varepsilon_1 - \varepsilon_0}{\varepsilon_1 + 2\varepsilon_0} \right)}{1 - v \left( \frac{\varepsilon_1 - \varepsilon_0}{\varepsilon_1 + 2\varepsilon_0} \right)} \right), \quad (2.56)$$

with  $v$  being the temperature dependent volume fraction of the inclusion (*Sihvola*, 1989). As shown in Fig.2.7, the frequency dependence of the refractive index of snow is similar to the one of pure ice but with smaller magnitudes due the host material air.

Melting snow particles form a mixture of water and snow, where the snow itself is a mixture of ice and air. The impact of snow wetness can be considered by defining a wetness parameter and applying the Maxwell-Garnett mixing formula (Eq.2.56) twice. The wetness percentage  $W$  of such particles is a temperature dependent parameter given by *Skofronick-Jackson et al.* (2002) as

$$\begin{aligned} W(\%) &= 0 && \text{for } T \leq 258.15K \\ W(\%) &= (T - 258.15)/100. && \text{for } 273.15 > T > 258.15K . \\ W(\%) &= 15 && \text{for } T \geq 273.15K \end{aligned} \quad (2.57)$$

The parameter is used to transform ice into water. The inclusion of the wetness percentage has a strong impact on the imaginary part of the refractive index of the particles which translates in a stronger absorption. This influence is largest for temperatures close to the freezing point, as can be seen in Fig.2.7.

## 2.8 Radiative transfer model MWMOD

Accurate and computational efficient calculation of brightness temperatures is essential when setting up a database of hydrometeor profiles with corresponding brightness temperatures at microwave frequencies for retrieval development. If vertical profiles of standard

atmospheric variables and the various hydrometeor types are provided, such a model must be able to generate interaction parameters for absorption and scattering required by the radiative transfer calculations. The interaction parameters are often generated by applying approximation methods for the single-scattering properties, like the previously described T-matrix method or the DDA (sec. 2.4.2) or by the Lorenz-Mie theory for spheres. Once these parameters were generated, the VRTE needs to be solved to achieve brightness temperatures at the top of the atmosphere.

Various models exist within the microwave community to solve this problem. These models have been compared in various studies (e.g. *Kim et al.*, 2004; *Smith et al.*, 2002; *Kummerow*, 2001).

In this study, the radiative transfer model MWMOD by *Czekala and Simmer* (2002) is applied. The model has been used in many studies investigating the radiative transfer in cloudy and precipitating atmospheres (e.g. *Simmer*, 2004; *Czekala and Simmer*, 1998; *Czekala et al.*, 1999; *Crewell et al.*, 2005; *Mech et al.*, 2007). It solves the VRTE for the first two components of the Stokes vector. The reason for using only two components is that there is no coupling between the first and last two components of the Stokes vector due to the azimuthal symmetry of the problems under consideration. To solve the VRTE, an iterative method as described in section 2.6 in a plan-parallel one-dimensional atmosphere is applied. A set of propagation directions (mostly nine Gaussian angles per hemisphere) is used for the directional discretization of the radiation field. The gas absorption coefficients due to water vapor, molecular oxygen, and nitrogen are calculated using the Millimeter Propagation Model (MPM) code from *Liebe et al.* (1993). Optionally the model by *Liebe et al.* (1989) can be used. At millimeter- and submillimeter-wavelengths, many trace gases lead to spectral features. Therefore, absorption coefficients calculated with ARTS and BEAMCAT (see Fig. 2.3) can be added to the continuum absorption coefficients.

The single-scattering properties of hydrometeors can be either computed by Lorenz-Mie theory for spheres, by the Extended Boundary Condition Method (*Mishchenko et al.*, 1996), or by applying the approximation given by *Liu* (2004) as described in section 2.4.2. In this study, spherical particles were considered for most of the calculations, not only because of computational costs, but rather because the shape distribution of ice crystals, graupel, and snowflakes is quite uncertain. The single-scattering calculations provide solutions for the ASF which relates the scattered electro-magnetic wave to the incident plane wave. From the ASF, the interaction parameters are calculated and integrated over the azimuth angle, ending up with the appropriate values for one-dimensional radiative transfer. Finally, the results for particles of a certain size and shape are integrated over a particle size distribution to obtain the polydisperse scattering quantities in each atmospheric layer.

The radiative transfer code requires the emissivity at the surface. For continental surfaces, emissivity atlases have been calculated from SSM/I satellite observations up to 85.5 GHz (*Prigent et al.*, 1997) and serve as an input to MWMOD. Since the variation in the surface emissivity above 85.5 GHz is small, the emissivity at 85.5 GHz is used for calculations at frequencies above. Furthermore, the influence of surface emissivity at higher frequencies is rather weak due to the atmospheric water vapor absorption. Over sea surface, the FASTEM model by *English and Hewison* (1998) is used to calculate emissivities.

A more detailed description of the model can be found in *Czekala (1999)* and *Simmer (2004)*. A description of the procedure of generating brightness temperature calculations for large set of profiles will be given in chapter 4.

The brightness temperature results achieved with MWMOD are similar to those obtained by the RT model described by *Meirolid-Mautner et al. (2007)* and *Wiedner et al. (2004)* that will be used in chapter 4 for the evaluation with satellite observations. The maximum 3 K difference is attributed to the different gas absorption models used in both radiative transfer calculations. In the latter one the gas absorption is according to *Pardo et al. (2001)*, whereas the gas absorption model after *Liebe et al. (1993)* is used in MWMOD. For a more detailed description of the differences between different gas absorption models see *Melsheimer et al. (2005)*. Since the differences in cloudy scenes are negligible the uncertainty of the gas absorption model is not considered to be relevant for the study.

## 2.9 Sensitivity of simulated brightness temperatures to hydrometeors

In the previous sections it has been described how atmospheric constituents interact with radiation propagating through the atmosphere. When observing hydrometeors from satellites at microwave frequencies, the sensitivity of the observed brightness temperature to variations in hydrometeor contents is important to know. Furthermore, by simulating such observations, the sensitivity of the radiative transfer model to variations can be investigated.

The sensitivity study will be performed on the basis of atmospheric profiles taken from a cross section through a simulation with the CRM Méso-NH. The sensitivity of brightness temperatures to perturbations in hydrometeor contents,  $w$ , are expressed as Jacobians, i.e.

$$J_w = \frac{\Delta T_b}{\Delta w} = \frac{T_b(w + 10\%) - T_b(w - 10\%)}{(w + 10\%) - (w - 10\%)}, \quad (2.58)$$

where  $w$  is the hydrometeor content in  $\text{gm}^{-3}$  perturbed by  $\pm 10\%$  and  $T_b$  the brightness temperature in Kelvin. The Jacobian  $J_w$  is then given in  $\text{Kg}^{-1}\text{m}^3$ .

Examples of the hydrometeor contents in  $\text{gm}^{-3}$  are shown in Fig. 2.8 for the ELBE case on August 12, 2002 at 6 UTC (see sec. 5.1). The cross section is taken along  $\sim 13^\circ$  longitude from South to North with strong convection and encompasses 700 km in horizontal and 14 km in vertical extension. By this area only land surfaces are covered. Thus, the surface emissivity at all simulated frequencies is 0.93. Furthermore, all simulations refer to an observation angle of  $51.8^\circ$ .

Fig. 2.9 shows the Jacobians for 89, 150, and 176.31 GHz with respect to variations in snow content. As expected, an increase in the snow contents in upper layers results in a brightness temperature depression that is more pronounced the higher the frequency is. The positive response of the brightness temperature to increased snow contents in the

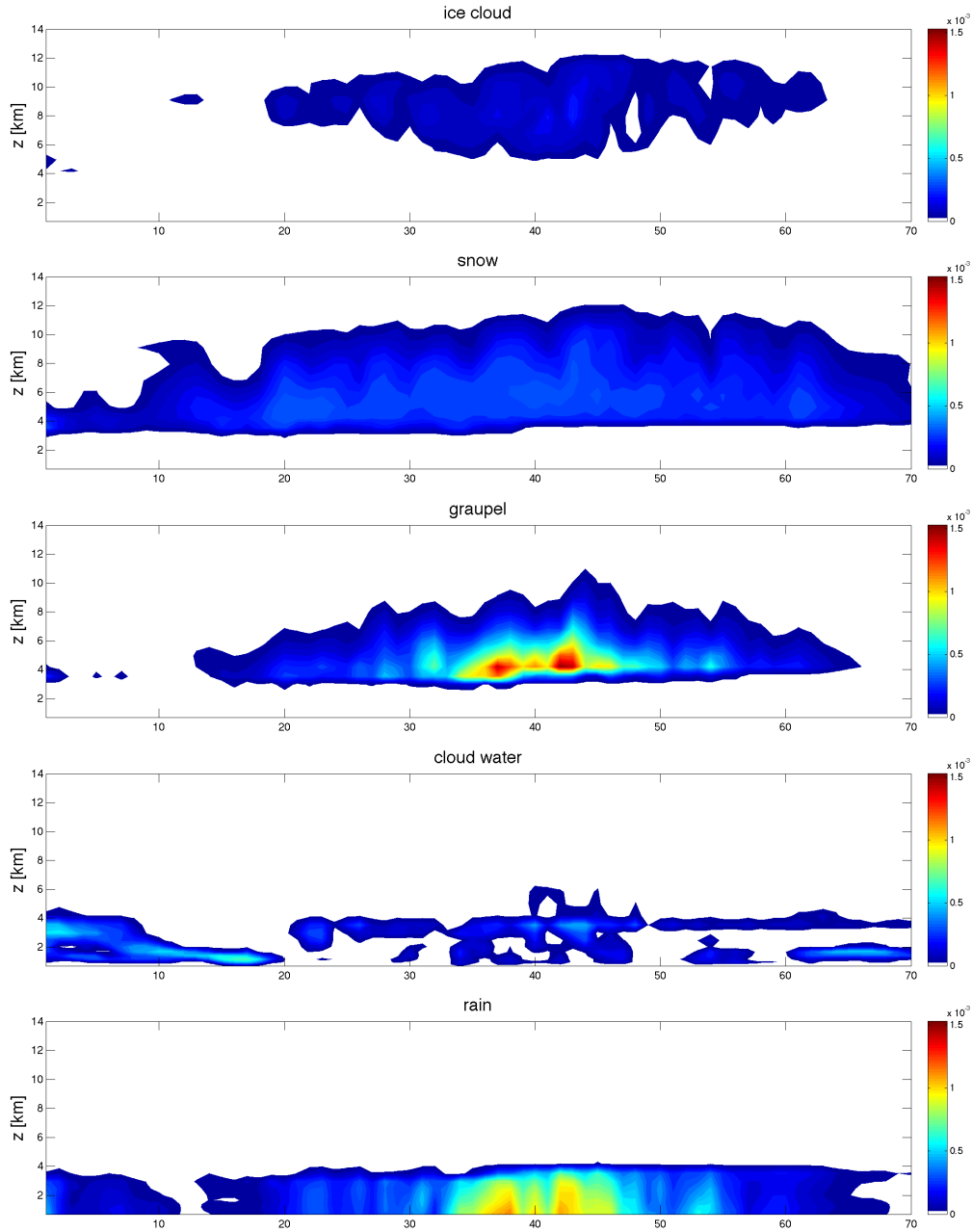


Figure 2.8: Cross section of hydrometeor contents [ $\text{gm}^{-3}$ ] of ice crystals, snow, graupel, cloud water, and rain water (from top to bottom) taken from a cross section through the ELBE case simulated with Méso-NH.

center of the simulation area in the lower levels are remarkable. This can be explained by an increased emission due to wet snow. The temperature in this layer is around  $-13^{\circ}\text{C}$  resulting in higher imaginary parts of the refractive index and therefore stronger emission (see Fig. 2.7). Moreover, below this snow layer high graupel and rain water contents can be found that caused a strong brightness temperature depression. The snow, graupel, and ice contents above this levels of positive Jacobians are dense enough to shade this effect. Furthermore, multiple-scattering effects between the layers underneath and above can be important. The areas with negative Jacobians in the North and South are due to an increase in scattering of the radiation that is not yet weakened by any strongly scattering or absorbing layer below. It can be also seen that the higher the frequency the more sensitive the simulated brightness temperature is to variations in snow contents. While at 89 GHz most response can be found in the lower snow layers, the signal at 176.31 GHz stems mostly from the upper layers due to stronger relative water vapor absorption.

The differential scattering effects of graupel is illustrated in Fig. 2.10. Here, the reduction in brightness temperature due to graupel variations at 150 GHz is two to three times higher than at 89 GHz. The scattering at 176.31 GHz is as well much more pronounced than at 89 GHz. At all frequencies the brightness temperature at the top of the atmosphere shows almost no sensitivity to variations in the area of highest graupel contents. This is due to dominating scattering in the layers above. In these layers high hydrometeor densities can still be found. Since graupel is assumed not to change its dielectric properties due to wetness like snow, no positive response occurs.

The Jacobians with respect to rain water (see Fig. 2.11) indicate no sensitivity in the area of strong convection due to the opacity and scattering, respectively, caused by snow and graupel content in the upper layers. At the North and South end of the simulation area, these "disturbing" hydrometeors are not present so that a response can be found. Since the surface emissivity is very high, the effect is expressed as negative Jacobians. Over ocean surfaces ( $\epsilon \approx 0.6$ ), an increase of rain water would result in a positive response of the brightness temperature due to the higher emissivity of the rain layer. The higher the frequency the less deep into the atmosphere can be seen and therefore the lower the detected effect is.

In general, higher frequencies are more sensitive to variations in frozen hydrometeor contents. The differential scattering that can be seen by comparing the effects at 89, 150, and 176.31 GHz for snow and graupel presents an excellent tool for the retrieval of frozen precipitation. Surface variations play a negligible role in the sensitivity at these frequencies. Similar results were found by *Bennartz and Bauer (2003)*.

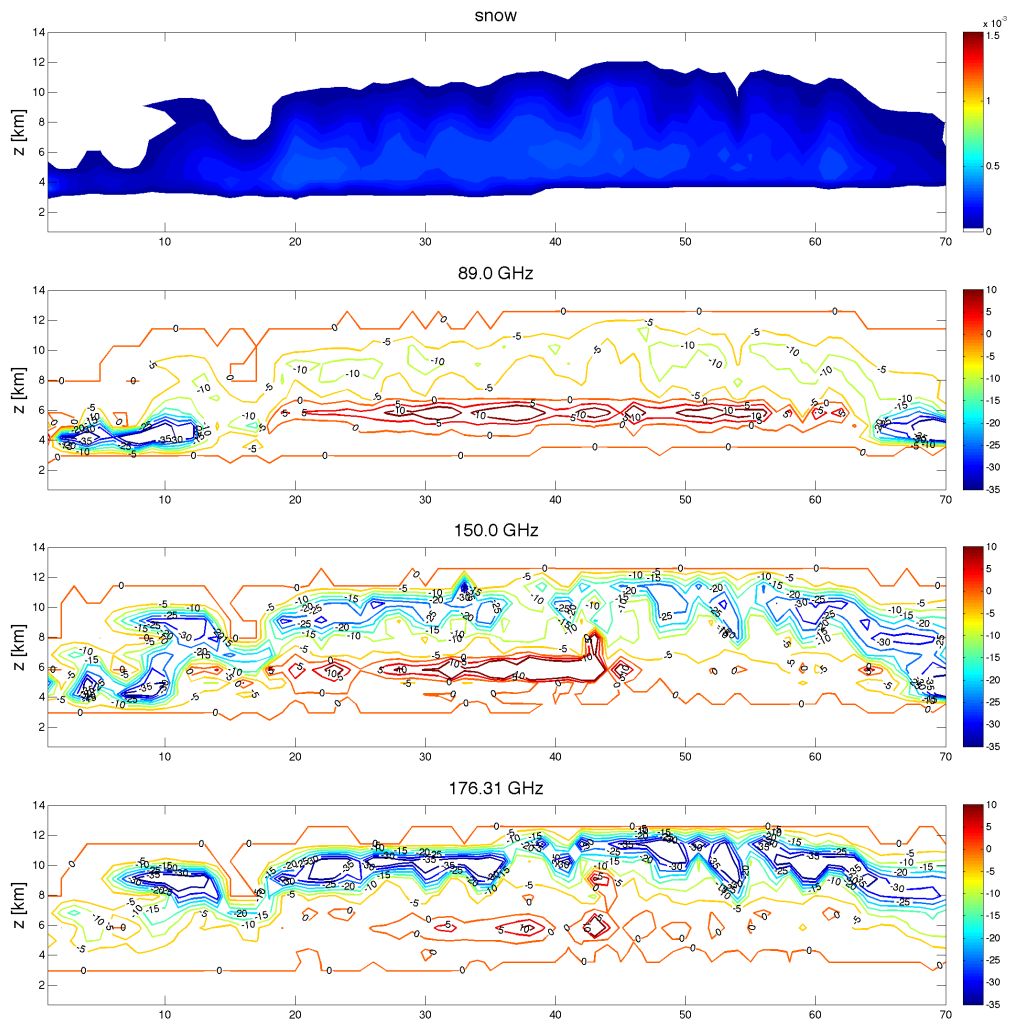


Figure 2.9: Jacobians [ $\text{Kg}^{-1}\text{m}^3$ ] for perturbations of the snow content (top) for the frequencies (from top to bottom) 89, 150, and 176.31 GHz.

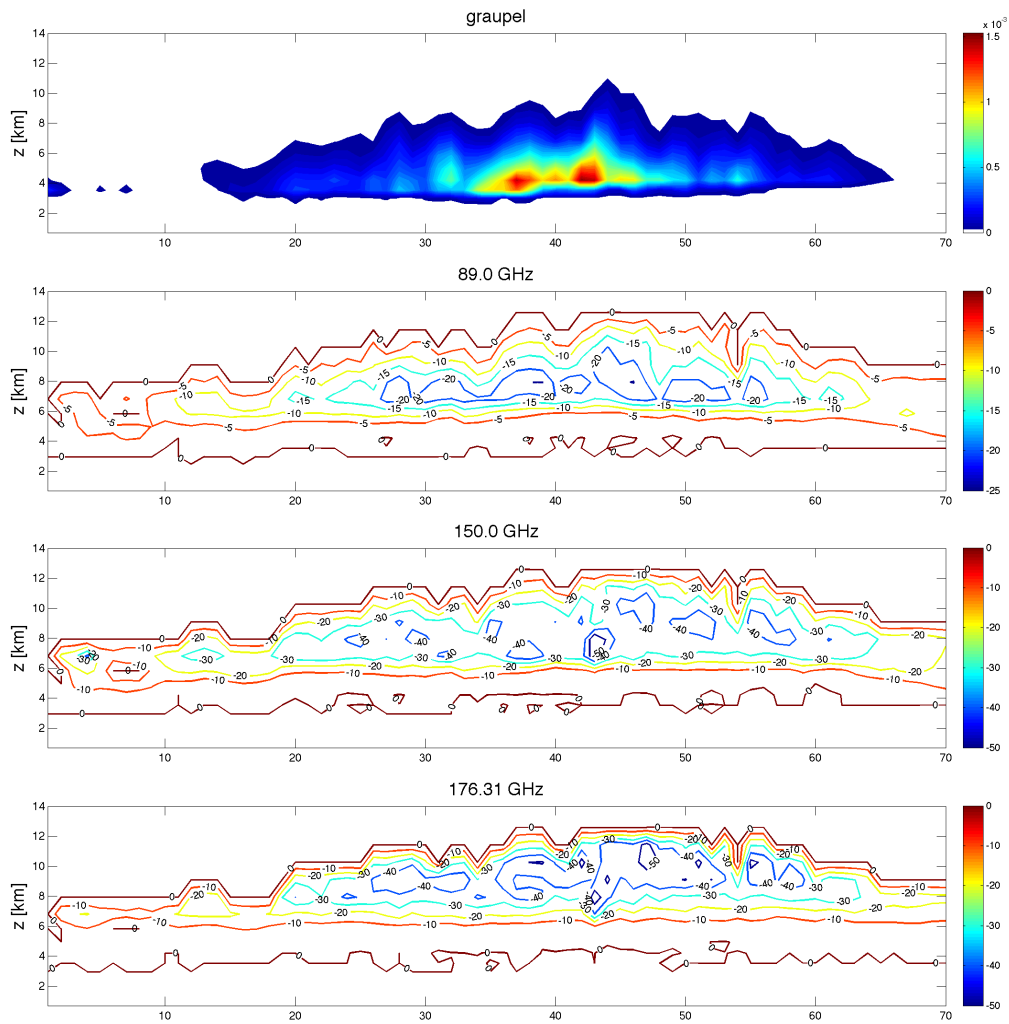


Figure 2.10: As Fig. 2.9 but for graupel.

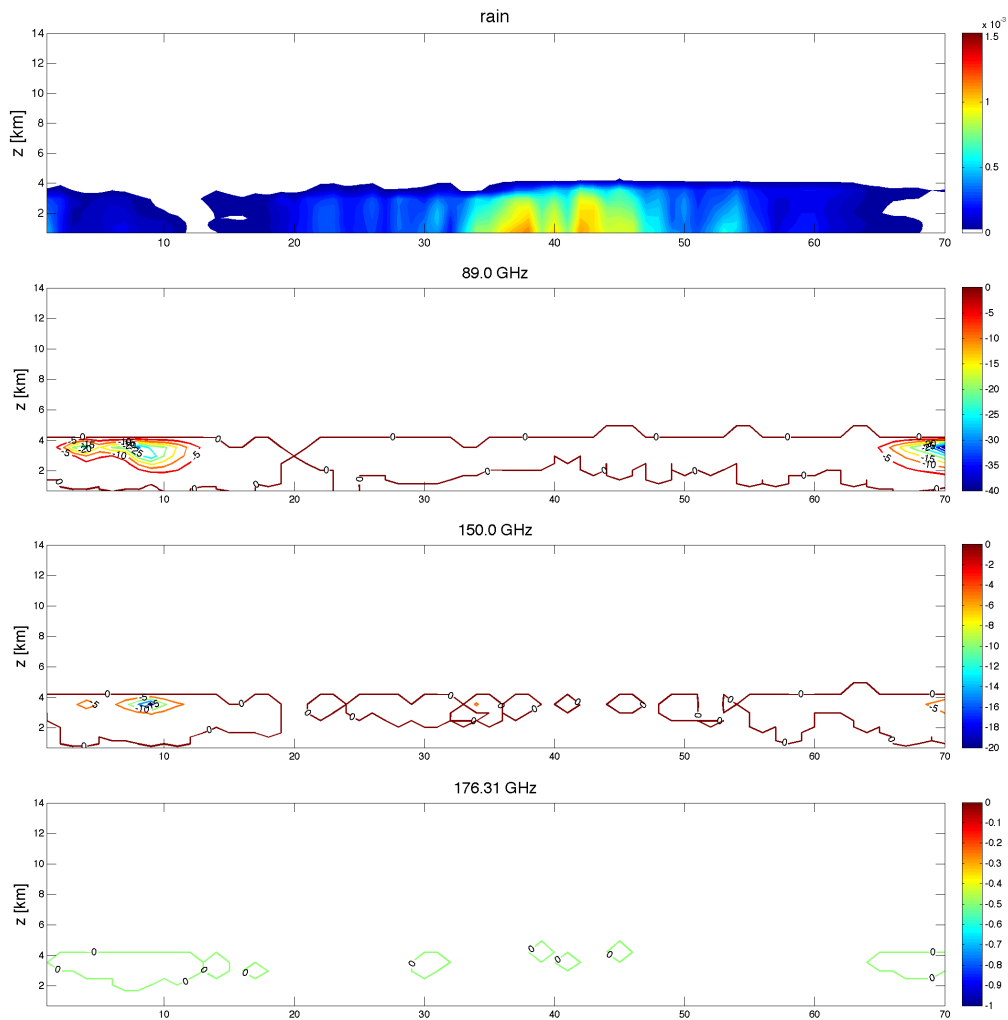


Figure 2.11: As Fig. 2.9 but for rain water content.



# Chapter 3

## Microphysics and CRMs

Microwave brightness temperatures are highly non-linear functions of surface properties, temperature, humidity, and gas profiles, and hydrometeor distributions. For example, in rainy atmospheres, the signal observed by a space-borne receiver at higher microwave frequencies would compose of radiation that has been emitted by the surface, the atmospheric gases, and the precipitating layer and scattered at the frozen particles in the upper parts of the cloud systems. It is thus very important that the simulated atmospheric and hydrometeor profiles reproduce as accurately as possible the whole atmospheric column in the precipitating situations when simulations of satellite measurements are performed.

Since no comprehensive and sufficient datasets of measurements of the relevant quantities exist, datasets of such parameters need to be generated by employing atmospheric models. In general, no detailed cloud microphysical parameterization is available in NWP models. Through CRMs it is possible to generate multi-dimensional distributions of the parameters required for the radiative transfer calculations. Furthermore, they provide spatial and temporal predictions of heat and water transfer in the atmosphere. Their detailed microphysical parameterizations of heat and water exchanges, and sources and sinks of several microphysical species (including cloud droplets, ice crystals, rain drops, snowflakes, and graupel) ensure that the hydrometeor fields are physically consistent and the vertical distribution of the hydrometeors is well correlated.

Choosing a specific CRM with its particular microphysical representation might be a limitation when trying to develop retrieval algorithms. Therefore, a variety of simulations with two different CRMs has been performed. In the first section, the different microphysical processes of formation and decay of hydrometeors will be described, followed by a section on cloud parameterization and representation of hydrometeors in CRMs.

## 3.1 Microphysics of clouds and precipitation

### 3.1.1 Hydrometeors

Hydrometeors are visible condensation products of water vapor of similar or different kind or shape, either hovering in the air (clouds) or falling towards the earth's surface (precipitation). The size range in diameters for liquid hydrometeors is between  $2\ \mu\text{m}$  and  $10\ \text{mm}$ , while particles  $\leq 50\ \mu\text{m}$  are named cloud droplets. Larger liquid particles are considered as rain drops (*WMO*, 1992). Frozen particles can have an extension from  $1\ \mu\text{m}$  for ice particles up to a couple of cm for snowflakes or hailstones.

To distinct the size of the various hydrometeors their geometrical extension or their mass can be considered. In case of liquid particles with moderate size, mass and geometrical extension are identical. This is not the case for very large falling rain drops and frozen particles (e.g. cloud ice, graupel, snow). Depending on environmental conditions (temperature, available water vapor, dynamical regime) and their prevailing history, a variety of shapes of ice crystals can develop, where the axes of extension are very distinct. To correlate mass and diameter for such particles, detailed information about their density and their functional dependence between their axes needs to be known.

When physical properties of hydrometeors are described in models, this is often done in terms of the spectrum of particles as a function of the diameter, called drop size distribution (DSD) or particle size distribution (PSD). This spectrum is the result of the various interaction processes between the different existing hydrometeor classes, discussed in the following subsection.

### 3.1.2 Microphysical processes

The amount of available water vapor in the atmosphere is one of the key parameters in formation of clouds and precipitation. A parcel of wet air can become saturated due to adiabatic or diabatic cooling or due to mixing processes. To form small cloud droplets nucleation processes need to be initiated. If a droplet forms in the condensation process solely by water vapor, the nucleation process is termed homogeneous nucleation. To form stable droplets particles need to grow by coalescence until they reach the critical radius. The size of this radius depends on the supersaturation; larger supersaturation requires smaller particle sizes to reach stable conditions. For homogeneous nucleation, super saturation of several hundred percent is required. Such conditions are not observed in the atmosphere. It is more likely for cloud droplets to form on hygroscopic aerosols (condensation nuclei) by heterogeneous nucleation. By solving of particles having an affinity for water, surface tension is decreased, so that much smaller supersaturation is required to form stable or activated drops. Such a particle acting as a condensation core is termed cloud condensation nucleus (CCN). Since CCNs are always present in the atmosphere, condensation starts when the relative humidity barely exceeds 100%. The rate of droplet formation is therefore driven by number of CCNs available and not by the random collision of particles.

Existing drops can grow by diffusion of water vapor from the air to the water droplet

(condensation). Evaporation is the contrary process responsible for decreasing particle size: diffusion from water droplet to air. Due to the transition of phases, such diffusion processes are linked to release (condensation) or absorption (evaporation) of latent heat. It depends on the thermodynamic state of the atmosphere which of these processes is dominant.

In early stages of droplet development, the condensation process is the dominant growth process. Once droplets have grown so far that the gravitational force exceeds values larger than the buoyancy force acting on it, they begin to fall. Their terminal fall speed is reached, when the gravitational force is balanced by the drag force exerted on the drop. Gravitational force and drag force are both functions of the particle diameter so that different sized particles reach different settling speeds: larger particles have greater speeds and collect smaller particles by collision processes (coalescence). Collision processes are only significant in rain formation if larger particles ( $r > 10 \mu\text{m}$ ) are present and the particle size spectrum is broad enough.

The colder the temperature, the greater the likelihood is that ice crystals form by homogeneous or heterogeneous nucleation. Homogeneous nucleation due to freezing of pure water drops is possible at temperatures around  $-40^\circ\text{C}$ : only few liquid particles are observed in natural at this temperature. Growth through diffusion of water vapor from air to the crystal is called direct deposition. Depending on supersaturation and temperature, different sizes and habits of ice crystals can evolve. By sublimation ice crystals are evaporated to water vapor. Melting ice crystals can become liquid cloud droplets, and by freezing cloud droplets become ice crystals. Similar to the liquid phase, smaller ice crystals can be collected by larger ones (aggregation). Newly formed ice crystals can grow rapidly due to diffusion at the expense of evaporating water drops: air saturated with respect to a water surface is supersaturated with respect to an ice surface.

In warm clouds, the droplet growth is caused by coalescence processes, although coalescence does not guarantee particle growth: particles can bounce apart once they collided, remain together permanently, or coalescence temporarily and separate in smaller drops. Which process is dominant is dependent on collision speed and collision trajectories. The diffusion-condensation process, that dominates droplet growth initially, leads to a narrowing of the size spectrum, seemingly complicating the coalescence process. But the rate of coalescence increases because the collision efficiency increases rapidly as the drops in the spectrum grow. Large droplets can become unstable because it is not sure that surface tensions can hold the drop together for sizes larger than 3 mm. For droplet diameters larger than 6 mm the particle is unstable. This can lead to a break up in smaller droplets: the process limiting the drop size distributions at the larger end. Populations with broad spectrums are most likely to produce rain in short times.

In cold clouds with cloud top temperatures below  $-20^\circ\text{C}$ , ice particles are most likely present. In such clouds large ice particles can capture smaller super-cooled water droplets. If the droplets freeze immediately on the crystal, they form a coating rime (riming), leading to graupel. If the pace of freezing is slow, more dense structures like hailstones are formed. Ice crystals clumping together (aggregation) form snowflakes. Significant aggregation is possible only at temperatures warmer than  $-10^\circ\text{C}$ . Larger snowflakes consist of dendrites and thin plates signifying diffusional growth near water saturation, whereas columns and

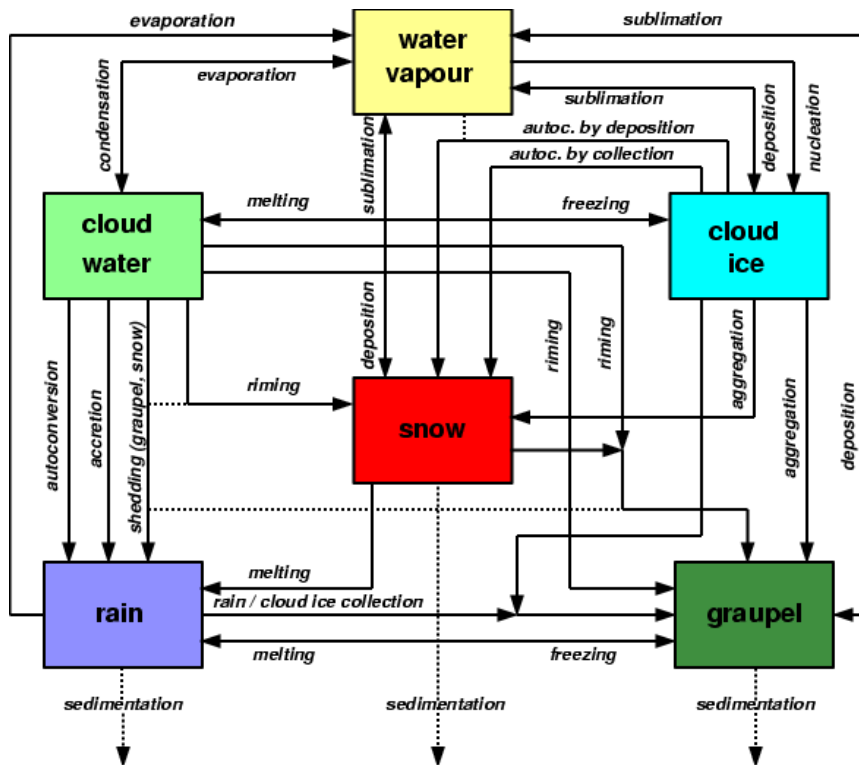


Figure 3.1: Cloud microphysical processes considered in the COSMO-DE three-category ice scheme as an example for the interacting processes (*Doms et al.*, 2004).

thick plates occur in cases of ice saturation.

It is possible that falling ice crystals reach the earth's surface without accretion and aggregation, although more likely snowflakes or graupel are observed in cold weather. But the dominant precipitation phase that occurs in the atmosphere is precipitation in form of rain drops: either developed in warm clouds or by frozen particles melting while falling down in layers with air temperatures above  $0^{\circ}\text{C}$ . The question, whether a droplet or crystal reach the ground, is dependent on the rate of evaporation or sublimation and on the size of the particle: rain drops with radius larger than  $r \geq 0.1\text{mm}$  are likely to contribute to the rain rate at the ground.

## 3.2 Hydrometeors in CRMs

In the previous section, the complex interaction processes between the various microphysical processes, involved in formation and decay of hydrometeors, has been discussed. A good representation of clouds, precipitation, and their interaction processes is essential for an accurate modeling of the atmospheric state. Cloud and precipitation development implies scales from synoptical to molecular. Explicit resolvable processes have spatial scales not smaller than the horizontal resolution of the model. With a grid space of less than

10 km, CRMs are able to explicitly simulate parts of the convection scheme. Cloud microphysical processes taking place on smaller scales are not explicitly simulated and have to be described by appropriate parameterization schemes. A challenging task not easy to fulfill.

Parameterizations are the formulation of the ensemble-effect of sub-grid scale processes on the resolved variables and in their terms. The processes under consideration are described by simple modeling and by closure conditions: the parameterizations are linked to the explicitly resolved processes. For a parameterization method to be well-posed and to avoid a mixture of resolved and parameterized scales in the simulations, a gap in space and time between both considerations is required.

In general, there are two different approaches for the numerical description of cloud microphysics, all based on budget equations for the water categories considered in the microphysical scheme. The ensemble of such equations is often called water continuity model and allows to predict the water mass and its changes due to various sources and sinks throughout the formation and decay of hydrometeors.

Although computational very demanding, the most direct approach is the spectral water continuity or explicit model (e.g. *Khain and Sednev, 1996*). Herein the ensemble of hydrometeors of one type or habit is subdivided in size categories. The number of particles in each category is predicted using budget equations for the number-density size-distribution function. Since many microphysical principles can be applied directly to the calculation of the size distributions, this method is well-suited to represent microphysical processes in dynamical models. However, many diverse hydrometeor types associated interaction processes and, for an accurate modeling, a discretization in hundreds of size bins makes this method very complex and therefore impractical.

More appropriate for nowadays computer capabilities is the representation of cloud microphysical processes in terms of moments of the PSD. In these bulk or parameterized water-continuity models, the atmospheric hydrometeors are subdivided in as few as reasonable categories and described by moments of their assumed size distributions. The equations of the microphysical processes must be parameterized in terms of the directly predicted total mass fraction  $q_h$  in each category (the index h is a place holder for the hydrometeor categories).

The basic assumption herein is, that the evolution of a particle spectrum can be approximated by varying the free parameters (related to the moments of the size distribution function) of an assumed specific mathematical function for the spectrum. In its simplest form, bulk water-continuity models use only the first moment of the size distribution (the particle dimension). For non-precipitating particles, the spectrum is assumed to be mono-disperse, whereas precipitating particles follow a negative exponential function in size

$$f_h(D_h) = N_0^h e^{-\lambda_h D_h}, \quad (3.1)$$

with the particle diameter  $D_h$  (for non-spherical particles this is sometimes the diameter of largest extension) as spectral coordinate and the intercept parameter  $N_0^h$ . The free

parameter of this distribution is the slope parameter  $\lambda_h$ , that can be determined from the integral over the mass distribution  $m(D_h)$  of the predicted mass fraction

$$q_h = \frac{N_0^h}{\rho} \int_0^\infty m(D_h) \exp(-\lambda_h D_h) dD_h. \quad (3.2)$$

Through Eqs. 3.1 and 3.2, the source and sink terms in the budget equations for the mass fraction can be formulated by taking into account the impact of the PSDs.

It was found by *McCumber et al.* (1991) that in addition to the two liquid categories (cloud water and rain) at least three different ice types are necessary to cover most of their precipitation studies. These are cloud ice as well as precipitating snow and graupel. These five categories are considered in the hydrological cycles of the applied CRMs (MésO-NH and COSMO-DE) and are treated as prognostic variables. Although their microphysical schemes are formulated for similar water categories (water vapor, cloud water, cloud ice, snow, graupel, and rain), the description of microphysical processes and particularly the particle size spectrums are quite different resulting in different hydrometeor contents and distributions.

In the following two subsections, the models used in this thesis and their assumptions in the size and mass spectrums for the five hydrometeor categories will be described.

### 3.2.1 Méso-NH

The non-hydrostatic mesoscale cloud model Méso-NH (*Lafore et al.*, 1998), jointly developed by Météo-France and the Centre National de la Recherche Scientifique (CNRS), is the research model of the French community. It is a CRM ranging from the meso- $\alpha$ -scale down to the micro-scale, based on an advanced anelastic system. It has interactive grid-nesting capabilities. The equations are horizontally discretized on a conformal projection system (preserves angles locally) with terrain-following vertical coordinate. The model is initialized and fed at the boundaries with analysis from the ECMWF model. In 2008, the AROME (Applications of Research to Operations at Mesoscale) model, that is based on the physical core of Méso-NH, will become the operational forecast model of the French weather service Météo-France, where it will be operated on 2.5 km horizontal resolution.

To simulate the microphysics inside pure warm clouds and the processes occurring in the low level deep convection, the Kessler scheme (*Kessler*, 1969) was implemented. A mixed-phase microphysical three-class ice scheme for the processes in ice clouds (cirrus) and heavily precipitating deep convection, for example, was developed by *Pinty and Jabouille* (1998) based on the approach of *Lin et al.* (1983). The microphysical scheme describing the interaction between the various hydrometeor classes is similar to the one for the COSMO-DE microphysics shown in Fig. 3.1. In the applied version, the complete microphysical scheme predicts the evolution of the mixing ratio (mass of water per mass of dry air) of five hydrometeor categories: cloud droplets, rain drops, pristine ice crystals, snowflakes, and graupel. The concentration of the pristine ice crystals is diagnosed. The concentration of the precipitating water drops, snow, and graupel is parameterized according to *Caniaux*

*et al.* (1994). The assumptions made on the PSDs are based on the scientific documentation of Méso-NH (see *Lafore et al.*, 1998 and *Pinty and Jabouille*, 1998).

In the Méso-NH microphysical scheme, the description of the spectrums is done with respect to the particle diameter  $D$ . Therefore all particles are assumed to be spheres, although the respective mass-size relation implicitly assumes a non-sphericity. The concentration of the PSD is parameterized with a total number concentration

$$N_h = C\lambda_h^x, \quad \text{where} \quad N_0^h = N_h\lambda_h. \quad (3.3)$$

The constants  $C$  and  $x$  are empirical adjustments drawn from ground and in situ measurements (see Tab. 3.2.1).  $\lambda_h$  is the afore mentioned slope parameter. For  $x = 0$  the total number concentration is held fixed, while for  $x = -1$  this corresponds to the intercept parameter ( $N_0^h \equiv C$ ) of the Marshall-Palmer distribution (Eq. 3.1). For the description of the different hydrometeor categories and the corresponding PSDs the relation between the mass and their sizes is essential

$$m(D) = aD^b. \quad (3.4)$$

By defining the relation in Eq. 3.4, the deviation from sphericity is implicitly assumed for the three ice categories. The velocity size relation is given by  $v = cD^d$ .

The size distribution of the hydrometeors follows a generalized Gamma distribution

$$\begin{aligned} n(D)dD &= N_h g(D)dD \\ &= N_h \frac{\alpha}{\Gamma(\nu)} \lambda_h^{\alpha\nu} D^{\alpha\nu-1} \exp(-(\lambda_h D)^\alpha) dD, \end{aligned} \quad (3.5)$$

where  $g(D)$  is the normalized distribution and  $\alpha$  and  $\nu$  are adjustable parameters. For  $\alpha = \nu = 1$  Eq. 3.5 reduces again to the Marshall-Palmer distribution law given in Eq. 3.1.

The ice and water contents for the different hydrometeor categories can be defined by the integral

$$\rho q_h = \int_0^\infty m(D)n(D)dD = aN_h M(b) \quad (3.6)$$

where Eq. 3.4 has been used and  $M(p)$  is given by the moment formula

$$M(p) = \int_0^\infty D^p g(D)dD = \frac{G(p)}{\lambda_h^p} = \frac{1}{\lambda_h^p} \frac{\Gamma(\nu + p/\alpha)}{\Gamma(\nu)}, \quad (3.7)$$

for the calculation of the  $p^{\text{th}}$  moment of the size distribution. Therein  $G(D)$  is the generalized Gamma law.

Category	$\alpha$	$\nu$	$a$	$b$	$c$	$d$	$C$	$x$
$q_c$	3	3	524	3	$3.2 \times 10^7$	2		
$q_i$	3	3	0.82	2.5	800	1		
$q_s$	1	1	0.02	1.9	5.1	0.27	5	1
$q_g$	1	1	19.6	2.8	124	0.66	$5 \times 10^5$	-0.5
$q_r$	1	1	524	3	824	0.8	$10^7$	-1

Table 3.1: Parameters of the PSD of the Méso-NH microphysical scheme after *Caniaux et al.* (1994).

The slope parameter can be deduced from Eq. 3.6 by inserting Eqs. 3.3 and 3.7

$$\lambda_h = \left( \frac{\rho q_h}{aCG(b)} \right)^{\frac{1}{x-b}}. \quad (3.8)$$

Tab. 3.2.1 provides the parameters used in the previous relations for all three ice categories, cloud water, and rain.

The model Méso-NH is used in this study for the simulation of the atmospheric state of mid-latitude precipitating cases (see sec. 5.1) on a 10 km horizontal resolution with 25 vertical layers between the surface and the model top at 20 km. The model output includes the full three dimensional description of the atmospheric parameters (pressure, temperature, 10 m wind speed, surface temperature, and the mixing ratios for water vapor and the five hydrometeor categories) needed for the radiative transfer calculations. The simulations performed with Méso-NH form the background for the database of hydrometeor profiles and corresponding brightness temperatures at different microwave frequencies (see sec. 5.4), used for the retrieval studies in chapter 6.

The quality of the cloud scheme used in Méso-NH was assessed by using space-borne sensors at various wavelengths in many investigations (e.g. sec. 4.3 and *Chaboureau et al.*, 2000; *Chaboureau et al.*, 2002; *Chaboureau et al.*, 2007; *Meirolid-Mautner et al.*, 2007; *Wiedner et al.*, 2004; *Ducrocq et al.*, 2002; *Richard et al.*, 2003) showing that neither strong nor systematic deficiencies are present in the microphysical scheme and the prediction of the precipitating hydrometeor contents.

### 3.2.2 COSMO-DE

The mesoscale cloud resolving model COSMO-DE (formerly known as Lokal-Modell kürzestfrist, LMK) is based on the COSMO-model (*Steppler et al.*, 2003; *Doms and Schättler*, 2002). It is a fully-compressible, non-hydrostatic limited-area atmospheric prediction model. Together with the global model (GME) and the COSMO-EU (horizontal mesh size 7 km), it is the operational NWP system of the German Weather Service (Deutscher Wetterdienst, DWD) since April 2007. The COSMO-model is based on the primitive thermo-hydrodynamical equations describing compressible flow in a moist atmosphere on

the meso- $\beta$ - (20-200 km) and meso- $\gamma$ -scale (2-20 km). The model equations are formulated in rotated geographical coordinates and a generalized terrain-following vertical coordinate with highest resolution close to the surface. Discretization is done spatially by finite differencing operators and corresponding atmospheric prognostic variables are stored on an Arakawa-C-grid: thermodynamic quantities (e.g. temperature, pressure, humidity, five bulk water quantities) are evaluated at the centers and dynamic quantities at the boundaries (e.g. wind vector, turbulent kinetic energy, diffusion coefficients). In its operational mode, it runs on 2.8 km horizontal resolution with a domain size of  $461 \times 421$  grid-boxes on 50 vertical layers.

A variety of physical processes are taken into account by parameterization schemes. It is assumed that at least the larger-scale elements of the convection are explicitly simulated by the model resolution. Therefore, the deep convection parameterization scheme is switched off. For the moist convection, acting on smaller scales, the cumulus parameterization scheme after *Tiedke* (1989) has been implemented. The grid-scale cloud microphysics are parameterized by a three-category ice scheme as shown in Fig. 3.1: warm clouds are parameterized after *Kessler* (1969) and the basic idea for the parameterization for ice-categories is based on the work by *Lin et al.* (1983) and extended and modified as described in *Doms et al.* (2004). The mixing ratios of cloud water, cloud ice, snow, graupel, and rain are considered as prognostic variables. A complete description of all parameterizations, including the processes for the interaction between the five categories of the microphysical scheme, can be found in *Doms et al.* (2004) and therein cited articles.

In the microphysical scheme, precipitating particles are assumed to be negative exponentially distributed with respect to the particle diameter  $D$  given in Eq. 3.1, or to the length of maximum extension  $D_h$ . Essential for the shape of the distribution for the different hydrometeor types is the slope parameter  $\lambda_h$ . It is strongly connected to the mass-size relation

$$m(D_h) = a_m^h D_h^b, \quad (3.9)$$

and the empirically determined intercept parameter  $N_0^h$  and can be deduced from Eqs. 3.1, 3.2, and 3.9

$$\rho q_h = a N_0^h \int_0^\infty D_h^b \exp(-\lambda_h D_h) dD_h = \Gamma(b+1) \frac{a_m^h N_0^h}{\lambda_h^{b+1}}. \quad (3.10)$$

Herein, the defined Gamma-function

$$\Gamma(z) = \int_0^\infty t^{z-1} e^{-t} dt \quad (3.11)$$

and the substitution  $t = \lambda_h D_h$  has been used. From Eq. 3.10, the slope parameter for any PSD in the COSMO-DE microphysical scheme can be formulated as

Category	$a_m^h$	$b$
$q_s$	0.038	2
$q_g$	169.6	3.1
$q_r$	$\pi/6\rho_w$	3
$q_i$	130	3

Table 3.2: Parameters of the PSD of the COSMO-DE microphysical scheme after *Doms et al.* (2004) with  $a_m^h$  in  $\text{kgm}^{-b}$  being a particle specific form factor and  $\rho_w$  the bulk density for water.

$$\lambda_h = \left( \Gamma(b+1) \frac{a_m^h N_0^h}{\rho q_h} \right)^{\frac{1}{b+1}}. \quad (3.12)$$

The parameters  $a_m^h$  and  $b$  are given in Tab.3.2.2 and are different from the parameters for Méso-NH.

For rain drop distributions,  $N_0^r$  is fixed at  $8 \times 10^6 \text{m}^{-4}$  and particles are assumed to be spherical with diameter  $D$ . Snow is assumed to be in the form of densely rimed aggregates of dendrites. Based on *Locatelli and Hobbs* (1974), the mass-size relation for snow can be approximated by Eq.3.9 with  $a_m^s = 0.038 \text{kgm}^{-2}$  and  $b = 2$  (see Tab.3.2.2). The distribution for snow particles is described in terms of the maximum dimension of the particles  $D_s$  related to the water-equivalent diameter  $D$  through

$$D_s = D^{3/b} \left( \frac{\pi \rho_w}{6a_m^s} \right)^{1/b}. \quad (3.13)$$

It is known that the size distribution of snow crystals varies with altitude and air temperature. Thus, in contrast to the rain drop distribution, the intercept parameter  $N_0^s(T)$  for snow particle distributions is assumed not to be constant anymore. *Field et al.* (2005) developed power laws based on aircraft measurements relating moments of the size distribution, so that the PSDs can be scaled for a given air temperature. The scaling is done by formulating  $N_0^s(T)$  as a function of temperature. Details can be found in their work (*Field et al.*, 2005).

Graupel particles (see *Heymsfield and Kajikawa*, 1986) are assumed to be close to spherical but with reduced densities. The mass-size relation is given by Eq.3.9 with  $a_m^g = 169.6 \text{kgm}^{-3.1}$  and with respect to the maximum dimension  $D_g$  related to the water-equivalent diameter  $D$  by

$$D_g = D^{3/b} \left( \frac{\pi \rho_w}{6a_m^g} \right)^{1/b}. \quad (3.14)$$

The intercept parameter is fixed at  $N_0^g = 4 \times 10^6 \text{mm}^{-4}$ .

The distribution of non-precipitating particles cloud water droplets and ice crystals (cloud ice) is assumed to be mono-disperse. The mean crystal mass is defined as  $m_i = \rho q_i N_i^{-1}$ , where  $N_i$  is the number of cloud ice particles per unit volume of air.  $N_i$  depends on ambient temperature. Its parameterization is based on aircraft measurements and is given by

$$N_i(T) = N_0^i \exp\{0.6(T_0 - T)\}, \quad \text{with} \quad N_0^i = 1.0 \times 10^2 \text{m}^{-3}. \quad (3.15)$$

Pristine ice crystals are assumed to be in the form of hexagonal plates with an aspect ratio of  $H/D_i = 0.2$ , where  $H$  is the second largest axis and the linear dimension  $D_i$  is smaller than about  $200 \mu\text{m}$ . The density of ice crystals is assumed to be fixed at  $0.913 \text{gcm}^{-3}$  and the mass-size relation of cloud ice particles is given by Eq. 3.9 with  $a_m^i = 130 \text{kgm}^{-3}$  and  $b$  from Tab. 3.2.2.

### 3.2.3 Comparison of the PSD

Cloud microphysical processes can be described in CRMs by different schemes, distinct from each other by the number of hydrometeor categories, description of PSDs, and of the interaction processes between these classes. Although the microphysical schemes of Méso-NH and COSMO-DE both represent the atmospheric water categories by six classes and the PSDs follow a Marshall-Palmer like distribution, the shapes of the particles and mass-size distributions for each atmospheric layer for the same category can be quite different. Even the resulting distribution of the available water vapor into the different hydrometeor contents can show large differences. For instance, the Méso-NH scheme tends to produce more graupel contents on the expense of snow, whereas in the COSMO-DE scheme snow is the dominating precipitating frozen hydrometeor category.

By comparing the PSDs of the Méso-NH and the different interpretations of the COSMO-DE schemes (Fig. 3.2.3) it can be seen, that the snow and graupel distribution for Méso-NH and COSMO-DE with respect to largest dimension show significant differences. For snow the distribution used in COSMO-DE has a larger intercept parameter (remember  $N_0^s$  is temperature dependent for snow in the COSMO-DE scheme) with a steeper slope than the Méso-NH resulting in particle concentration at smaller particles, whereas for graupel it is the other way around.

Since the single-scattering properties of the different sizes of snow and graupel differ significantly, the shape of PSDs and the distribution within the different hydrometeor categories can have large impact on radiative transfer calculations in the microwave region.

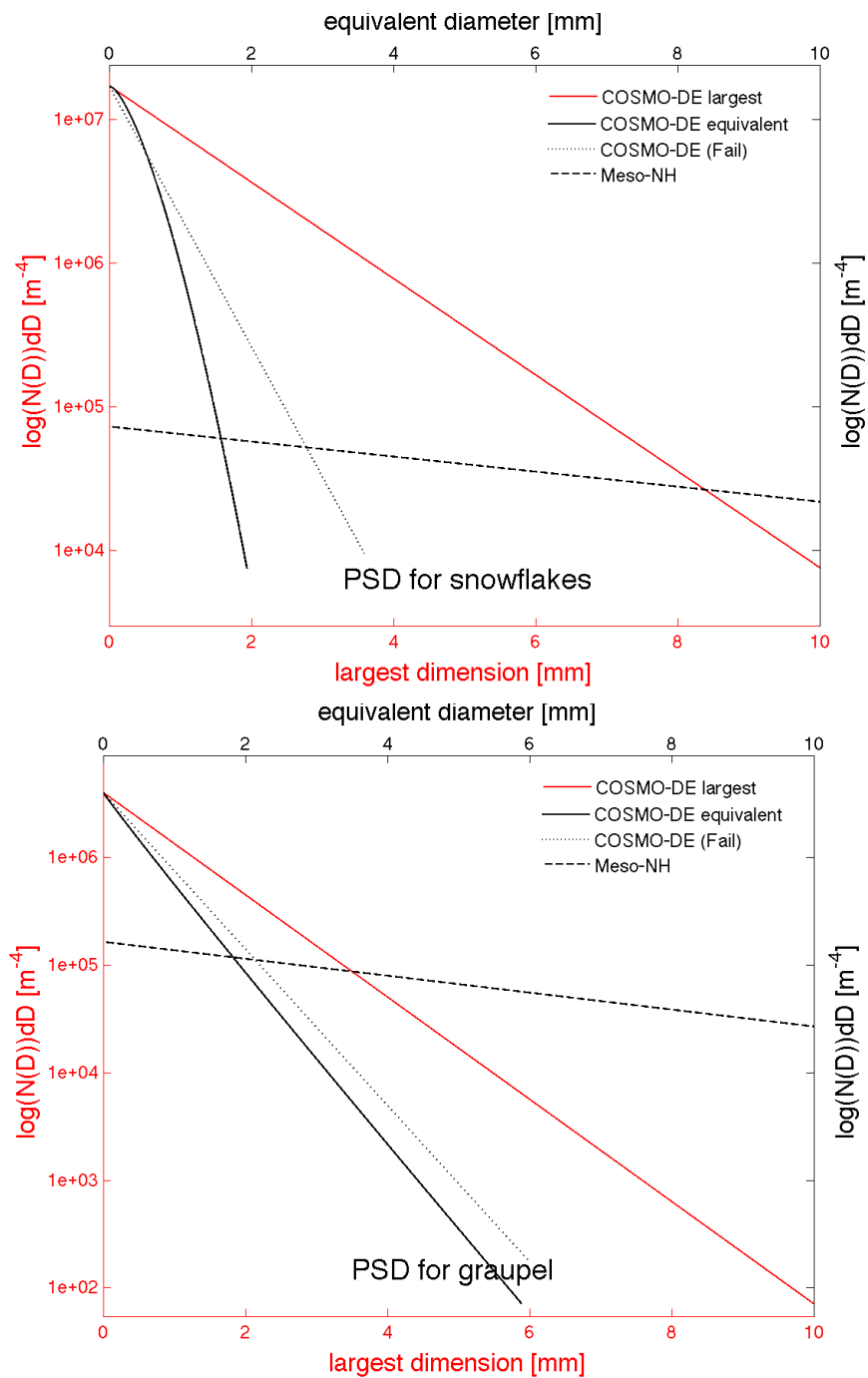


Figure 3.2: Particle size distribution of snowflakes (top) and graupel particles (bottom) for a mixing ration of  $3 \times 10^{-3}$  at 265 K. The red line shows the distribution for the COSMO-DE microphysical scheme with respect to the largest diameter; black lines are with respect to spheres.

# Chapter 4

## Satellite simulator

When coupling CRM output with a RT model, all parameters relevant for radiative transfer need to be preprocessed to match the input requirements of the RT model. Thereby, it is important not to modify the physical correlations between the parameters, because this would arise unforeseeable errors. Especially when dealing with radiative transfer calculations with clouds and precipitation implied, the hydrometeor properties (size and shape distribution, phase, densities, and dielectric properties) need to be carefully matched to avoid any inconsistencies of microphysical parameterizations. Thus, the direct output of the CRMs, e.g. profiles of temperature, pressure, and humidity and surface properties of one grid cell have to be considered in the RT model. Before the bulk water contents of each hydrometeor category in one grid box can be included in the RT model they have to be distributed to the different particle diameters using the same assumptions as used in the microphysical parameterizations of the CRMs.

In the following chapter the Synthetic Satellite Simulator (SynSatMic; Fig. 4.1), together with a post-processor convoluting the simulated brightness temperature fields with the satellite observation characteristics, will be described in detail.

### 4.1 SynSatMic

For the simulation of brightness temperatures, the one dimensional RT model MWMOD (see sec. 2.8) is used. Therefore, vertical profiles of temperature, pressure, humidity, and bulk water contents, as well as the surface type, temperature, and wind speed for a specific vertical column need to be extracted from the CRM output. For the investigated satellite geometries and the employed horizontal resolutions of the CRM simulations, the extraction of the standard atmospheric variables is straight forward, since no slant path correction is necessary (i.e. an imaginary line drawn from satellite to any point within its footprint will not intersect two vertical columns). The pre-processing of the five water categories is much more difficult since the bulk water categories need to be described by appropriate PSDs in a physically consistent way with the microphysical schemes of the CRMs.

A critical point here is the discretization of the particle diameter. Using too few size bins

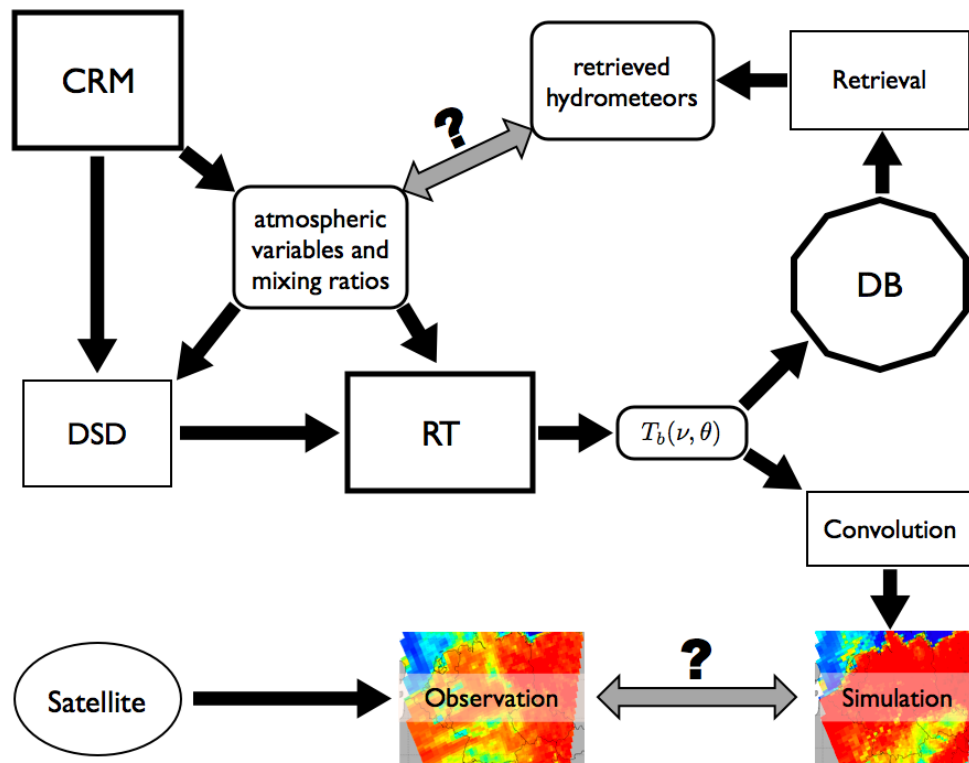


Figure 4.1: Schematic view of the model framework for SynSatMic and the retrieval database.

can lead to inaccuracies especially for strong variations of the Mie-Parameter (Eq. 2.29). In contrast, using too many bins strongly increases the computation time. Fig. 4.2 (left) shows the sensitivity of brightness temperature calculations in terms of percentages to variations in the number of discretization bins from two to 50, for frequencies used in this study and for a single layer with moderate snow content in a typical mid-latitude atmosphere. For frequencies close to absorption lines, the effect of the discretization number is negligible, since the hydrometeor signal is damped strongly by the absorbing gases above the snow layer. This effect would not have been so strong, if the simulations were performed for a hydrometeor layer in mid- to upper-tropospheric parts. In window regions an effect of increasing accuracy with increasing bin number can only be seen from two to ten with a maximum of 0.3% at 150 GHz, corresponding to  $\sim 0.35$  K. A further increase of the number of size bins has no significant effect on the accuracy of the brightness temperature calculations. On the other hand, for this increase in number of size bins and a relatively small gain of accuracy, the computation time doubles (Fig. 4.2, right). For even larger bin numbers and higher frequencies (more sensitive to scattering), the increase in computation time is enormous. For simulations with a typical atmospheric profile that contains several hydrometeor categories in a number of layers, both effects would amplify. But it is desirable to keep the bin number as small as possible to save computation time without losing too much accuracy compared to other model errors.

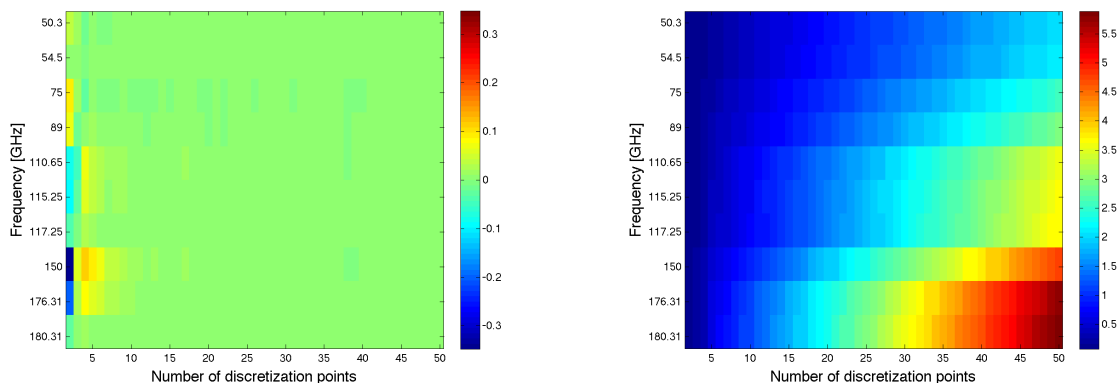


Figure 4.2: Sensitivity of brightness temperature to increase in number of bins at various frequencies (left) as percentage of the highest resolution. The brightness temperature resulting from the calculations with the highest number of discretization points is assumed to be the most accurate. Increase in computation time in seconds with increasing bin number (right). The calculations were performed with a single layer of snow particles (mixing ratio  $q_s = 3 \times 10^{-3}$ ) at 550 hPa and 265 K after the COSMO-DE microphysical scheme.

Hence, like in *Wiedner et al.* (2004) and *Meirolid-Mautner et al.* (2007), four different diameters as shown in Fig. 4.3 are used for the discretization of the snow, graupel, and rain distributions following the distributions described for Méso-NH and COSMO-DE in section 3.2, respectively. The density assumptions for the three hydrometeor types are derived from their mass-size relationship and the assumption for equivalent spheres. Hereby, an upper cut-off value of  $0.92 \text{ gm}^{-3}$  for the frozen precipitating particles is assumed, which means that there is a cut-off radius where the density becomes that of pure ice.

Since cloud droplets and ice cloud particles are small compared to the wavelength of interest, mono-disperse distributions with spheres are considered, where cloud droplets are assumed to have a diameter of  $20 \mu\text{m}$  and ice particles a diameter of  $60 \mu\text{m}$ , with densities of  $1 \text{ gm}^{-3}$  and  $0.92 \text{ gm}^{-3}$ , respectively. These values were also selected by the International Satellite and Cloud Climatology Program (ISCCP) for typical cloud droplets and non-precipitating ice particles (*Rossow and Schiffer*, 1999).

For the calculation of the single-scattering properties of the five hydrometeor types in the model, appropriate dielectric properties need to be considered. The liquid particles like rain and clouds are therefore described by the relation given by *Manabe et al.* (1987). For ice the refractive index is taken from *Warren* (1984). The Maxwell-Garnett formula (Eq. 2.56) is applied for the refractive index of snow and graupel as well as for melting snow with a temperature dependent wetness parameter. A sensitivity study investigating the impact of different descriptions of the dielectric properties is given in *Meirolid-Mautner et al.* (2007).

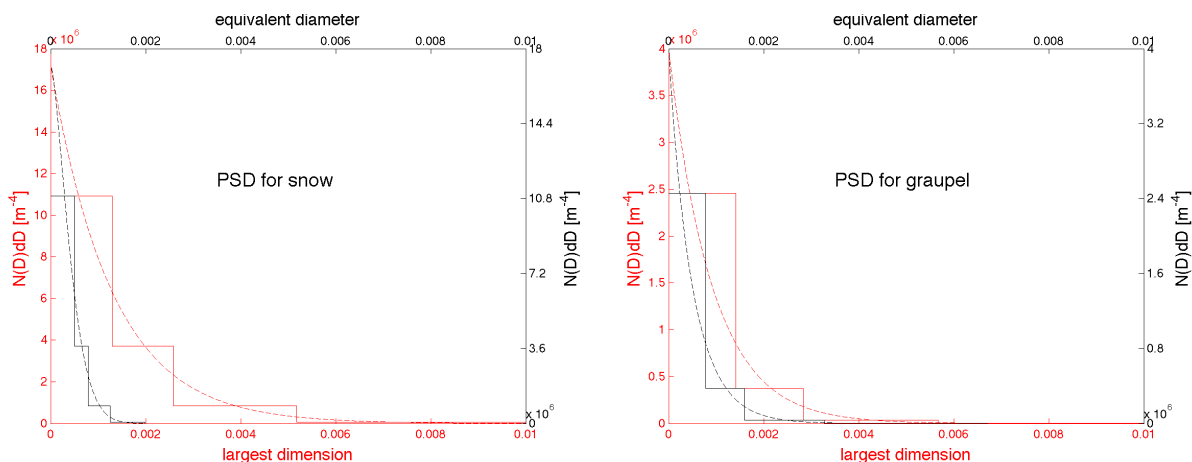


Figure 4.3: Comparison of the particle size distributions for the maximum extension (red) and the water-equivalent diameter (black) following the COSMO-DE parameterization. The dashed lines indicate the the particle size distributions after Eqs. 3.1 and 3.12: left side for snowflakes, right side graupel particles.

## 4.2 Adopting simulations to AMSU-B geometry

SynSatMic is designed to be a tool for simulating brightness temperature observations of recent satellites for evaluation purposes and to estimate the potential of future satellite sensors in the microwave range. In order to directly compare SynSatMic simulations performed on the CRM grid with satellite observations, it is necessary to have both datasets available on the same grid. Moreover, the antenna pattern function (APF) of the considered instrument and polarization sensitivity of the sensor have to be accounted for, when comparing the observations with the simulations. Thus, an algorithm needs to be applied on the simulations to spatially average the output fields to match satellite observations.

Unfortunately, not many instruments in the higher microwave region on satellites are available in our days, especially for the mid-latitudes and over land. Satellites operating in the lower microwave range exist more often. These are for example the TMI instrument on the TRMM with frequencies between 10.65 and 85.5 GHz dedicated for quantifying and observing precipitation in the tropics and the SSM/I instrument hosted by the DMSP satellite with frequencies between 19.35 and 85.5 GHz. Since both instruments have only sensors in the lower microwave region (with the exception of the 85.5 GHz sensor), they are only feasible for precipitation observations over the ocean. To retrieve precipitation over land, higher microwave frequencies need to be applied. Thus, for the evaluation of SynSatMic’s potential to simulate brightness temperatures in the higher microwave region, measurements needs to be considered which are as close as possible to this frequency range. The only routinely available measurements for such purposes are the one taken by the sensors of the AMSU-B instrument (*Robel, 2006*).

AMSU was first launched in May 1998 on board of the NOAA satellite NOAA-15. It consists of two modules, AMUS-A and -B. AMSU-A is equipped with 15 sensors between

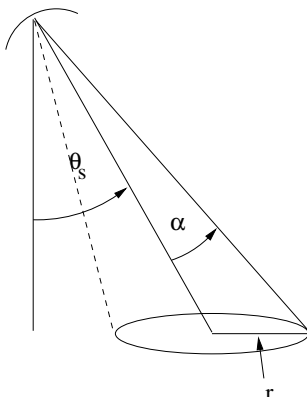


Figure 4.4: Geometry considerations for AMSU satellite observations.  $\theta_s$  is the scanning angle,  $\alpha$  the angle and  $r$  denotes the radius of the field of view, respectively.

23.8 GHz and 89 GHz, where twelve sounding channels (52-58 GHz) in the O<sub>2</sub>-band are used for retrieving atmospheric temperature profiles from 3 hPa to the earth's surface. Thereby, the retrieval of the temperature profiles utilizes the altitudes where the weighting functions of each channel have their maximum. AMSU-B is designed for humidity sounding and has two window channels at 89 and 150 GHz and three channels centered on the 183.31 GHz H<sub>2</sub>O-line. AMSU-A and -B are cross-track scanning instruments with a nominal field of view (FOV) of 3.3° and 1.15° (at the half power point) and sample 30 and 90 earth views, respectively. Thereby, the AMSU observation scan angle  $\theta_s$  varies from  $-48^\circ$  to  $+48^\circ$ , with a nominal orbit height of the polar-orbiting NOAA satellites of 833 km. This translates into a FOV of 50 and 16.3 km for AMSU-A and AMSU-B at nadir, respectively. The spatial resolution is fixed but changes with scanning angle.

Fig. 4.4 shows the viewing geometry for a satellite observing the earth's surface with an scanning angle of  $\theta_s$  and a FOV with angle  $\alpha$ . AMSU-B has a nadir resolution of 16.3 km that increases with off-zenith angles. The CRM simulations with COSMO-DE were performed on a horizontal resolution of 2.8 km. Therefore, a number of grid points lies within the FOV of one sample.

The receiver characteristics of the AMSU-B antenna can be assumed to resemble a Gaussian distribution defined by its standard deviation  $\sigma$  and mean  $\mu$ . An exact description of the measured APF can be found in *Robel (2006)*. The full width of half maximum (FWHM) of a Gaussian distribution can be derived to equal  $2.354\sigma$  corresponding to the FOV. Hence, the standard deviation describing the distribution yields  $\sigma = \text{FOV}/2.354$ . Since a Gaussian distribution is assumed and calculated centered at the boresight of the AMSU-B instrument, the mean value becomes  $\mu = 0$ .

As indicated in Fig. 4.4, all model grid points within a circle with radius  $r$  around the boresight of the sample have to be considered for the spatial averaging to match the brightness temperature observation. It is assumed that simulations for grid boxes with greater distances to the boresight have no significant influence on the brightness temperature observed for the considered sample. The radius  $r$  is defined as three times of

the standard deviation  $\sigma$ . This ensures that 99.73% of the population within the antenna characteristics is accounted for. A weighting factor is attributed to each of the simulations points within the circle with radius  $r$ . It is calculated from a Gaussian distribution with the distance to the boresight  $r'$ :

$$w_i = \alpha \cdot F_i(r'), \quad (4.1)$$

with the Gaussian distribution

$$F_i(r') = \frac{1}{\sqrt{2\pi}\sigma} \exp^{-\frac{r_i'^2}{2\sigma^2}}. \quad (4.2)$$

With the required presumption that the integrated Gaussian function is equal to unity

$$\int_{FOV} \alpha \cdot F(r') dr' = 1 \approx \sum_i \alpha F_i(r') = \sum_i w_i. \quad (4.3)$$

The normalization factor  $\alpha$  can be calculated by

$$\alpha = \frac{1}{\sum_i F_i(r')}. \quad (4.4)$$

As mentioned before, AMSU-B is a cross-track scanning instrument. Thus, the observation geometry depends on the zenith angle  $\theta_s$  of the boresight. For calculating the simulated observation of brightness temperature  $\langle T_b \rangle$  the following formulation needs to be applied:

$$\langle T_b \rangle = \sum_i w_i T_{b_i}(\theta_s, \nu), \quad (4.5)$$

with  $T_{b_i}(\theta_s, \nu)$  being the simulated brightness temperature for frequency  $\nu$  and point  $i$  within the FOV under the observation angle  $\theta_s$ . Since the AMSU-B instruments do not measure a specific polarization, the observed signal is a composition of vertical and horizontal polarization, defined after *Karbou et al.* (2005) as

$$T_{b_i}(\theta_s, \nu) = T_{b_i,h}(\theta_s, \nu) \cos^2(\theta_s) + T_{b_i,v}(\theta_s, \nu) \sin^2(\theta_s) \quad (4.6)$$

where  $T_{b_i,h}(\theta_s, \nu)$  and  $T_{b_i,v}(\theta_s, \nu)$  are the simulated brightness temperatures at horizontal and vertical polarization at frequency  $\nu$  for point  $i$ , respectively.

### 4.3 Comparison to SSM/I and AMSU-B observations

To evaluate the brightness temperatures achieved by the combination of a CRM and a RT model, comparisons to satellite measurements need to be performed. In such comparisons, different error sources are involved, especially from the modelers point of view. Hereby, differences between simulation and observation are most likely related to an incorrect representation of the atmospheric processes within the CRM, an inappropriate description of the hydrometeor properties and their distribution within the RT model, and inaccuracies in the calculation of the single-scattering properties.

To better analyze such discrepancies and to separate errors, different frequencies can be consulted due to their sensitivity to the various atmospheric components. For example, the lower microwave range in window regions is most sensitive to rain water and the surface contributions. Frequencies above 60 GHz respond through scattering at precipitating ice with a brightness temperature depression. Submillimeter-wavelengths are most sensitive to ice crystals in the mid- and upper-troposphere.

The comparisons presented here were made with the Atmospheric radiative Transfer Model (ATM) coupled to Méso-NH and have recently been published by *Meirolid-Mautner et al.* (2007). Comparisons between simulated brightness temperature fields achieved with SynSatMic and the ATM-Méso-NH combination showed agreement over the whole simulated frequency spectrum (*Crewell et al.*, 2005 and personal communication with the French group at l'Observatoire de Paris, <http://lerma.obspm.fr/>).

Figs. 4.5 and 4.6 show comparisons between satellite observations and simulations for the Hoek case on September 19, 2001 at 18 UTC (see sec. 5.1). It is quite unlikely that the polar-orbiting instruments SSM/I on the DMSP satellites or the AMSU-B sensors on the NOAA satellites have overpasses exactly at the simulation time. Thus, the closest overpasses were chosen, 1941 UTC for SSM/I and 1755 UTC for AMSU-B. For Meteosat, as a geostationary instrument measuring with a 15 min interval, appropriate observations will be available most of the time.

In general the simulated brightness temperature fields agree well with the observations: the global spatial structure of the brightness temperature fields are well captured with small displacements of the precipitation systems. This shows that the CRM Méso-NH is able to reproduce the thermodynamic nature of the precipitating system. This is pronounced as well by the comparison of the infrared simulation and observation in Fig. 4.6. Small scattered structures seen in the simulations over the Northern Sea are not present in the observations.

The overall agreement of the dynamic range of the microwave brightness temperatures is reasonable, showing that the RT model is able to simulated satellite observations. This does not hold for the simulation and observation in the higher window regions (85, 89, and 150 GHz). The scattering observed over central Germany (indicated by a strong brightness temperature depression) appears in the simulation with significant less intensity, especially at 150 GHz. Here, the sensitivity to scattering at frozen particles is strongest.

As afore mentioned this deficiency can have several reasons. First, the CRM can underestimate the frozen particle contents within this area. Second, the description of the

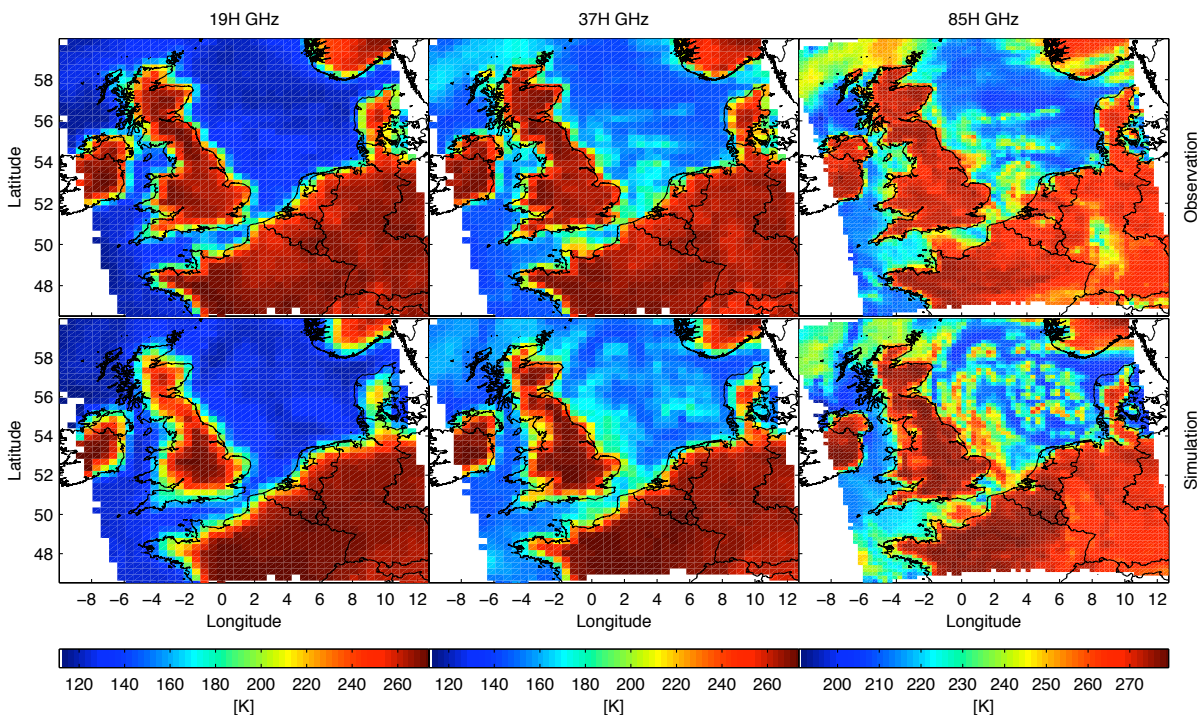


Figure 4.5: Comparison between SSM/I observations (top) and the Atmospheric radiative Transfer Model (ATM) (bottom) at window frequencies 19, 35, and 85 GHz for the Hoek case (see sec. 5.1).

frozen particles, their dielectric properties, and their PSD are not realistic. And third the approximations applied for the single-scattering calculations can not be applied to the present particles.

Most likely the error is connected to the non-sphericity of the particles and their dielectric properties that can not be accurately described within the models. Furthermore, the Méso-NH microphysical scheme produces more graupel in the expense of snow. Due to the shape of snow particles, that is more oblate than the more spherical-like graupel particles, an additional underestimation of scattering is implicated. More detailed investigations on that can be found in *Meirolid-Mautner et al. (2007)*. Further comparisons between simulations and observations are presented in chapter 7 where COSMO-DE and SynSatMic simulations are compared to AMSU-B for two specific cases.

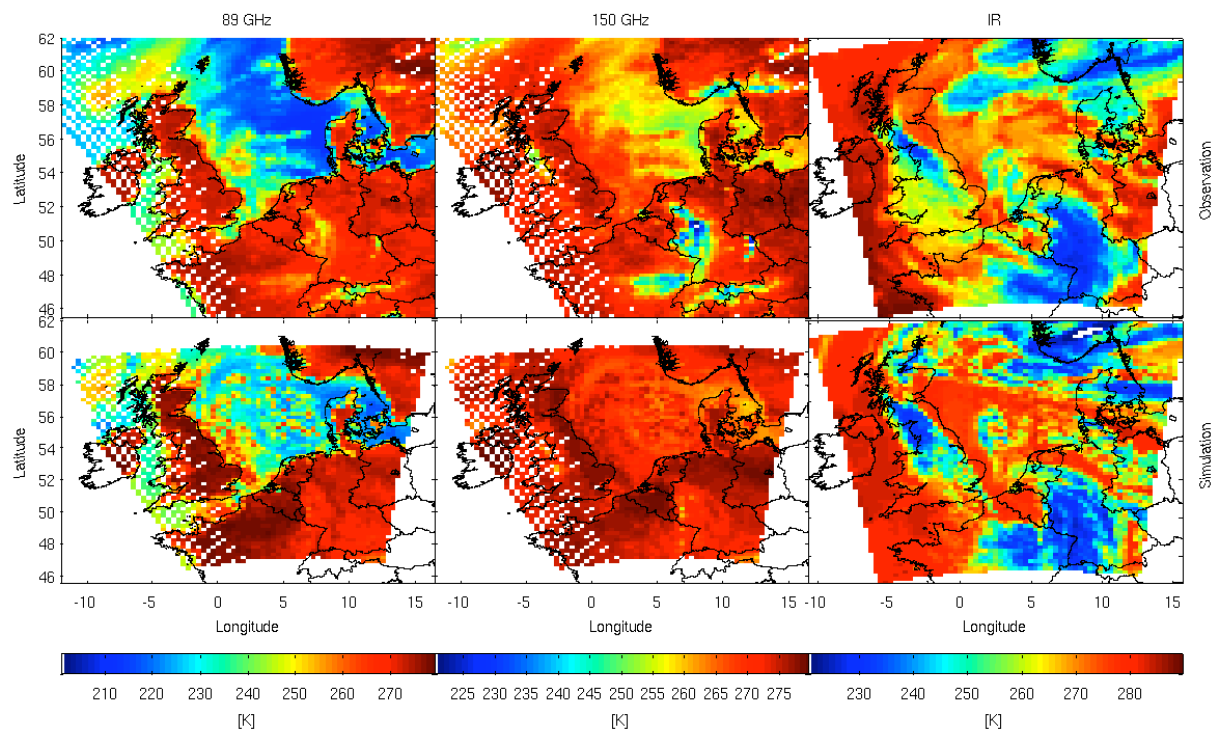


Figure 4.6: Comparison between AMSU-B and Meteosat observations (top) and the Atmospheric radiative Transfer Model (ATM) (bottom) at window frequencies 89 and 150 GHz, as well as the Meteosat infrared channel at  $11 \mu\text{m}$ .



# Chapter 5

## Data base for retrieval development

Satellite observations of the earth's atmosphere are in terms of brightness temperature. To infer hydrometeor quantities, retrieval algorithms need to be applied on a set of observed brightness temperatures. Such retrieval algorithms need to be developed on the basis of datasets consisting of brightness temperatures and corresponding hydrometeor contents and surface rain rates, respectively. The quality of the statistical dataset is essential: the variability described in the dataset should represent as correctly as possible the different regimes of precipitation in the region of interest. Unfortunately, when developing retrieval algorithms for hydrometeor observations in the mid-latitudes not many observed or even simulated datasets are available. For the tropical region, the GPROF (Goddard PROFiling) dataset (*Kummerow et al.*, 2001) focussing on retrieval development from both, SSM/I and TRMM observations, has been developed, with outputs from seven tropical precipitation cases. Such a database can not directly be used to develop algorithms for rainfall estimations outside the tropics (Note, however, that the latest version of the GPROF database contains also two mid-latitude simulations *Olson et al.*, 2006).

In order to analyze the potential of the millimeter- and submillimeter-wavelength region for hydrometeor observations from satellites in the mid-latitudes, a database needs to be build from scratch. The components used to setup the database have been described in the previous chapters. These are the CRM Méso-NH and the RT model MWMOD. In this chapter, the atmospheric cases, the frequency selection, and an investigation of the sensitivity of the simulated brightness temperatures is presented.

### 5.1 Simulated atmospheric cases

To cover different precipitation situations for the mid-latitudes in different seasons, a set of five different cases was selected (see Tab. 5.1) typical for this region. In order to take into account the microphysical changes occurring in the lifetime of precipitation events, two different time steps were chosen for each event. To allow a comparison of the model results, time steps with close-by satellite overpasses with microwave sensors on board have been chosen as model output times.

Name	Event	Date	Time for output
ALGER	Algiers flood	Nov. 10, 2001	<b>02</b> and 07 UTC
ELBE	Elbe flood	Aug. 12, 2002	<b>06</b> and 18 UTC
HOEK	Light precipitation at Hoek van Holland	Sep. 19, 2001	03 and <b>18 UTC</b>
RHINE	Light frontal precipitation over Rhineland	Feb. 10, 2000	09 and <b>18 UTC</b>
UKMIL	Millennium storm in South East England	Oct. 30, 2000	06 and <b>09 UTC</b>

Table 5.1: Overview of the different cases considered for the database of mid-latitude precipitation events. Output times written in bold letters have been used in Figs. 5.1 and 5.2 for the surface rain rate and hydrometeor statistics.

For the simulations, the CRM Méso-NH was set up for the corresponding region of interest and initialized with ECMWF analyses. A horizontal resolution of 10 km was chosen for all cases, because it is sufficient to resolve the typical scales that can be achieved by higher microwave frequencies from geostationary orbits. Furthermore, running the model in such a resolution allows to cover a sufficiently large horizontal area with about  $1600 \times 1600$  km. The vertical grid consists of 25 levels between the earth's surface and 20 km with grid spacing varying between 60 m (close to the ground) to 600 m (in the stratosphere).

For the database of atmospheric simulations, five cases typical for mid-latitude precipitation events were selected (see Tab. 5.1). They occurred in different seasons and are assumed to cover the variety of precipitation situations affecting Europe to a good degree. The selected situations include a frontal case with light precipitation over the Rhine area (RHINE, February 10, 2000), a long lasting precipitation event at Hoek van Holland (HOEK, September 19, 2001), a moderate rain case over the Elbe area (ELBE, August 12, 2002), an intense rain case over Algiers (ALGER, November 10, 2001), and the 'millennium storm' in England (UKMIL, October 30, 2000). All these cases concerned cloud systems organized at the mesoscale.

**Algiers flood** The Algiers flood case occurred on November 10, 2001 leading to the most devastating flood in this area with more than 700 casualties and catastrophic damage (e.g. *Argence et al.*, 2006; *Tripoli et al.*, 2005). The rainfall was caused by an intense mesoscale cyclone resulting from the interaction between an upper-level trough over Spain and lower-level warm air moving north off the Sahara. At 02 UTC, the heaviest rainfalls were located in several cells organized in a line along the North African coast (Fig. 5.1). Over Algiers, 262 mm of rainfall was measured during the entire storm episode, with more than 130 mm between 06 and 09 UTC. At the Dar-el-Bedia station, situated inland, only 15 km away from Algiers, only 41 mm was recorded (*Argence et al.*, 2006).

**Elbe flood** Convection embedded within synoptic-scale frontal precipitation resulted in the Elbe flood in August 2002. The synoptic situation was characterized by a deep cyclone moving from the Mediterranean Sea towards Poland (e.g. *Zängl*, 2004; *Ulbrich et al.*, 2003). On August 12, the cyclone was quasi-stationary over eastern Germany and the Czech

Republic. On the western side of the low, the partly occluded warm front coincided with the steepest pressure gradient area at 06 UTC (Fig. 5.1). This system brought large rainfall amounts: more than 300 mm fell in one day in parts of Ore Mountains, a mountain range at the German-Czech frontier. The extreme precipitation was followed by a very quick rise of the levels of the Elbe tributaries, leading to a 100-year-flood of the Elbe river with the largest recorded flood related damage in Europe.

**Hoek van Holland** Light precipitation occurred on September 19, 2001 at Hoek van Holland. This was a long lasting precipitation event produced by a quasi-stationary low pressure system over the Netherlands (Fig. 5.1). A maximum of 100 mm accumulated rainfall was recorded over the whole event at Hoek van Holland, with relatively small rain rates of a few mm/h.

**Rhineland** For the Rhine case, light precipitation was related to a cold front passing western Germany on February 10, 2000. At 18 UTC, the cold front was associated with a broad pattern of light surface rainfall of a few mm/h (Fig. 5.1). The 0°C height dropped from 2 to 0.5 km. By that precipitation could reach the ground as snow, which is of particular interest for precipitation phase retrievals.

**Millennium storm** The 'millennium storm' corresponded to an exceptionally intense low over the English Midlands and its associated fronts. On October 30, 2000, the low had deepened from 994 to 958 hPa in 12 hours (*Browning et al.*, 2001). The steep pressure gradient resulted in strong winds and widespread gusts between 30 and 40 m/s. Heavy rain fell all night, leading to 24 hour totals between 25 and 50 mm, with 75 mm and more in some areas. Local floods occurred and caused major disruption of commuter traffic during the morning rush hour of October 30. The rainfall pattern at 09 UTC was typical for an extratropical cyclone (Fig. 5.1). The more intense areas were located in the occluded warm and trailing cold fronts of the low over the North Sea, while weak showers were scattered in the cold sector over the Atlantic Ocean.

A more detailed description of the simulated cases and the setup of Méso-NH for the single model runs can be found in *Chaboureau et al.* (2007) and *Crewell et al.* (2005).

## 5.2 Analysis of the hydrometeor contents

As indicated in the description of the events in the previous section a reasonable number of heterogeneous precipitation types is covered by this set of selected cases. Tab. 5.2 shows statistics of hydrometeor contents for the different cases and time steps. It makes sense to take different development stages of the precipitation system into account, since significant differences in maximum and minimum rain rates as well as in the partitioning of the different hydrometeor contents occur at different time steps (see Tab. 5.2).

The distributions of the vertically-integrated hydrometeor contents and the surface precipitation rates are examined in Fig. 5.2. The outputs are shown only at times with AMSU-

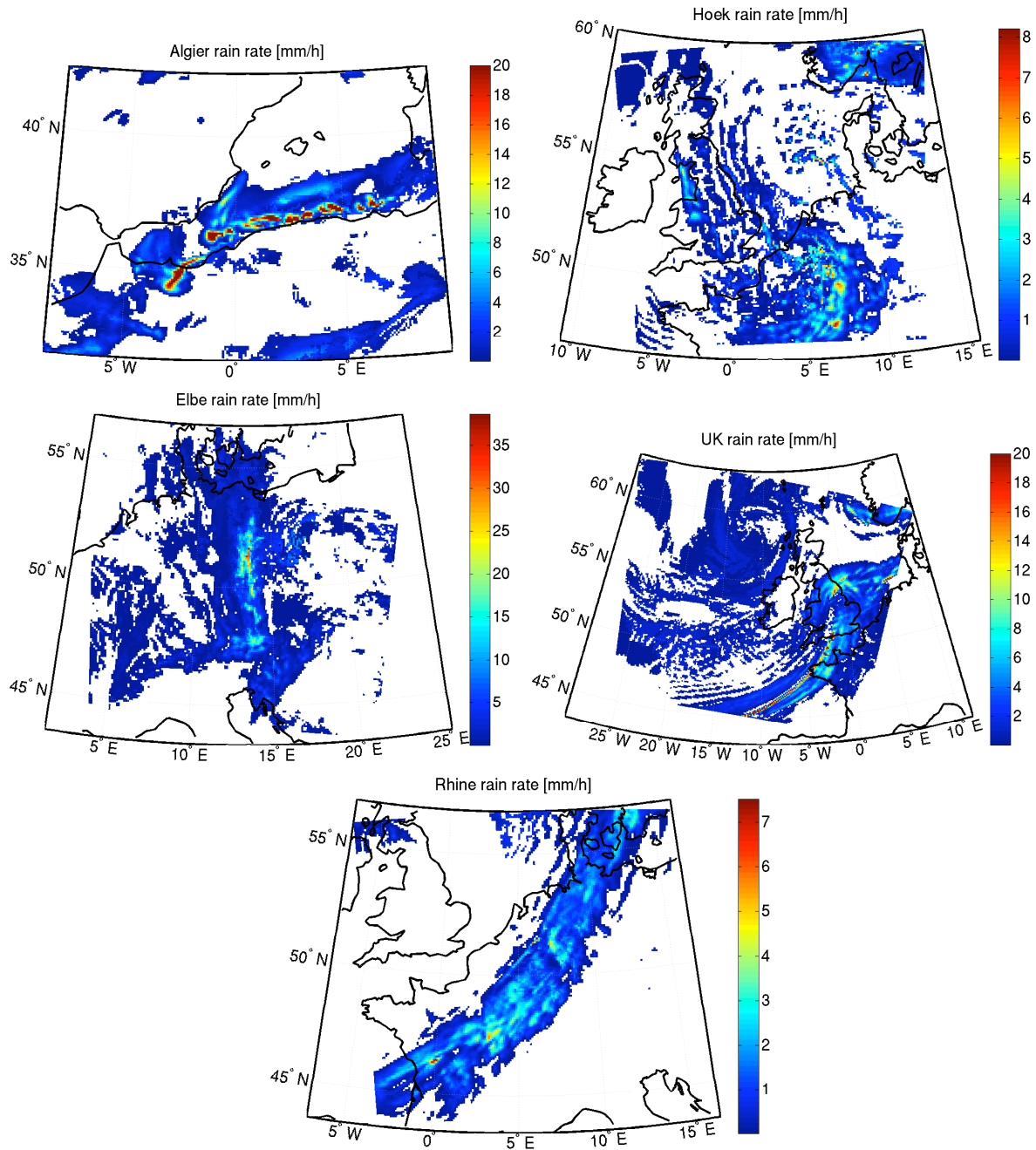


Figure 5.1: Overview of the different precipitation cases (bold letters in Tab. 5.1) in terms of surface rain rates (in mm/h) and the respective domains considered in this study. In the UKMIL and ALGER cases, the surface rain rates are shown with a cut off above 20 mm/h for presentation reasons. For statistics of the events see Tab. 5.2.

Case	$R_{max}$ mmh <sup>-1</sup>	$\langle R \rangle$ mmh <sup>-1</sup>	$f_{rain}$ %	$G_{max}$ kgm <sup>-2</sup>	$\langle G \rangle$ kgm <sup>-2</sup>	$f_{grau}$ %	$S_{max}$ kgm <sup>-2</sup>	$\langle S \rangle$ kgm <sup>-2</sup>	$f_{snow}$ %
<b>ALGER02</b>	130.8	0.39	23	24.0	0.14	51	2.5	0.18	61
ALGER07	107.2	0.44	29	18.7	0.14	67	2.5	0.22	73
<b>ELBE06</b>	35.7	0.41	49	8.0	0.06	44	2.1	0.15	56
ELBE18	13.1	0.23	52	4.0	0.02	42	2.0	0.07	58
HOEK03	9.5	0.15	37	2.6	0.01	36	1.7	0.05	44
<b>HOEK18</b>	7.7	0.22	50	2.0	0.02	45	1.7	0.09	67
RHINE09	16.1	0.26	42	3.6	0.04	49	1.9	0.13	74
<b>RHINE18</b>	7.3	0.28	37	1.3	0.03	59	1.6	0.16	81
UKMIL06	212.5	0.5	72	3.2	0.08	69	2.1	0.19	83
<b>UKMIL09</b>	147.2	0.48	75	5.2	0.07	72	2.1	0.17	83

Table 5.2: Hydrometeor statistics for all cases: maximum precipitation rate ( $i_{max}$ ), mean precipitation rate ( $\langle i \rangle$ ) only for pixels with precipitation and percentage of profiles with precipitation ( $f_i$  in %) of type  $i$ , where  $i$  is rain  $\langle R \rangle$ , graupel  $\langle G \rangle$ , and snow  $\langle S \rangle$ . Output times written in bold letters have been used in Figs. 5.1 and 5.2.

B overpasses. The distribution of the surface precipitation rate shows a large variability that includes light (RHINE and HOEK), moderate (ELBE), and strong (ALGER, UKMIL) precipitation cases. This classification is well documented in Tab. 5.2: the largest surface rain rates are simulated for ALGER and UKMIL. For the frozen hydrometeor contents, the same classification can be adducted. In contrast, the distributions of the rain content separate into two groups only (RHINE and HOEK versus ELBE, UKMIL, and ALGER) and the distribution of the liquid water content is more homogeneous (see Fig. 5.2). This can be explained by the microphysics and the way hydrometeors are formed. An excess of cloud ice was converted into snow that grew by aggregation and riming and was then transformed into graupel particles. Finally, graupel particles and rain drops contribute most to the surface precipitation rate.

Since the surface rain rate is the product of a number of complex processes, the relation between the rain rate and the hydrometeors aloft, which determine the microwave signal, is not a straightforward one. The mean vertical profiles for all cases at satellite overpass times (Fig. 5.3) show that the relation strongly depends on the 0°C isotherm: the liquid layers are confined in the lower layers of the atmosphere with the frozen particles aloft. As the simulation domains cover a few thousands of kilometers, the altitude of the 0°C isotherm changes within the simulation domain by a few hundred meters as indicated by the range drawn for each mean profile (Fig. 5.3). Non-precipitating ice content is found only above the 0°C isotherm maximum height as the primary ice crystals are immediately melted into cloud droplets at temperatures warmer than 0°C. In contrast, cloud water can exist well above the freezing level in the form of supercooled droplets, which are available for ice riming. Precipitating ice can also be found below the 0°C isotherm in warm layers where the snowflakes are progressively converted into graupel particles which melt as they

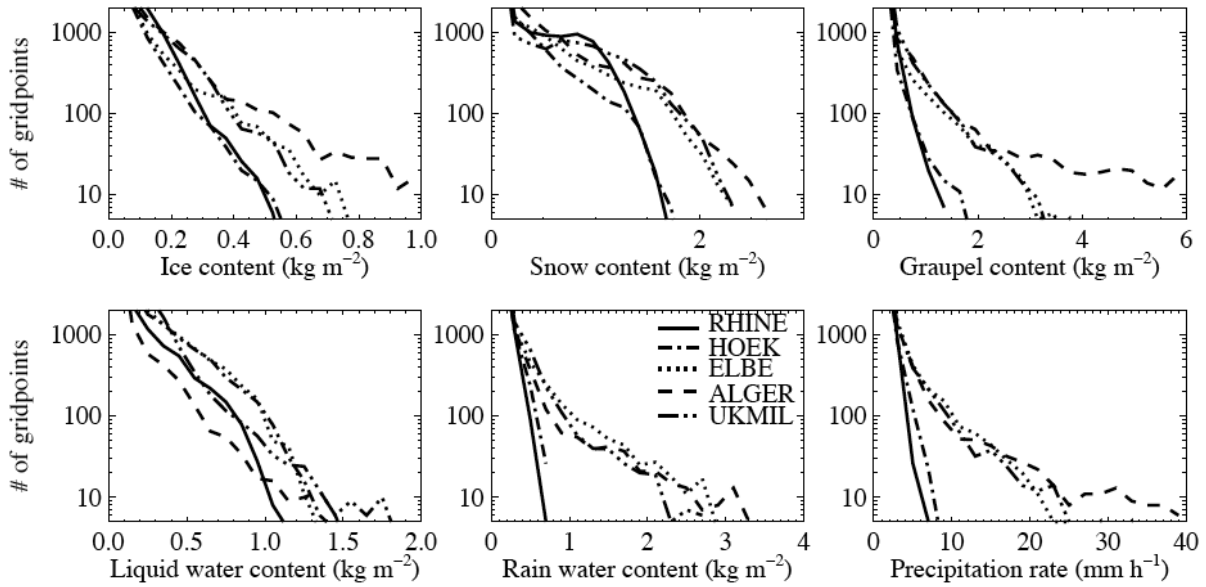


Figure 5.2: Distributions of vertically integrated hydrometeor contents ( $\text{kgm}^{-2}$ ) and precipitation rate ( $\text{mmh}^{-1}$ ) for the different precipitation cases (bold letters in Tab. 5.1). The bin widths of the ice, snow, graupel, cloud liquid water, and rain water contents, and the precipitation rate are 0.05, 0.15, 0.3, 0.1, and  $0.2\text{kgm}^{-2}$  and  $2\text{mmh}^{-1}$ , respectively. The very high contents mentioned in Tab. 5.2 were single point simulations and have been omitted in this distributions.

fall. Rain is formed by autoconversion of cloud droplets or results from the melting of graupel. As a consequence, the rain layer is always below the  $0^\circ\text{C}$  isotherm. This makes clear that the precipitation is produced by the cold rain process in the solid form as snow and graupel which later on melts to rain.

The averaged vertical profiles also varied from case to case (see Fig. 5.3). This was mostly due to the seasonal variation of the air temperature. The RHINE case in February included grid points where graupel and snow particles could reach the ground (Note that the statistics shown in Tab. 5.2 consider the whole column for snow and graupel and not only surface contributions). The two autumn cases (UKMIL and ALGER) presented similar shapes with snow and graupel layers above the ground. The HOEK case in September showed precipitating frozen hydrometeors in higher layers above 1.5 km. Finally, the ELBE case in August was the warmest case with a deep cloud water layer extending up to 4 km and frozen water content present above 2.5 km.

The separation of the different phases raises the hope that the microwave signal, which will be mainly determined by the upper atmospheric ice particles, will have an accurate relation to the surface rain rate. Such a relationship was investigated by looking at the correlation between the surface precipitation rate and the different integrated hydrometeor contents at two output times (Fig. 5.4). As expected, the highest correlation exists for the

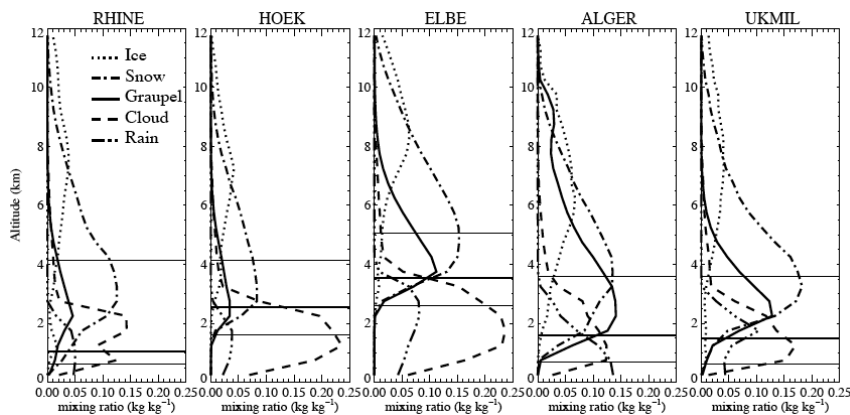


Figure 5.3: Mean vertical distributions of the different hydrometeor categories in the troposphere. The contents are shown as mixing ratios [kg/kg]. Averages are calculated only from hydrometeor contents that are not zero. The horizontal thick (thin) line represents the mean (maximum/minimum) altitude of the 0°C isotherm.

vertically-integrated rain (up to 0.9). Linear correlation coefficients above 0.7 can also be found for the integrated graupel content for three cases. Lower values are obtained for vertically integrated snow, which are more strongly case-dependent. The high correlation between the integrated frozen hydrometeor contents (snow, graupel, and cloud ice) emphasizes the cold rain process. The correlation relative to the integrated non-precipitating water (ice and cloud water) contents is the lowest (around 0.5). It should also be pointed out that the correlation values for a particular case and a particular water content can vary considerably with time. For example, the correlation coefficients for the integrated graupel content for the ELBE case are 0.76 and 0.39 at 06 and 18 UTC, respectively. Therefore, the rain retrieval from indirect measurements of cloud and precipitation contents, using regression-based methods is a highly challenging task.

The five mid-latitude situations compiled in this database differ significantly from the tropical cases simulated for the GPROF database (*Kummerow et al., 2001; Olson et al., 2006*). The freezing level of the mean vertical profiles in these mid-latitude cases is located between 1 and 3 km altitude, whereas in the tropics, its usual height is about 4.5 km. This means that frozen hydrometeors exist throughout the troposphere in the mid-latitude cases. Furthermore, the GPROF tropical cases are deep convective situations, while this mid-latitude cases include as well stratiform precipitation events. In convective situations, the development of large graupel particles and rain drops is more favorable due to strong updraft winds. In contrast, stratiform cases with weak vertical velocities favor small-sized hydrometeors.

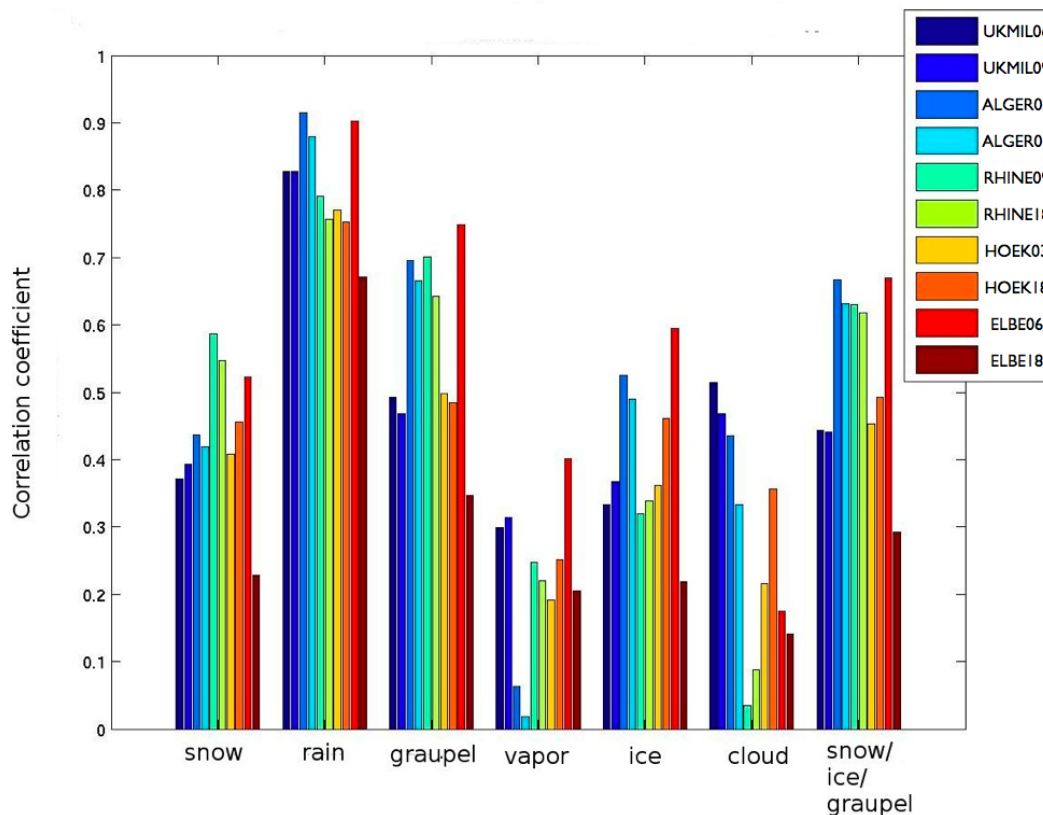


Figure 5.4: Correlation between the different integrated hydrometeor contents and the surface rain rate for all cases and both time steps. The rightmost columns show the correlation between the frozen hydrometeor contents and the surface rain rate.

### 5.3 Frequency selection

The question whether window frequencies or frequencies in the various absorption bands are best suited for precipitation retrieval is still under discussion. In window channels, the information comes from the scattering at the hydrometeors and provides only integrated quantities. The use of absorption channels provides the possibility of vertically resolving the atmospheric hydrometeor profile to some extent. By applying the method of differential absorption of frequencies in the oxygen line complex between 50 and 60 GHz and of that one at 118 GHz (*Bauer et al., 2005*), promising results for precipitation retrieval were obtained. Channels around 50, 118, and 424 GHz in the oxygen lines give access to the atmospheric temperature profile and were proposed by *Klein and Gasiewski (2000)* and by *Prigent et al. (2005)*. Water vapor profile information can be retrieved from channels around the 183, 325, and 380 GHz water vapor lines. In addition to their water vapor and temperature profiling capabilities, these sounding channels are expected to constrain the hydrometeor profiles (*Bauer and Mugnai, 2003*).

Satellite projects in the millimeter- and submillimeter-wavelengths, such as GEM and

Frequencies in GHz	Characteristics
50.3,52.8,53.6, 54.5,54.94,55.5	O <sub>2</sub> complex between 50 and 60 GHz
110.65,115.25,116.65, 117.25,117.65,118.0	O <sub>2</sub> line at 118 GHz
89.0,150.0,176.31, 340.0,398.2,428.76	window frequencies

Table 5.3: List of frequencies considered for the database between 50 and 428.76 GHz relevant for planned satellite missions.

GOMAS on geostationary orbits or Cloud Ice Water Submillimeter Imaging Radiometer (CIWSIR) on a polar orbit (*Bühler et al.*, 2005b), propose frequency channels that have similarities but are not identical, mainly because their objectives are not exactly the same: the first two (GEM and GOMAS) originally focus on water vapor and temperature profiling and more recently on precipitation, while the last one (CIWSIR) focusses on cirrus characterization.

The selection of the frequency bands for the database is based on the ones that are currently investigated for possible use in future satellite campaigns, i.e. on those relevant to the European contribution to the Global Precipitation Mission (EGPM), and on those in heritage of former successful satellite missions like the Advanced Microwave Sounding Unit (AMSU).

The 18 selected frequencies in the oxygen absorption complex between 50 and 60 GHz and at 118 GHz and the selected window channels in the range between 89 and 428.76 GHz are compiled in Tab. 5.3 and Fig. 5.5. Above 200 GHz, only three window frequencies are included as sounding channels since these high frequencies are not likely to be flown on satellite in the near future.

## 5.4 Database

The database, which was developed by combining CRM and RT model output as described in the previous chapters, consists of simulated brightness temperatures for five mid-latitude precipitation cases at two time steps of the cloud model runs. The brightness temperatures were simulated at 18 millimeter- and submillimeter-wavelength frequencies and for nine observation angles. One dataset of the database is build by the brightness temperatures at one frequency (vertical and horizontal polarization) and one angle together with the total column contents of the five hydrometeor categories (cloud water, cloud ice, rain, graupel, and snow) of the vertical profile used in the RT and the corresponding surface rain rate (graupel and snow are taken into account by the liquid equivalent mass). Since, on average, 60% of the 256000 profiles contain hydrometeors, the database consists of more than  $4 \cdot 10^7$  datasets.

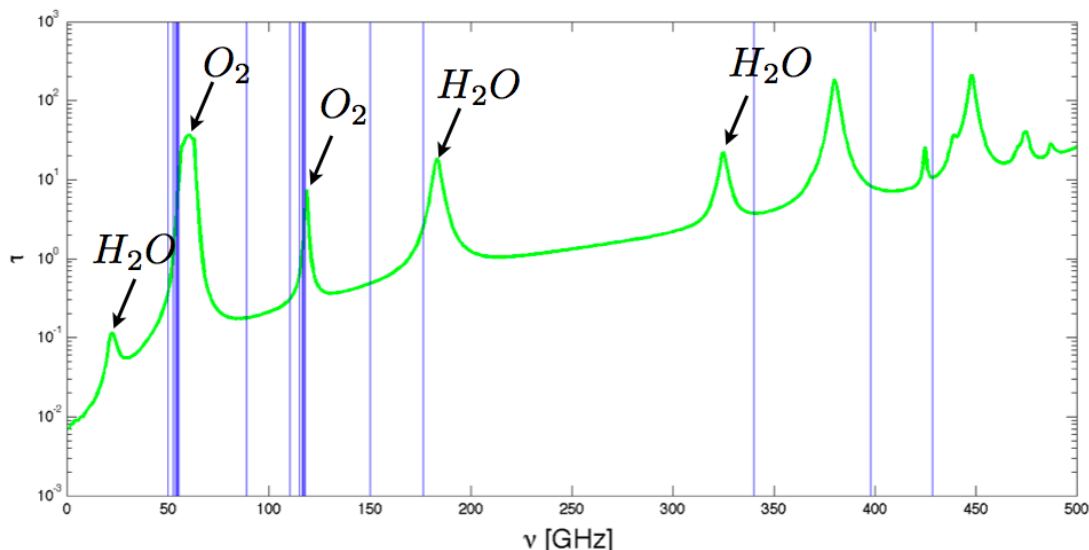


Figure 5.5: Absorption by water vapor and oxygen in terms of optical thickness. Blue lines show the frequencies between 50 and 428.76 GHz selected for the radiative transfer simulations.

## 5.5 Analysis of simulated brightness temperatures

Fig. 5.6 shows the simulated brightness temperature maps for the Hoek van Holland case at 18 UTC for an observation angle of  $52^\circ$ . The different horizontal distributions of the brightness temperatures give an idea which atmospheric properties might be retrieved. The highest frequencies of the two oxygen absorption bands (55.5 and 118 GHz) are highly opaque and only provide information on the upper tropospheric temperature. With decreasing frequency the radiation stems from lower altitudes. Consequently, the lowest channels (50.3 and 110.65 GHz) are already located in window regions and show the surface contribution with strong spatial contrasts due to strong differences in the emissivity  $\epsilon$  between land ( $\epsilon \approx 0.9$ ) and ocean ( $\epsilon \approx 0.5$ ). With increasing frequency, emission and scattering by hydrometeors evolve differently. The increase of extinction due to small particles, like cloud droplets, is approximately twice as strong at frequencies in the 118 GHz oxygen complex than at the corresponding (meaning similar clear air weighting function) frequencies in the 60 GHz complex (*Gasiowski et al., 1990*). For this reason, these channels, which are usually used for temperature sounding, were proposed by *Bauer and Mugnai (2003)* for remote sensing of precipitation.

At higher frequency channels, e.g. the 176.31 GHz (wing of  $H_2O$ -line) and above, the atmospheric absorption is already so strong, that differences between land and ocean disappear (see Fig. 5.6) and that the brightness temperature structures are closely related to the water vapor field (not shown). Due to high scattering at frozen hydrometeors, the ice cloud band over western Germany can be detected well by strongly reduced brightness temperatures.

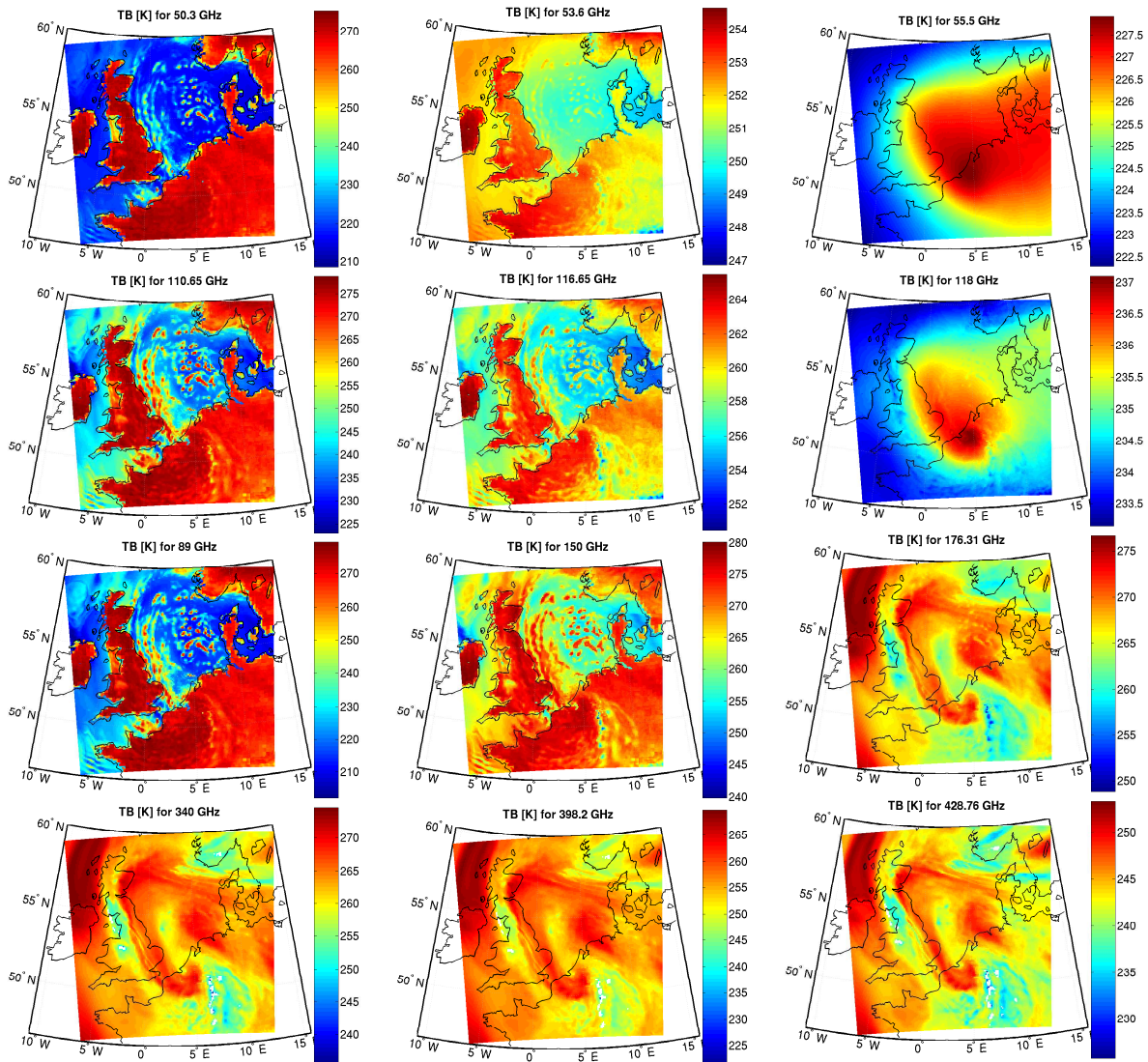


Figure 5.6: Horizontal distribution of the simulated brightness temperatures for selected frequencies for the Hoek van Holland case on September 11, 2001 at 18 UTC. The upper row shows simulations for frequencies in the oxygen complex between 50 and 60 GHz, the second row in the oxygen band at 118 GHz, the third row at the window frequencies 89, 150, and 176.31 GHz, and the bottom row at the higher window frequencies 340, 398.2, and 428.76 GHz on the wing of the 424.76 GHz oxygen line.

*Skofronick-Jackson et al.* (2004) showed that there is a high surface contribution to the brightness temperature for the AMSU-B window channels at 89 and 150 GHz. This contribution can be half of the observed signal at 89 GHz for profiles with low frozen hydrometeor contents over land. This effect decreases with increasing hydrometeor contents. The strong contribution of the land surfaces to the brightness temperature can be seen in the brightness temperature maps (Fig. 5.6), which reveal a strong difference of land and ocean pixels at window frequencies and at the channels of the outer wing of the absorption lines. Therefore, the correlations of all channels to the integrated hydrometeor content for all, ocean, and land, pixels are shown in Fig. 5.7. A separation into land and ocean pixels reveals that for frequencies of 176.31 GHz and above, no strong differences between land and ocean are obvious, but that for lower frequencies different mechanisms lead to different correlations. In the most transparent channels, e.g. 50.3 and 89 GHz, the correlation over ocean is positive for all hydrometeor types, showing the emission effect over the radiatively cold sea (emissivity  $\approx 0.5$ ). Over land, with its emissivity of about 0.9, low level water clouds are still radiatively warmer than the surface, leading to a positive correlation, while frozen hydrometeors, even at low frequencies, already give a negative correlation because of the scattering effect. Low correlation values ( $< 0.2$ ) at opaque channels (54.5-55.5 GHz, 117.25-118.0 GHz) should be carefully interpreted, because the brightness temperature variation is very small ( $< 2$  K) and depends mainly on the upper atmospheric pressure distribution, i.e. the tropopause height.

The correlation between the surface rain rate and the brightness temperatures is only slightly lower than the one for the rain water path and the brightness temperatures. The investigation of the correlation between the integrated rain water to the surface rain rate in section 5.2, showed values up to 0.9 for some simulated cases, but in each case at least more than 0.68. Strongly case dependent correlations in the range from 0.3 to 0.7 exist as well between the integrated frozen hydrometeor contents and the surface rain rate. Such a correlation indicates that the surface rain rate can be retrieved from observations in frequencies sensitive to scattering at frozen hydrometeors. This sensitivity can be seen in Fig. 5.7, where the correlations between brightness temperature and frozen hydrometeors has high negative values up to -0.7 for snow and ice clouds and -0.5 for graupel. As a rule of thumb, the correlation of brightness temperature with surface rain rate or rain water path is about half of that to snow or ice.

It can clearly be seen from Fig. 5.7, that the combination of land and ocean pixels reduces the correlation, as different physical processes are mixed. Therefore it seems to be sensible to separate also the different regimes, when retrieval algorithms are developed, as the surface flag (land/ocean) is well known.

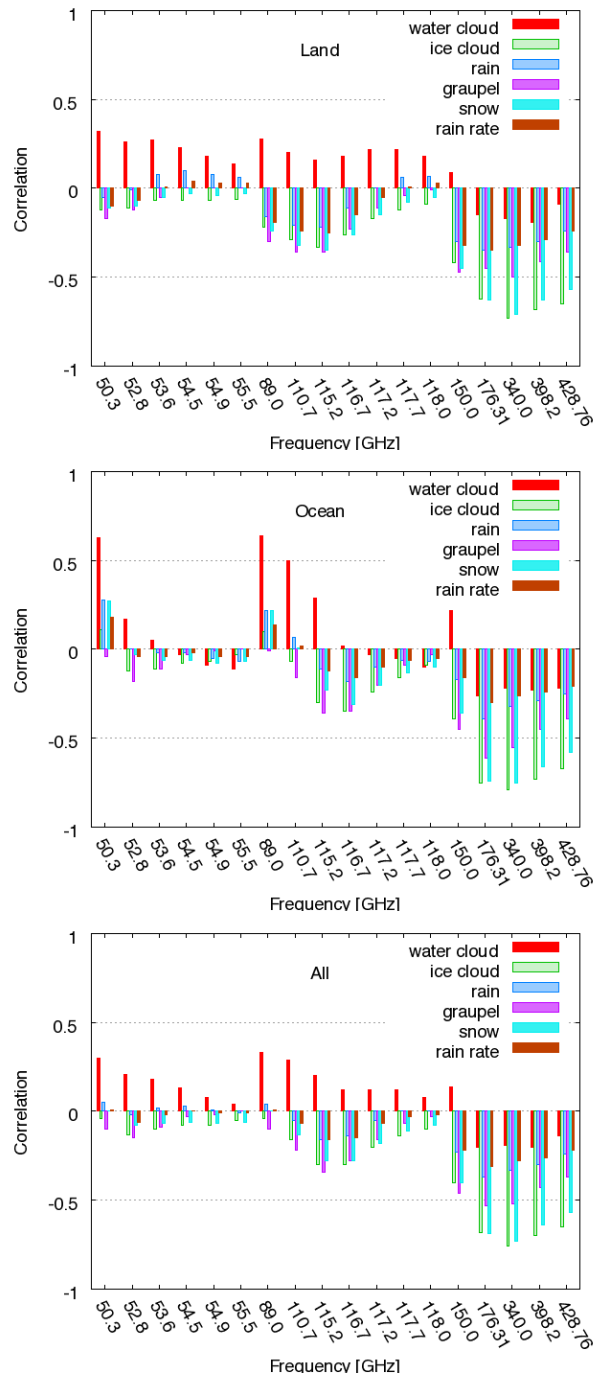


Figure 5.7: Correlation between the simulated brightness temperatures at different frequencies and the integrated hydrometeor contents, as well as the surface rain rate. Land pixels (top), ocean pixels (middle), and all pixels (land and ocean; bottom).



# Chapter 6

## Retrieval approaches

The selection of the precipitation cases for a specific region and the choice of the simulated frequencies determine the information content of the corresponding database. Retrieval algorithms based on that database, should therefore be able to retrieve this information once they are applied to measurements. Following the theoretical considerations of the chapters 2 and 3, it can be assumed that the choice of frequencies in the higher microwave range should provide a high potential to reveal information especially for frozen hydrometeors.

The largest problem in the retrieval of precipitation rates and hydrometeor contents from observed microwave brightness temperature is that it is ill-determined. The brightness temperature is related to the vertical profiles of temperature, humidity, and hydrometeors (cloud water and ice, rain, graupel, and snow). In addition, depending on the frequency, the PSD, the shape, and the orientation of the hydrometeors can also influence the brightness temperature. Therefore, it is clear that the number of free parameters is much larger than the number of frequencies measured and a direct inversion is not possible. It should be noted that just increasing the number of frequencies would not result in a much better posed problem as brightness temperatures are often strongly correlated.

In the first section of this chapter, an overview of different retrieval algorithms is presented. After that, very simple statistical retrieval approaches are developed and applied to the database to investigate the information content and the potential of the frequency selection with respect to the different hydrometeor types and the surface rain rate. Thereby self-tests of the database and investigations with reduced number of frequencies are performed. By reducing the cases within the database, their coverage is evaluated with respect to variability in precipitation events.

### 6.1 Retrieval algorithms

Typically, retrieval algorithms are distinguished between statistical and physical ones. Pure statistical algorithms are based on a set of concurrent brightness temperature and rain rate or hydrometeor content values, which are related by some kind of function. The classical physical algorithm finds a solution for the atmospheric state (including rain rate

or hydrometeor content) such that the measured brightness temperatures are very close to the ones simulated from the derived profile of the atmospheric state. Since a large number of atmospheric states can satisfy each combination of brightness temperatures, constraints have to be chosen which will reduce the degrees of freedom. Therefore, many retrieval algorithms are described as physical but almost always depend on some sort of statistical assumptions about the atmospheric state.

In general, statistical algorithms make use of a database of possible atmospheric situations together with simulated brightness temperatures. These databases were initially built from cloud model simulation outputs. Although it is certainly not possible to simulate the multitude of situations occurring in reality, a limited number of well-documented situations combined in a database could provide at least solutions that are physically meaningful. Based on such a database, algorithms need to be developed that can be applied to observations.

The simplest approach to use the information contained in such a database is by developing regression algorithms. To account for the non-linearity of the problem, the regression is often performed by using the logarithm or higher orders of the brightness temperatures or by using artificial neuronal networks.

Another way of using the information contained in such a database is the Bayesian framework. Thereby, the best estimate for the atmospheric state given the set of observed brightness temperatures is determined by finding the minimum variance solution. For that purpose, each brightness temperature (observed and simulated) is weighted by the inverse of their variance (uncertainty). In the optimal estimation formulation it is assumed that these errors are Gaussian distributed. While the error of the observations can relatively easily be estimated from the radiometer performance, the error of the simulations is more difficult as it contains uncertainties of the cloud and radiative transfer model. Thus, the simplest approach is using a fixed value for the uncertainty as for example done by *Kummerow et al.* (2001) using 8 K for each frequency channel. Their approach also assumes that the distribution of atmospheric states in the database is the same as in reality and thus covers all precipitation types and development stages.

Physically based algorithms include a physical description of the interaction of electromagnetic waves with the atmospheric components. This technique requires the vertical distribution of hydrometeors and other parameters, that determine the signal received at the satellite. The first of these algorithms are based on an iterative adjustment of detailed cloud model profiles which are fed into a RT model to reproduce the observations. Examples are the classical algorithms by *Kummerow et al.* (1989), *Kummerow and Giglio* (1994), *Smith et al.* (1992), or *Mugnai et al.* (1993).

*Bauer et al.* (2001) used one database to develop different algorithms (multiple regressions, neural networks, and Bayesian estimators). They found that all algorithms perform relatively similar (with the exception of weakly non-linear algorithms). Therefore, in the following sections, multiple regression algorithms as the simplest approach, will be developed to investigate the potential of the millimeter- and submillimeter-wave region for hydrometeor and precipitation observations.

## 6.2 Multiple regression

For each case and for the different surfaces (land/ocean), multiple regression algorithms of the form

$$q = a + \sum_{i=1}^{n_f} b_i \cdot T_{b_i} + \sum_{i=1}^{n_f} c_i \cdot T_{b_i}^2 \quad (6.1)$$

were developed for the hydrometeor and the surface rain rate retrievals. Here,  $q$  is the retrieved quantity,  $a$ ,  $b_i$ , and  $c_i$  the coefficients of the regression, and  $T_{b_i}$  the simulated brightness temperatures at  $n_f$  frequencies. For the brightness temperature the mean between horizontal and vertical polarization has been used. By including quadratic terms, non-linearities were taken into account. In the retrieval development, only hydrometeor contents greater than a threshold value of  $0.1 \text{ kgm}^{-2}$  were considered. The performance is described by the relative error  $\delta x$ , defined as

$$\delta x = \frac{\sqrt{\frac{\sum_n (x_j - y_j)^2}{n}}}{\bar{y}} \quad (6.2)$$

the sample standard deviation divided by the mean of the inspected quantity. Here,  $x_j$  is the value of the retrieved quantity at pixel  $j$ ,  $y_j$  the output of the cloud model for the quantity and pixel,  $\bar{y}$  the mean, and  $n$  the number of all pixels containing the concerned quantity above the threshold value. The results for the relative errors are compiled in Fig. 6.1. It clearly shows that the performance for ocean and land pixels is different from case to case. Furthermore, it shows that the combination of both types of pixels gives worse results especially in cases with high retrieval potential, e.g. the HOEK case. This confirms the importance of separating land and ocean pixels and developing separate algorithms for both conditions. Also, the combination of different cases and time steps leads in general to a reduced performance. For instance in the HOEK03 case the rain water path for ocean pixels can be retrieved with a relative error of 6.8%, but can increase up to 34.3% for the ELBE06 case. The combination of both surface types and all cases leads to a relative error of 65%. Generally, the graupel water path can be retrieved with very low relative errors less than 25% for almost all cases and conditions, as long as separated cases are considered. This is surprising since the very high graupel contents in the Algiers flood case (Tab. 5.2) caused high errors in the retrieval, when experimenting with linear regression algorithms. The snow water path is better detected over land for the more stratiform cases (HOEK, RHINE, and UKMIL). For the strong convective ALGER07 case, the results for the ocean pixels are better. The low relative errors for the frozen hydrometeor types indicate a high potential to sense more information about microphysics than just the surface rain rate as an end product. When combining both surface types, the retrieval performance can have very large relative errors over land for the rain water path and the surface rain rate for convective cases (ALGER and UKMIL).

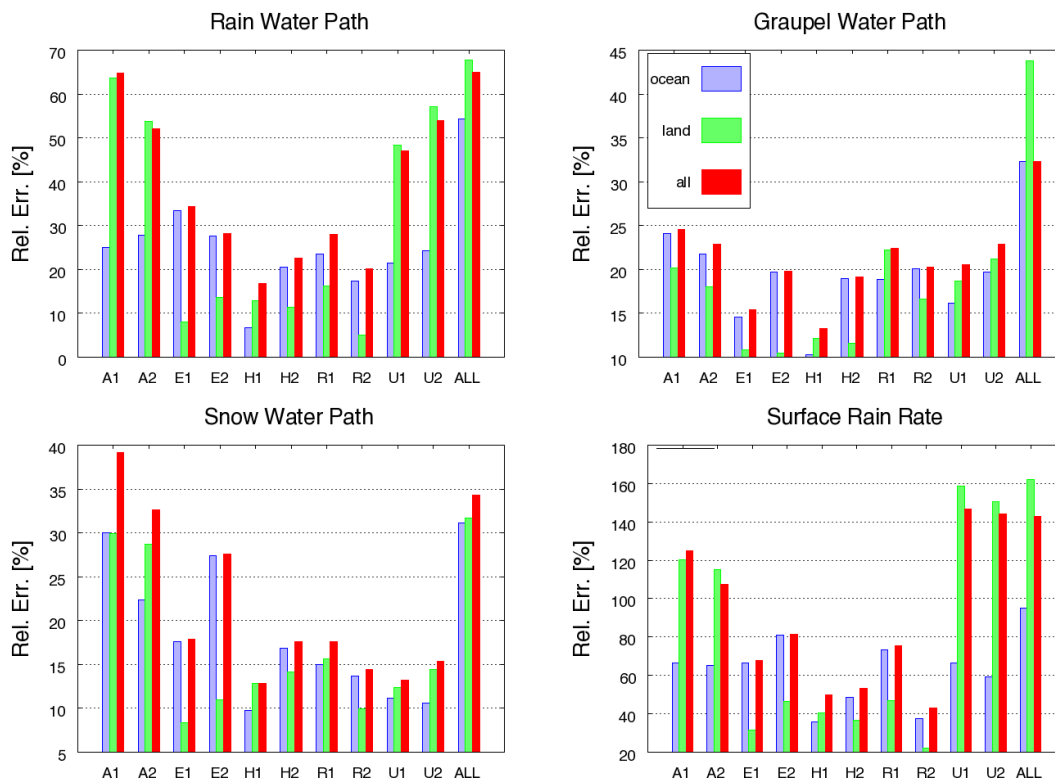


Figure 6.1: Relative errors of the retrieval are shown for rain, snow, and graupel water path as well as for the surface rain rate. The relative errors are separated into land, ocean, and all pixels for each single case and time step. Here and in the following figures, the denotation for the cases has been changed: A1 corresponds to ALGER02, A2 to ALGER07, E1 to ELB06, etc.. The columns indicated by *All* represent the retrieval performance for all cases and time steps merged together.

To test the robustness of the retrieval results on perturbations of the brightness temperatures at all frequencies, common to realistic measurements, random noise with increasing maximum amplitudes up to 2 K was added to the brightness temperature dataset. When increasing the noise, the relative errors only changed by about 2 percentage points, which indicates a high robustness with respect to such disturbances.

### 6.3 Frequencies for GEO

Since for a geostationary orbit only frequencies higher than 150 GHz result in spatial resolutions sufficient for numerical weather forecast models and hydrological applications for realistic antenna sizes, retrieval algorithms based on the brightness temperatures simulated at frequencies of 150 GHz and above were developed. By comparing the relative errors of the retrievals based on all frequencies to the one based only on the higher ones (Fig. 6.2), the loss in retrieval accuracy by excluding the information contained in the lower frequen-

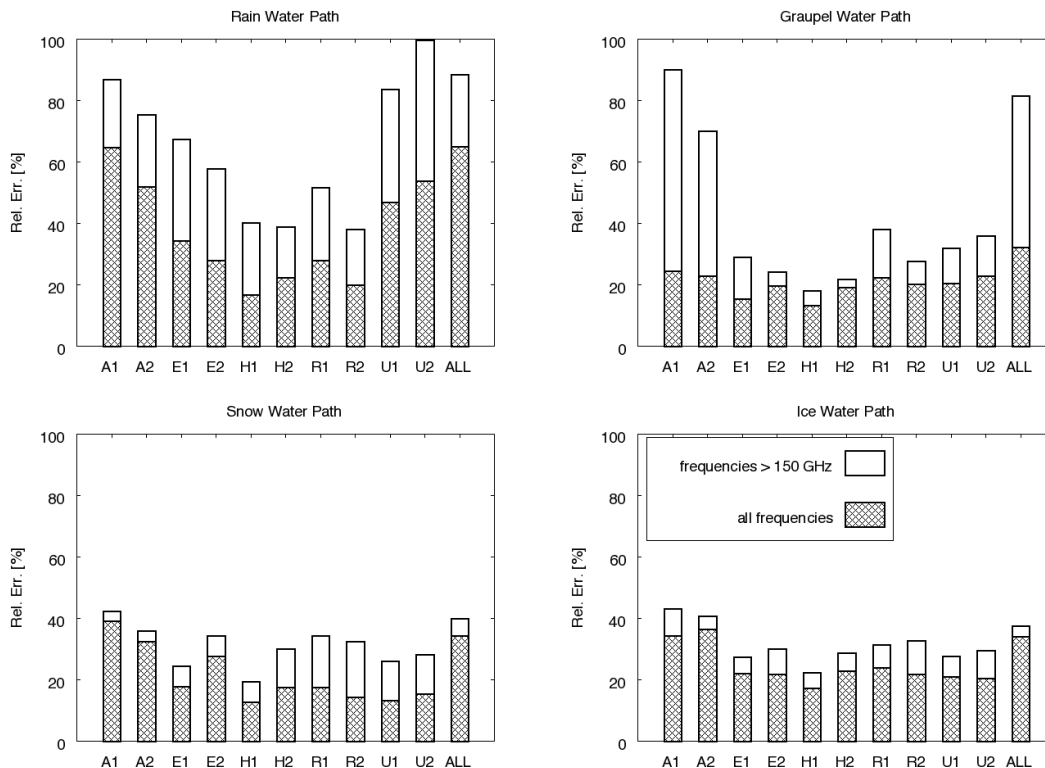


Figure 6.2: Comparison of the performance in terms of relative errors between hydrometeor retrievals including all frequencies and the one based on algorithms including only frequencies at 150 GHz and above for land and ocean surface types together. For the denotation of the cases see Fig. 6.1.

cies can be clearly seen. As expected from the theoretical considerations, the integrated contents of the frozen hydrometeor types can be retrieved with only a small loss of accuracy by only using the high frequencies. Thereby for single cases, the loss in accuracy is below 10 percentage points in the relative error. For the snow water path and the ice water path, even with all cases merged together, the loss of accuracy is very small. Two exceptions can be found for the accuracy of the frozen hydrometeor retrieval based on higher frequencies. The first exception are the very high graupel water paths produced in the strong convective Algiers flood case. The second are the snow water paths in the RHINE and UKMIL cases. For these cases, the  $0^{\circ}\text{C}$  isotherm is at very low altitudes which results in snow contents in the lowest layers. The sensitivity of the higher frequencies to hydrometeors in the lower layers is not very high, due to water vapor absorption. Therefore, to retrieve snow contents in atmospheric layers close to the ground lower frequencies are important in the mid-latitudes. Nevertheless, even with frequencies above 150 GHz the relative errors for these two cases are below 40%. For the rain water path, the consideration of the lower frequencies is important. Omitting the lower frequencies can result in a doubling of the relative errors.

Quantity	rain water path					
Pixels	all		ocean		land	
Frequencies	110.65,53.60, 52.80,89.0, 118.0	all	110.65,53.60, 52.80,117.65, 89.0	all	115.25,50.30, 176.31,118.0, 150.0	all
Correlation	0.73	0.80	0.85	0.85	0.65	0.79
Rel. Err. [%]	74	65	54	54	84	68
RMS [ $\text{kgm}^{-2}$ ]	0.26	0.23	0.18	0.18	0.32	0.26
Quantity	surface rain rate					
Pixels	all		ocean		land	
Frequencies	150.0,117.25, 340.0,176.31, 50.3	all	110.65,340.0, 117.65,150.0, 176.31	all	150.0,50.30, 176.31,117.65, 398.2	all
Correlation	0.62	0.67	0.74	0.8	0.59	0.64
Rel. Err. [%]	152	143	105	95	170	162
RMS [ $\text{mmh}^{-1}$ ]	2.54	2.39	1.53	1.38	3.29	3.14

Table 6.1: Performance of the rain water path, and rain rate retrieval in terms of correlations, relative errors, and root mean square error (RMS) for a combination of the five frequencies resulting in the lowest relative error and for a retrieval based on all frequencies. The five frequencies are sorted according to their importance beginning with the most important one.

## 6.4 Best frequency combination

Algorithms were also derived for a reduced number of frequencies without considering the provided spatial resolution from geostationary orbits, with the aim to investigate whether window frequencies or absorption channels have a higher potential for precipitation retrieval. The procedure started with finding the frequency channel with the highest correlation and then successively adding further channels, which reduced the relative error most strongly. It needs to be noted that sometimes the differences in performance between certain channels are very small. Therefore, it is possible that one frequency gives the strongest increase in correlation, but another one leads to a stronger reduction of the relative error.

Depending on whether the rain water path or the surface rain rate, land or ocean pixels are considered, different frequencies provide the most valuable information. The results for a retrieval based on the five most important frequencies in comparison to the one based on all frequencies is shown in Tab.6.1. Over the cold ocean the rain water path is directly related to the emission at frequencies along the wing of the oxygen line. The lowest frequency (e.g. 110.65 GHz) can be considered as a window channel. At this frequency, the emission signal is not disturbed by the ice particle scattering as this plays a minor role at these frequencies (Fig. 5.7). Therefore, for the rain water path retrieval, lower frequencies in the wings of the oxygen complex provide the most information, with additional information

content in the lower window channels. For the land surfaces, higher frequencies are favored as additional frequencies, since these are less influenced by the surface emissivity. When the surface rain rate is considered instead of the water column only, the window frequencies (89, 340, and 150 GHz) become more important, because these are more strongly related to the ice phase and the whole precipitation process. Over land the 150 GHz channel proves to be most valuable for the surface rain rate, but also channels above 300 GHz appear. Furthermore, including channels along the 118 GHz oxygen absorption line is very beneficial, since these also provide information on the temperature and thus, vertical position of the hydrometeors.

## 6.5 Database coverage

For the development of statistical retrieval algorithms, the database serving as a basis for the development needs to encompass the same diversity and variability as the measurements to which the retrieval algorithms should be applied. The necessity of a large variability can be clearly seen in Fig. 6.3, where the datasets were separated into a large training part (four of five cases; both time steps) and a small test part (one case; both time steps). In the next step, retrieval algorithms for land, ocean, and all pixels together were developed with the training dataset. Based on the derived coefficients, the retrieval was applied to the test case. This procedure was performed for every simulated case (Fig. 6.3). For all hydrometeor types in the Algiers flood case, the integrated amounts can not be retrieved by any means. Their relative errors reach values in the thousands percentages, even though the self-test for the training datasets are not worse than in the other cases. This is caused by the high number of hydrometeors occurring in the Algiers flood case. This variability, with values up to  $24 \text{ kgm}^{-2}$  and  $2.5 \text{ kgm}^{-2}$  for the maximum graupel and snow water paths, is not included in the training set, since the Algiers case itself is excluded. It is a good example for the failure of retrieval algorithms that are developed on a database that is not encompassing. The same holds for the graupel and snow water paths over land in the Elbe case. Apart from these outliers, the frozen hydrometeor amounts of the various cases can be retrieved quite well by algorithms based on a subset of the database. For the rain water path retrievals, the self-tests of the training datasets result in relative errors around 50%, which is similar to the one for all cases in Fig. 6.1. The algorithms applied to the test datasets produce worse results and cause a doubling of the relative errors in some cases. The retrieval of the surface rain rate has already large relative errors in the development stage. Therefore, the small increase of the relative errors from the development to the test stage can not be used to evaluate the complexity of the database.

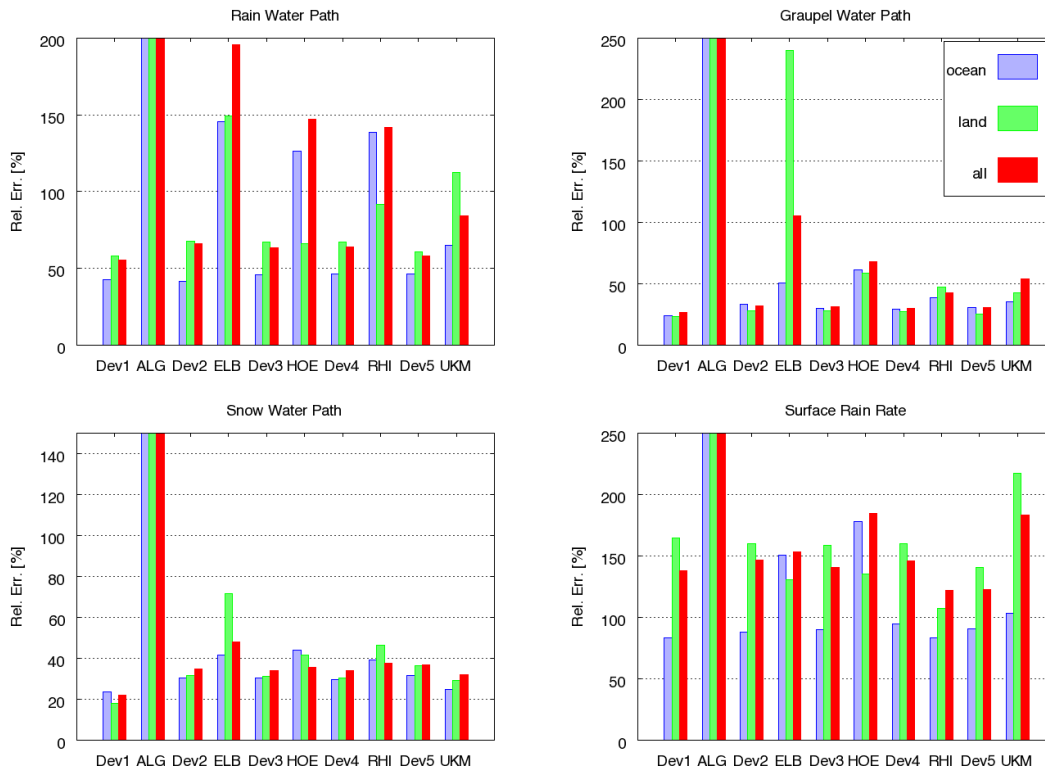


Figure 6.3: Tests of the representativeness of the database for rain water path, graupel water path, snow water path, and surface rain rate are shown. Dev1, Dev2, Dev3, Dev4, and Dev5 are the training datasets for the retrieval development built by excluding the case shown rightward of each development dataset. The resulting coefficients are applied to retrieve the amounts of the actual quantities of the excluded case. The performance of the retrievals is shown in terms of relative errors. For the Algiers flood case, the relative errors are truncated.

# Chapter 7

## COSMO-DE evaluation by SynSatMic

In chapter 4, SynSatMic has been introduced. Comparisons of this model-to-satellite approach to satellite observations in the microwave range showed good agreement as long as the CRMs are able to capture the atmospheric state correctly. Therefore, it suggests itself to use SynSatMic for evaluation purposes of CRMs. Since the previous chapters showed that there is a clear relation between hydrometeor contents and simulated brightness temperatures, this tool can serve as an instrument to systematically and rapidly evaluate the liquid and ice amounts predicted by the cloud schemes of CRMs. The evaluation can be carried out by performing simulations for times and locations where satellite overpasses with appropriate instruments in the microwave range on board are available.

In this chapter, two case studies are presented in which SynSatMic is applied on COSMO-DE simulations to evaluate the predicted hydrometeor fields by comparison to AMSU-B observations.

### 7.1 Case study - stratiform precipitation

The synoptic situation on August 3, 2006 was dominated by an upper-level trough over Central Europe associated with a surface low over the North Sea. While moving south-eastwards, the surface low split up into two systems: one was located over Denmark and the Baltic Sea, while the other one was moving slowly along the southern side of the Alps from France to Slovenia, which is typical for a Vb track (*Hess and Brezowsky, 1977*). This constellation of the low-level pressure systems and the upper-level trough leads to northerly winds over south-east Germany, northern Austria, and the Czech Republic below 2-4 km. Southerly winds above, advected warm and humid air from the Mediterranean Sea northwards. These air masses were lifted by the northerly up-sloping flow at low levels causing hydrometeor development and long-lasting continuous rainfall in south-east Germany, northern Austria, and the South of the Czech Republic.

On August 3, 2006 at 11 UTC, AMSU-B on board NOAA-16 passed over Europe with a FOV covering almost the whole COSMO-DE area. Therefore, the forecast valid for 11 UTC of the COSMO-DE run, which has been initialized at 00 UTC, has been selected for the

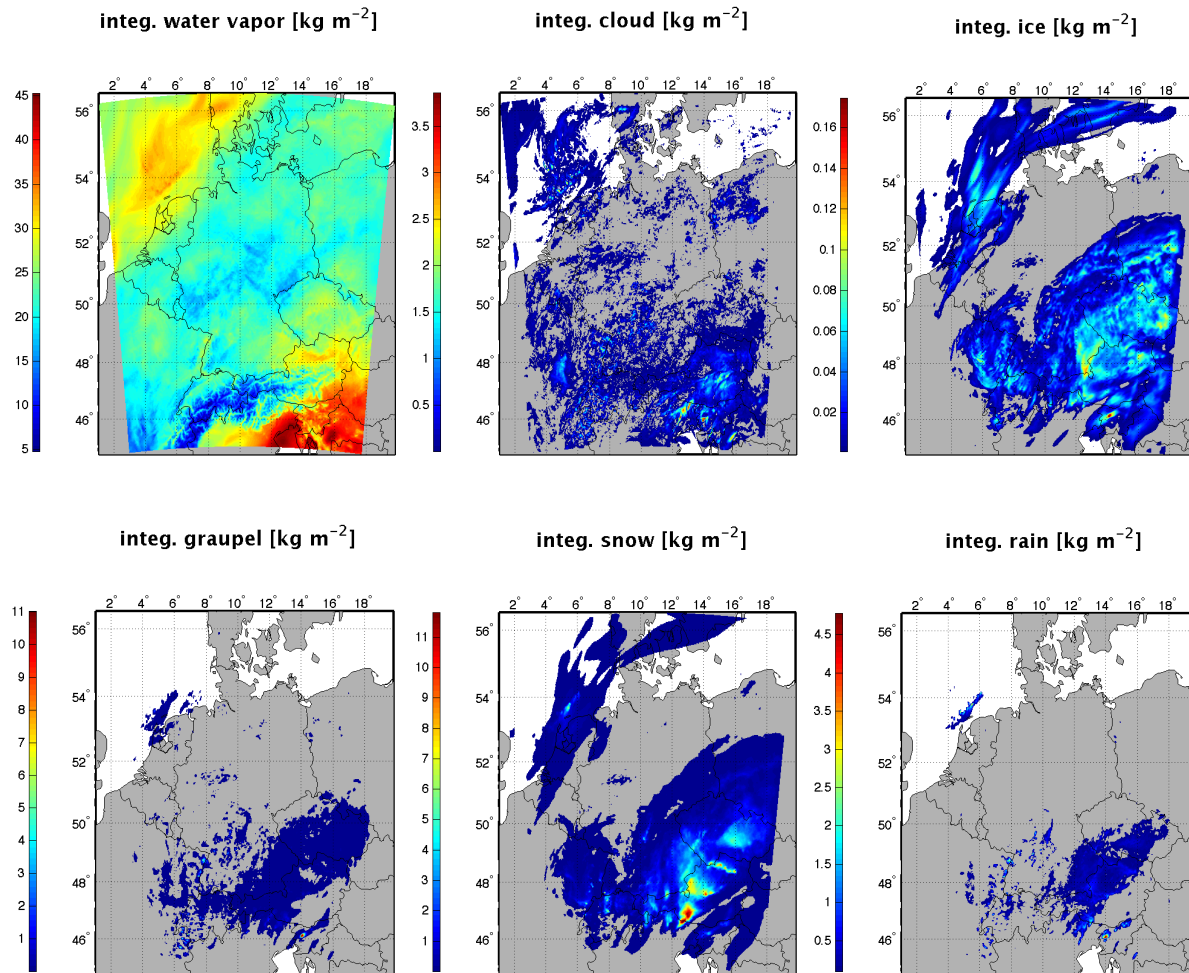


Figure 7.1: Vertically integrated water categories (water vapor, cloud water, ice crystals, graupel, snow, and rain) in  $[\text{kgm}^{-2}]$  for August 3, 2006 simulated with COSMO-DE at 11UTC for a run initialized at 00 UTC.

evaluation. In Fig. 7.1, the vertically integrated hydrometeor categories simulated with the model for the overpass time are shown. The integrated water vapor clearly indicates the warm humid air south-easterly of the Alps. In the eastern part and north-east of the Alps, an area with moderate graupel and large snow amounts can be found.

The observation of AMSU-B at 150 GHz shows a large area of low brightness temperatures extending from the South of the Czech Republic over south-eastern Germany and western Austria to north-eastern Italy (Fig. 7.2). Furthermore, an area of cold brightness temperatures is apparent over the Netherlands. These cold temperatures indicate the presence of strongly scattering frozen particles like snow or graupel most likely accompanied with precipitation below. The comparison with the simulations based on COSMO-DE shows that the location of the area of lower brightness temperatures north-east of the Alps is well captured by the simulation but with a weaker brightness temperature depression

than in the observation. This means that the location of the lifting is correct but the amount of the associated hydrometeor development is too small. The area of low brightness temperature over the Netherlands is only very weak in the simulation in comparison to the observation. This indicates, that the CRM did not develop the necessary amount of snow or graupel to produce a similar brightness temperature depression as in the satellite observation. Because of the underestimation of the hydrometeor formation, less scattering takes place leading to higher brightness temperatures in most pixels. Thus, the histograms for the brightness temperature distribution at 150 GHz (Fig. 7.3) show much more pixels without depressions through scattering for the simulations over land than for the observations. For these pixels brightness temperatures around 280 K have been simulated. Since ocean surfaces cover only a small part of the simulation area, not many pixels are available for a reasonable comparison. Therefore, the corresponding histograms have to be handled with care. The simulated spatial distributions of the integrated hydrometeors (Fig. 7.1) show almost no significant contents for snow and graupel leading to scattering at 150 GHz. Consequently, no brightness temperature depression is simulated. The hydrometeors over the Netherlands causing the scattering in the observations extend over the North Sea leading to lower brightness temperatures in the histogram for the simulations over ocean pixels. The slightly colder temperatures in the observation in the north-eastern corner of the simulation area can have several reasons. The most obvious reason would be a missing hydrometeor field in the simulations. Another possibility is the surface emissivity. Due to water vapor absorption, the influence of the surface emissivity is small at 150 GHz. Differences between observation and simulation in the sea surface emissivity can still be noticeable. These can be related to the sea surface temperature or inaccuracies within the applied ocean emissivity model. Another reason can be the convolution process. The fraction of vertical and horizontal polarization in the received radiation by the AMSU-B sensors is dependent on its observation angle. The function to describe this dependence in the convolution process can only be approximated. This can cause differences, especially over ocean surfaces where the emissivity has a strong polarization dependence.

That none of these possibilities cause directly the differences can be seen by the comparison for the 182.31 GHz channel (Fig. 7.4). The influence of the different surfaces is not apparent any more in the 182.31 GHz channel, since it is close to the H<sub>2</sub>O absorption line. Therefore, it is more sensitive to upper tropospheric water vapor. The more water vapor is present the less deep into the atmosphere can be seen by the sensors and the colder the brightness temperature are. Observation and simulation (Fig. 7.4) agree well at this channel. Over north-eastern Germany, Poland, and the Baltic Sea the observation seems to be drier than the simulation. Within this dry area, the damping by water vapor is reduced. Therefore, the colder ocean surface has a stronger influence on the signal at 150 GHz leading to the colder brightness temperatures for this area that were mentioned in the discussion for the comparison at 150 GHz. Although the signal is damped by water vapor, scattering associated with frozen hydrometeors in deep cloud systems can still contribute to the signal at 182.31 GHz. This causes the depressed brightness temperatures within the deep cloud system over the Netherlands that is not apparent in the simulations. The dry area over the Baltic Sea and the area of brightness temperature depression over

the Netherlands, both can be seen as well in the histograms (Fig. 7.5). For land and ocean the simulations show colder brightness temperatures than the observations. Due to the water vapor damping the broadening of the brightness temperature distribution is not as strong as for window channels.

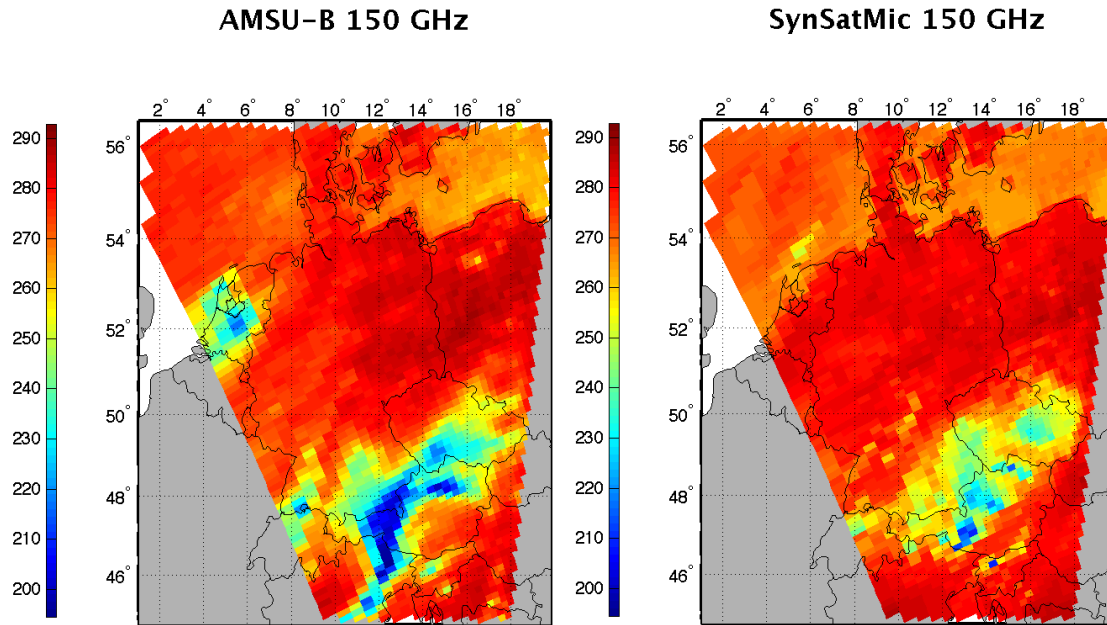


Figure 7.2: AMSU-B observation (left) and SynSatMic simulation (right) for 150 GHz on August 3, 2006 at 11 UTC.

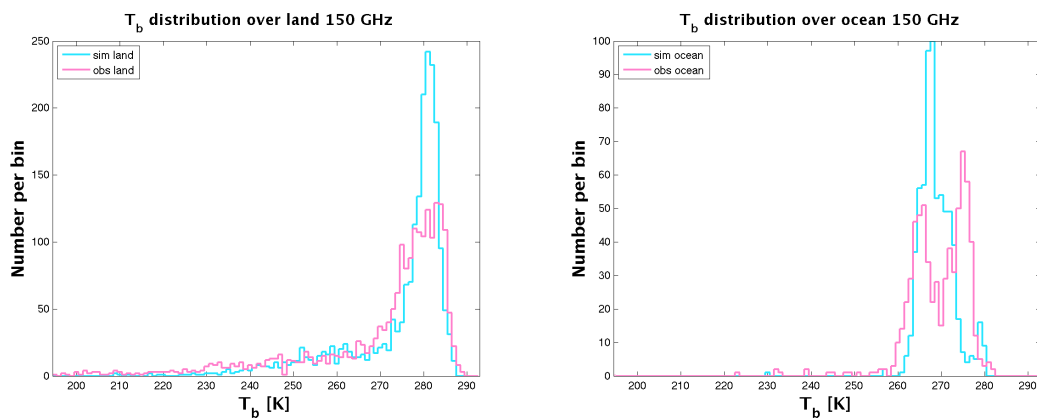


Figure 7.3: Brightness temperature distribution for 150 GHz on August 3, 2006 at 11 UTC separated into ocean and land pixels: AMSU-B observation (magenta) and SynSatMic simulation (blue).

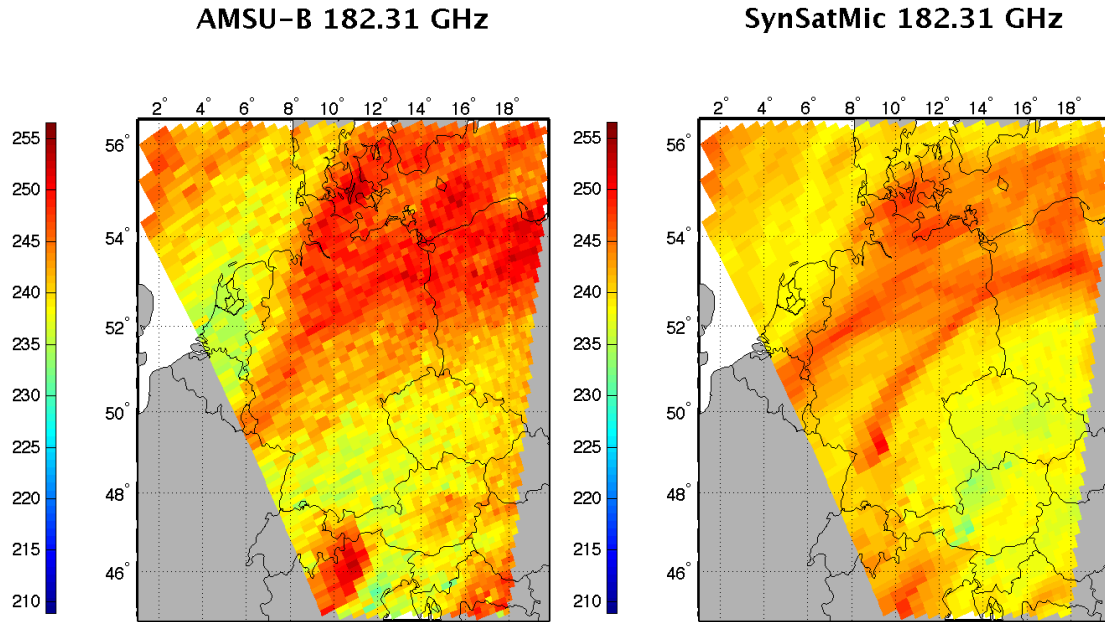


Figure 7.4: Same as Fig. 7.2 but for 182.31 GHz.

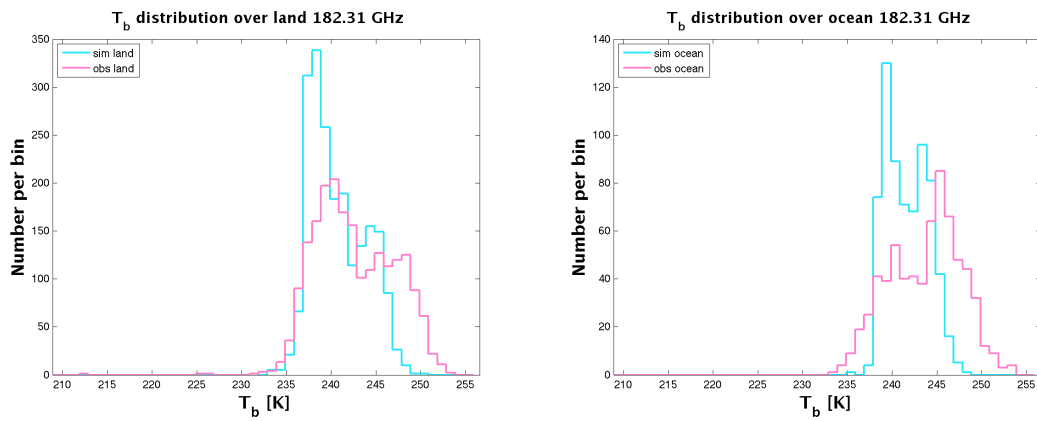


Figure 7.5: Same as Fig. 7.3 but for 182.31 GHz.

## 7.2 Case study - convective precipitation

On August 28, 2006, a low pressure system was located over Denmark. At noon, the associated cold front was over north-western France moving with a strong north-westerly upper air flow towards the Alps. Ahead of the cold front, the leftovers of a warm front passed Southern Germany in the early afternoon associated with weak stratiform precipitation. The stratiform precipitation was present during the whole afternoon and enhanced additionally by a small low developing over the Alps. In conjunction with the passage of the cold front embedded convection has been triggered and the front developed into a narrow band of strong precipitation.

NOAA-17 with AMSU-B on board passed Central Europe at 14UTC on August 28, 2006. The corresponding water vapor and hydrometeor output fields of the COSMO-DE run for 14 UTC, which has been initialized at 00 UTC on that day, are presented in Fig. 7.6. Indicated by the maxima in rain, snow, and graupel contents, convection is apparent in western and south-western Germany. Areas of moderate snow and graupel contents can be found over the Alpine region.

Fig. 7.7 shows the results for the AMSU instrument and the observations at 89 GHz. At 89 GHz the surface emissivity has a significant influence on the brightness temperature at the top of the atmosphere. Pronounced differences between land and ocean surfaces are observable in the brightness temperature fields. Thereby, the simulation seems to be warmer. In the observation, a band of low brightness temperatures due to scattering at frozen particles extends from the North Sea to western Czech Republic. This band is not apparent in the simulation. However, the brightness temperature distribution over the western and southern part of Germany and the Alpine region agrees well with slightly warmer simulations. The comparison with the integrated hydrometeor contents (Fig. 7.6) shows that these brightness temperature depressions are related to convection with enhanced snow contents. The convective area over Southern Germany is almost not present in the model. Nevertheless the histograms (Fig. 7.8) show good agreement between simulation and observation over land. The large differences seen in the histograms for ocean pixels are associated with differences in hydrometeor contents over the North Sea. At this frequency, the emission by hydrometeors increases the brightness temperature compared to the cold ocean. In addition, the sensitivity of this channel to surface influences and the fact that the surface emissivity is not easy to model in the microwave range, results in simulations being too cold.

The 176.31 GHz channel yields similar results (Fig. 7.9) like the 89 GHz comparison for land pixels. As for the 182.31 GHz channel shown in the stratiform case study (sec. 7.1), the water vapor damping covers the influence of the different surface types. Since the 176.31 GHz channel is more on the wing of the H<sub>2</sub>O absorption line, the damping is not as strong. Therefore, scattering at large frozen hydrometeors leading to brightness temperature depressions, is dominating the spatial distribution. With the exception of the scattering over Central Germany and the North Sea, the spatial distribution of scattering and therefore the frozen hydrometeors are well captured by the model. The depression in brightness temperature in the convective cores over western Germany is much too large in

the simulation. This indicates an overestimation of the convection, resulting in an overestimation of hydrometeor contents. Nevertheless, the histograms for this channel over land agree well, except of the simulated low brightness temperatures in the convective cores. Over ocean the afore mentioned hydrometeor field in the observations over the North Sea results in a broadening of the observed distribution.

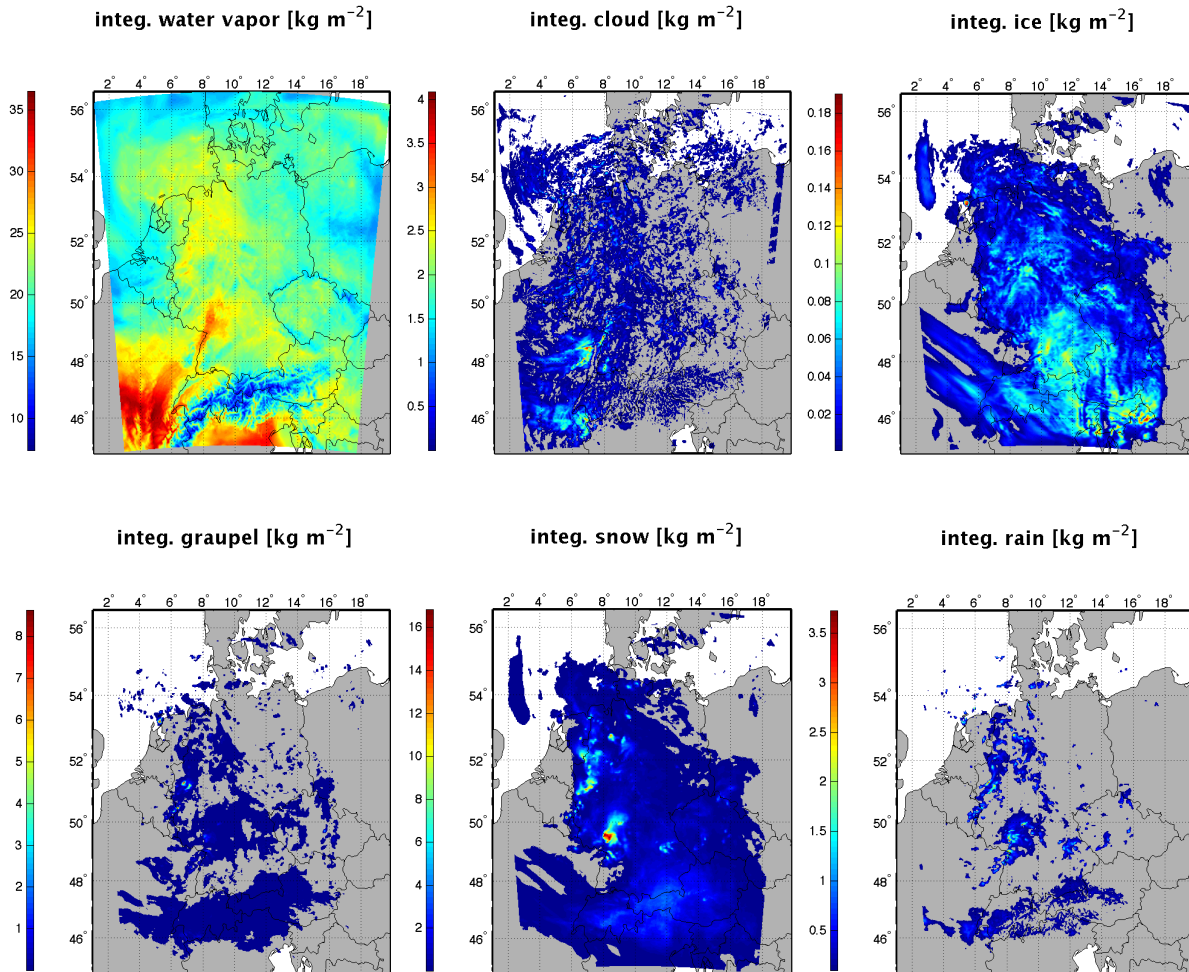


Figure 7.6: Vertically integrated water categories (water vapor, cloud water, ice crystals, graupel, snow, and rain) in  $[\text{kgm}^{-2}]$  for August 28, 2006 simulated with COSMO-DE as an 14 hour forecast valid for 14 UTC.

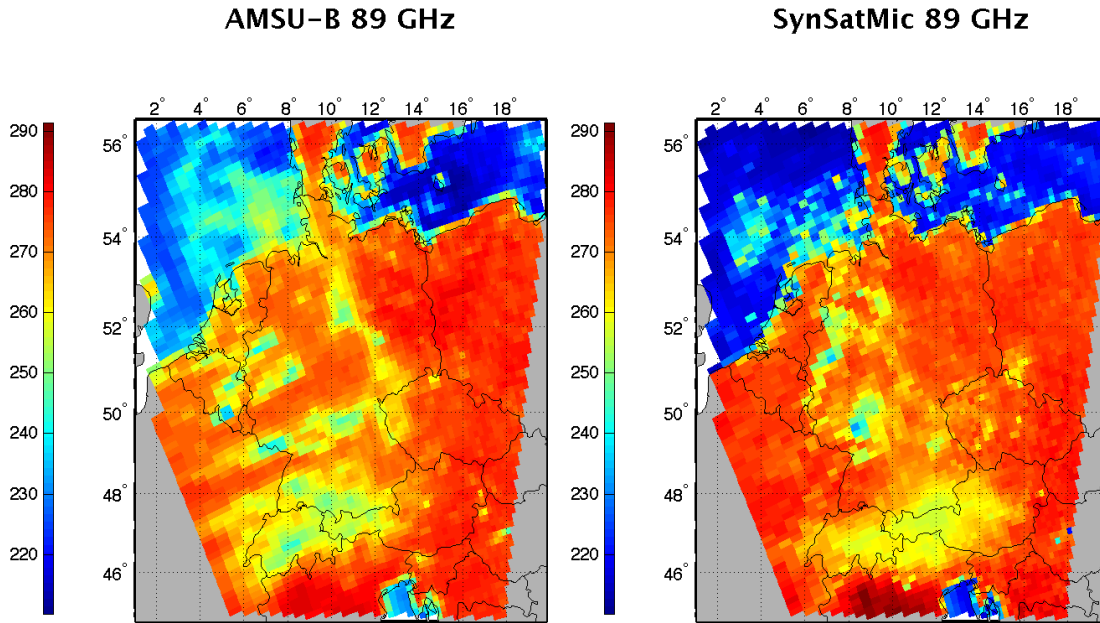


Figure 7.7: AMSU-B observation (left) and SynSatMic simulation (right) for 89 GHz on August 28, 2006 at 14 UTC.

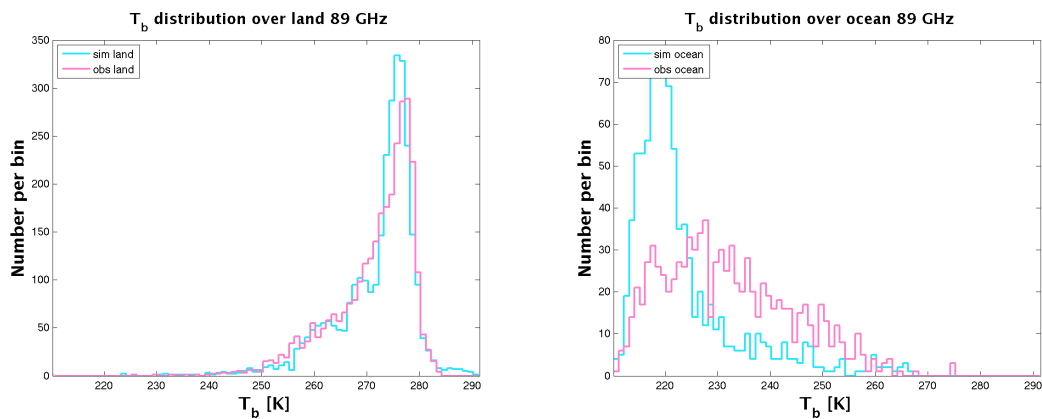


Figure 7.8: Brightness temperature distribution for 89 GHz on August 28, 2006 at 14 UTC separated into ocean and land pixels: AMSU-B observation (pink) and SynSatMic simulation (blue).

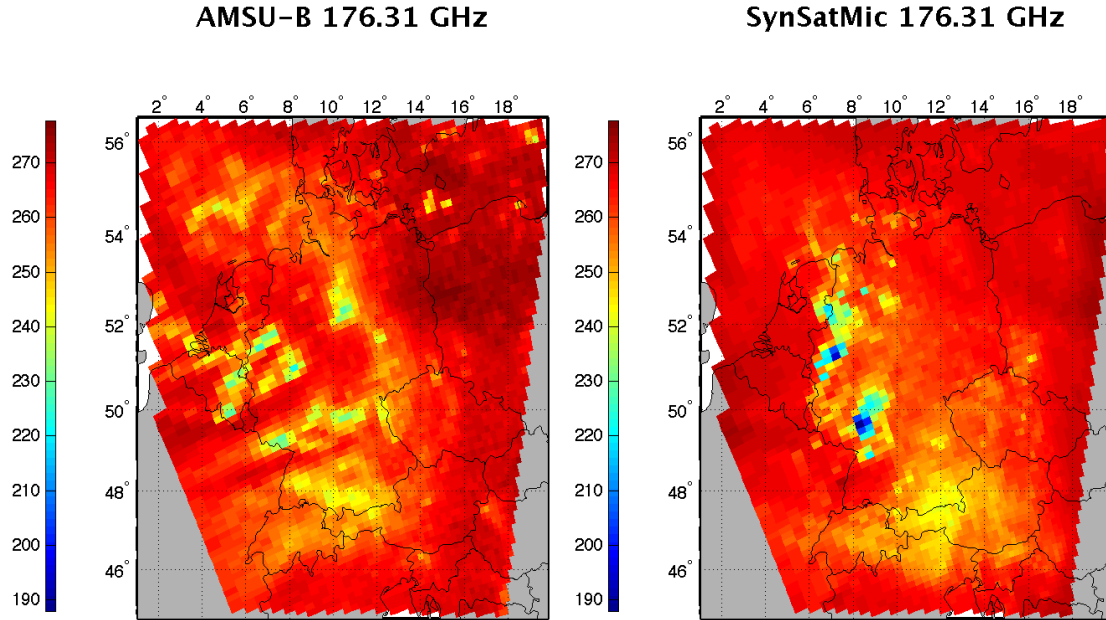


Figure 7.9: Same as Fig. 7.7 but for 176.31 GHz.

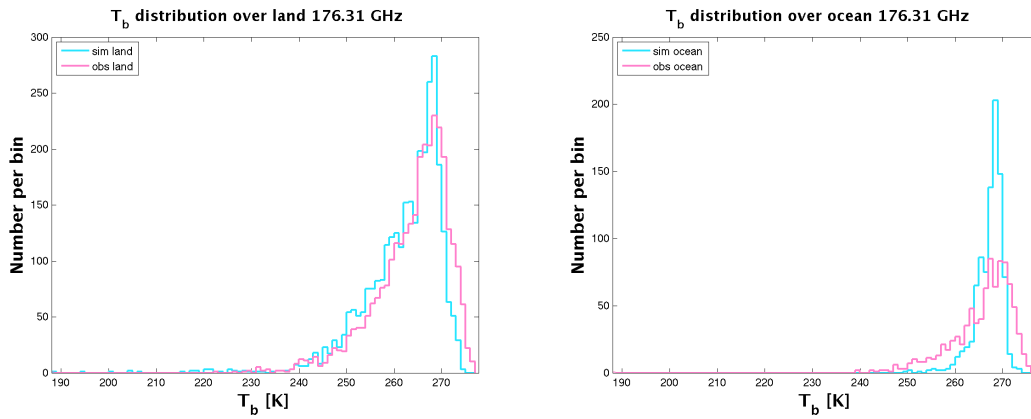


Figure 7.10: Same as Fig. 7.8 but for 176.31 GHz.



# Chapter 8

## Conclusions and Outlook

In this thesis the potential of the millimeter- and submillimeter-wavelength region for hydrometeor and precipitation observations from space has been investigated. For that purpose, the Synthetic Satellite simulator for the Microwave region (SynSatMic) has been developed. By applying this tool to CRM simulations for five mid-latitude precipitation cases, a database of simulated brightness temperatures at 18 frequencies with corresponding integrated hydrometeor contents has been created. The information content of this database has been investigated with simple retrieval approaches. In two case studies, SynSatMic has been utilized as a tool to evaluate the simulated hydrometeor fields of CRMs by comparing the simulations to microwave satellite observations.

The need of precipitation and hydrometeor observations with a temporal and spatial resolution sufficient for NWP, NWC, and hydrological applications, is a challenging task (*Rizzi et al., 2006*) and not easy to achieve. Millimeter- and submillimeter-wavelength observations with space-borne sensors could fulfill the requirements posed by this applications. One of the major problems for precipitation retrievals based on observations in the higher frequency range is the relationship between cloud ice and precipitation (*Bizzarri, B. et al., 2005*). The high sensitivity of the brightness temperatures at higher microwave frequencies to variations in the hydrometeor contents has been shown by calculating Jacobians for cross sections through precipitation systems. Thereby, the interaction between emission in the lower liquid layers and the scattering at frozen hydrometeors aloft could be seen clearly. By applying frequencies with different sensitivities with respect to height, it is possible to sound the vertical hydrometeor profiles. In general, increasing the contents of frozen hydrometeors causes a depression in the brightness temperature at the top of the atmosphere. Due to snow wetness, the brightness temperature at the top of the atmosphere responded with an increase to variations in the snow contents just above the freezing level. The surface emissivity had no influence on the simulated brightness temperatures at the investigated frequencies.

Since only few measurements by aircrafts are available at these high frequencies, intensive modeling is required for better understanding of the problem of the relationship between hydrometeors and microwaves. By the coupling of CRMs (Meso-NH and COSMO-DE) and the RT model MWMOD, a tool to simulate satellite observations for

the millimeter- and submillimeter-wavelength region was compiled. Thereby, considering two different CRMs is meaningful since each cloud microphysical scheme represents the PSDs in different ways. Although the surface emissivity has no influence at frequencies above 150 GHz, it has been included by explicit modeling for ocean surfaces and by emissivity maps for land surfaces. The simulations resulting from such a model framework, consisting of a CRM coupled to a RT model, have been analyzed by comparisons with SSM/I and AMSU observations. This resulted in a good agreement. Differences in the brightness temperature fields can be associated to the CRM simulations of the hydrometeor fields or to the representation of frozen hydrometeor categories within the calculation of the single-scattering parameters.

Simulations with Méso-NH for five mid-latitude precipitation events at two time steps were performed and resulted in approximately 250000 atmospheric profiles, where on average 60% of those contained hydrometeors. By the five selected cases, a reasonable number of heterogeneous precipitation types is covered, from strong, convective to light winter cases. The analysis of the surface precipitation rates, the hydrometeor profiles and contents clearly showed that the cold rain process, in which frozen particles are formed and later on melt to rain, is the dominant precipitation mechanism in mid-latitude precipitation systems. Thereby, the relationship between liquid layers underneath frozen layers is strongly determined by the height of the 0°C isotherm. The cold rain process could be identified as well by the high correlations between the total column contents for the frozen hydrometeors and the surface precipitation rates. In comparison to simulations for the tropics, like in the GPROF database (*Kummerow et al.*, 2001; *Olson et al.*, 2006), where convective cases dominate, the mid-latitude database includes more stratiform precipitation systems. Furthermore, by the differences in the altitude of the 0°C isotherm (1 to 3 km in the mid-latitudes and of about 4.5 km in the tropics), the vertical distribution of the hydrometeors is different.

Based on the profiles of the mid-latitude database, forward modeling with the RT model MWMOD has been performed to achieve brightness temperatures at 18 frequencies for a set of nine zenith angles. The integrated hydrometeor contents together with the corresponding brightness temperatures assemble an unique database for the mid-latitudes, with an ample information content for the estimation of the potential of hydrometeor and precipitation observations in the millimeter- and submillimeter-wavelength region. High values were found for the correlation between the integrated snow and graupel contents and the brightness temperatures at channels sensitive to scattering at frozen hydrometeors. This indicates a high potential of these frequencies for the observations of snow and graupel. At lower window channels (50.3 and 89 GHz), positive correlations were found for all frozen and precipitating hydrometeor types (except graupel) over ocean and negative ones over land. Above 176.31 GHz, the correlations were negative, independent of the surface type.

Multiple regression algorithms have been developed on the basis of the database of brightness temperatures and concurrent hydrometeor contents. The first conclusion to be drawn from analyzing the retrievals is indeed the potential of millimeter- and submillimeter-wavelengths to sense atmospheric hydrometeors. Especially for graupel and snow very good retrieval accuracies (< 30%) are achieved. For these hydrometeor types, even with

algorithms based only on frequencies larger than 150 GHz, these simple retrievals show good performance, as long as the cases are not strongly convective. Such frequencies are of special interest, since they are suitable for geostationary applications. The performance for the rain water path and surface rain rate is lower: for convective situations (for example the Algiers case) relative errors in surface rain rate can exceed 100%, while for stratiform cases (for example the Hoek case) much better results (40%) are obtained.

The surface emissivity plays a role for frequencies lower than 176 GHz and therefore, separate algorithms for land and ocean areas should be developed. Tests of the adaptability have shown that for the retrieval development the database needs to encompass the whole spectrum of the hydrometeor contents and needs to include a large variability of precipitation cases to result in acceptable retrieval results. While the database developed in this study seems to include a broad repertoire of frontal situations, it should be expanded with more convective cases since these seem to be underrepresented. A general extension of the database would be preferable, since the quality of statistical algorithms is strongly dependent on the scope of the underlying database. The promising results achieved for specific cases suggest that for future retrieval approaches it might be worth to classify the situations first. For example a discrimination between stratiform and convective situations or a classification of rainy and non-rainy or non rainy, low precipitating, and high precipitating could be performed prior to any quantitative precipitation retrieval.

The high retrieval potential for the different hydrometeor types indicates that satellite observations in the microwave region could play an important role in evaluating the performance of numerical weather prediction models. For example, graupel and snow are prognostic model parameters and essential in the cloud schemes for determining the forecasted precipitation rate at the ground. By comparing simulated brightness temperature fields and AMSU-B observations, the potential of SynSatMic for the evaluation of CRMs microphysical schemes has been shown in two case studies. Thereby, the general nature of the precipitation systems (stratiform and convective) has been well captured by COSMO-DE. The intensity of the brightness temperature depression associated with scattering at frozen hydrometeors did not agree well. Overestimation in the convective case and underestimation in the stratiform case have been found. Channels sensitive to water vapor showed good agreement between model and simulations.

The description of the single-scattering properties of non-spherical frozen hydrometeors at millimeter- and submillimeter-wavelengths within the RT calculations has been identified as a major problem. Studies where the particles have been described with spherical approximations like the soft sphere approximation (*Liu, 2004*) have revealed that such approximations become poor if realistic ice densities are used. Furthermore, the applied mixing theories are inappropriate to treat irregularly shaped hydrometeors with large size parameters. Therefore realistic ice habits should be used (*Liu, 2004; Kim et al., 2007; Mugnai et al., 2005*). The treatment of light scattering at non-spherical particles can be approached with different methods (*Mishchenko et al., 2002*). By applying the Discrete Dipole Approximation (DDA, *Draine and Flatau, 2000*), the single-scattering properties of arbitrarily shaped particles can be described very accurately. Unfortunately, calculations with the DDA are very time consuming.

Within the TOSCA study (Toward an Optimal-based Snow Characterization Algorithm; *Battaglia et al.*, 2006), the single-scattering database initially created within the ESA-ESTEC project "Development of a radiative transfer model for the frequency range between 200 and 1000 GHz" (*Sreerekha et al.*, 2005) will be extended by a large number of crystal sizes and habits. The information contained in this database can be used for the SynSatMic framework by calculating parameters following *Liu* (2004) for the soft-sphere approximation of the different habits at frequencies operational on current satellites. Another benefit of the single-scattering database would be the possibility to directly access the information by an appropriate interface. Thereby the single-scattering properties of snow particles can be described accurately within the RT calculations. This could significantly improve the performance of SynSatMic and reduce the uncertainty within the comparison to satellite observations. Furthermore, using the pre-calculated single-scattering properties contained in the database will result in a speed improvement of the simulations.

In preparation for future satellite programs, many missions have been recently proposed considering observations in the millimeter- and submillimeter-wavelength region from geostationary or low Earth orbits. By such missions the uncertainties related to atmospheric hydrometeors within NWP and climate models can be further reduced, since to a good deal these are related to the lack of adequate observations.

The primary objective of the Geostationary Observatory for Microwave Atmospheric Sounding (GOMAS, *Bizzarri, B. et al.*, 2005) mission is the measurement of the precipitation with a sampling rate compatible with the naturally high temporal variability of the precipitation events. The secondary objective is to provide nearly all-weather temperature and water vapor profiles of the atmosphere. By the concept of the instrument, scans of the whole Earth-disc from geostationary orbit will be possible. The selection of the frequencies (from 50 to 428 GHz) concentrates along the wings of absorption lines covering a large spectral range with different sensitivities to the full atmospheric column, including hydrometeor characteristics (e.g., phase, size, and altitude) both, in clouds and in precipitation. The potential of this frequency range to observe hydrometeors and precipitation has been shown in this thesis and recently by *Defer et al.* (2007).

The Cloud Ice Water Submillimeter Imaging Radiometer (CIWSIR, *Bühler et al.*, 2005b) mission is devoted to gather global ice cloud characteristics by submillimeter observations to close the gap in the observation system between radar being sensitive to larger particles and infrared observations probing thin cirrus. The CIWSIR prototype instrument concept has a conical scanning geometry from low Earth orbit at an incident angle around  $53^\circ$  to achieve a near-global horizontal coverage in 24 h. The proposed frequencies cover the millimeter and submillimeter range between 183 and 664 GHz. For simultaneous infrared data, the mission will fly in tandem with one of the MetOp satellites. Retrieval simulations similar to the one performed for GOMAS have been conducted for the CIWSIR frequencies (*Bühler et al.*, 2007; *Jiménez et al.*, 2007) to demonstrate that the prototype concept meets the scientific mission requirements. *Bühler et al.* (2007) and *Jiménez et al.* (2007) found high sensitivities to integrated quantities like ice water paths (IWP) with a relative accuracy of approximately 20% and a detection threshold of approximately  $2 \text{ gm}^{-2}$ . An accuracy of approximately  $30 \mu\text{m}$  could be achieved for the median mass equivalent-sphere

diameter of the ice particles.

Before satellites are launched, the capabilities of the proposed frequency bands are tested on airborne simulators. Currently, two such simulators for the millimeter- and submillimeter-wavelength region are established. The HALo Microwave Package (HAMP) is currently being built to fly on the High Altitude and LOng range research aircraft (HALO) covering the frequency range up to 183 GHz with channels at 54, 118, and 183 GHz. Its expected to be operational in 2010. As a complement to HALO-HAMP, an airborne demonstrator will be established within the ESA project "Study of a submillimeter-wave airborne demonstrator for observations of precipitation and ice clouds" to prove the scientific mission concepts of CIWSIR and GOMAS. The data collected by both demonstrators will help to understand more the relation between hydrometeors and higher microwave observations.

Within this thesis, SynSatMic has been developed for two applications: first, for the creation of a database of simulated brightness temperatures with concurrent hydrometeor contents and second, for model evaluation purposes. Both applications have been demonstrated and showed promising results. With regard to an increasing interest in the millimeter- and submillimeter-wavelength region for hydrometeor observations and for future satellite applications, an extension of the database is desirable. Therefore, to increase the diversity of precipitation systems in the database, more convective cases should be included. For further studies on best frequency selection, the frequency bands considered in the GOMAS and CIWSIR missions should be included in the simulations as well. SynSatMic as a tool for model evaluation can be applied for case studies as well as for long term evaluations with operational satellites in the microwave range. Up to now, the simulations are still very time consuming due to the single-scattering calculations. Once an appropriate database with single-scattering properties for the microwave region is set up, the calculation of microwave brightness temperatures routinely should be possible.



# Bibliography

- Argence, S., D. Lambert, E. Richard, N. Söhne, J.-P. Chaboureau, F. Crépin, and P. Arbogast (2006), High resolution numerical study of the Algiers 2001 flash flood, *Adv. Geosciences*, 7, 251–257.
- Battaglia, A., U. Löhnert, G. Peters, and M. Hagen (2006), Toward an Optimal-based Snow Characterization Algorithm (TOSCA), Proposal to Deutsche Forschungs Gesellschaft (DFG).
- Bauer, P. (2002), Introduction to microwave radiative transfer, *Tech. rep.*, ECMWF.
- Bauer, P., and A. Mugnai (2003), Precipitation profile retrievals using temperature-sounding microwave observations, *J. Geophys. Res.*, p. 4730.
- Bauer, P., P. Amayenc, C. D. Kummerow, and E. A. Smith (2001), Over-ocean rainfall retrieval from multisensor data of the Tropical Rainfall Measuring Mission. Part II: Algorithm implementation, *J. Atmos. Ocean. Tech.*, 18, 1838–1855.
- Bauer, P., E. Moreau, and S. D. Michele (2005), Hydrometeor retrieval accuracy using microwave window and sounding channel observations, *J. Appl. Meteorol.*, 44, 1016–1032.
- Bauer, P., P. Lopez, A. Benedetti, D. Salmond, and E. Moreau (2006), Implementation of 1D+4D VAR assimilation of microwave radiances in precipitation at ECMWF. Part I: 1D-VAR, *Q. J. Roy. Meteor. Soc.*, 132(620), 2277–2306.
- Bennartz, R., and P. Bauer (2003), Sensitivity of microwave radiances at 85-183 GHz to precipitating ice particles, *Radio Sci.*, 38(4).
- Bennartz, R., and G. W. Petty (2001), The sensitivity of microwave remote sensing observations of precipitation to ice particle size distributions, *J. Appl. Meteorol.*, 40, 345–364.
- Bizzarri, B. et al. (2005), GOMAS - Geostationary Observatory for Microwave Atmospheric Sounding, submitted to ESA in response to the call for ideas for the Next Earth Explorer Core Missions.
- Bohren, C. F., and E. E. Clothiaux (2006), *Fundamentals of Atmospheric Radiation*, WILEY-VCH Verlag GmbH & Co. KGaA.

- Browning, K. A., R. S. Dixon, C. Gaffard, and C.-G. Wang (2001), Wind-profiler measurements in the storm of 30 October 2000, *Weather*, *56*, 367–373.
- Bühler, S. A., P. Eriksson, T. Kuhn, A. von Engeln, and C. Verdes (2005a), ARTS, the Atmospheric Radiative Transfer Simulator, *J. Quant. Spectrosc. Ra.*, *91*(1), 65–93.
- Bühler, S. A., et al. (2005b), Cloud Ice Water Submillimeter Imaging Radiometer, *Proposal*, ESA.
- Bühler, S. A., et al. (2007), A concept for a satellite mission to measure cloud ice water path, ice particle size, and cloud altitude, *Q. J. Roy. Meteor. Soc.*, *133*, 109–128.
- Caniaux, G., J.-L. Redelsperger, and J.-P. Lafore (1994), A numerical study of the stratiform region of a fast-moving squall line. Part I: General description, and water and heat budgets, *J. Atmos. Sci.*, *51*, 2046–1074.
- Chaboureau, J.-P., J.-P. Cammas, P. Mascart, J.-P. Pinty, C. Claud, R. Roca, and J.-J. Morcrette (2000), Evaluation of a cloud system life-cycle simulated by the Méso-NH model during FASTEX using METEOSAT radiances and TOVS-3I cloud retrievals, *Q. J. Roy. Meteor. Soc.*, *126*, 1735–1750.
- Chaboureau, J.-P., J.-P. Cammas, P. Mascart, J.-P. Pinty, and J.-P. Lafore (2002), Mesoscale model cloud scheme assessment using satellite observations, *J. Geophys. Res.*, *107*(D16), 4301.
- Chaboureau, J.-P., J. P. Pinty, I. Meirold-Mautner, C. Prigent, M. Mech, and S. Crewell (2007), A midlatitude cloud database validated with satellite observation, *submitted to J. Appl. Meteorol.*
- Chen, F. W., and D. H. Staelin (2003), AIRS/AMSU/HSB precipitation estimates., *IEEE T. Geosci. Remote*, *41*, 410–417.
- Crewell, S., et al. (2005), Simulation study of precipitating clouds from geostationary orbits with passive microwaves, *Final report*, EUMETSAT, [http://www.eumetsat.int/groups/pps/documents/document/pdf\\_mtg\\_rep20.pdf](http://www.eumetsat.int/groups/pps/documents/document/pdf_mtg_rep20.pdf), contract No. EUM/CO/04/1311/KJG.
- Czekala, H. (1999), Microwave radiative transfer calculations with multiple scattering effects by nonspherical hydrometeors, Ph.D. thesis, Rheinische Freidrich-Wilhelms-Universität Bonn.
- Czekala, H., and C. Simmer (1998), Microwave radiative transfer with nonspherical precipitating hydrometeors, *J. Quant. Spectrosc. Ra.*, *60*(3), 365–374.
- Czekala, H., and C. Simmer (2002), On precipitation induced polarization of microwave radiation measured from space, *Meteorol. Z.*, *11*(1), 49–60.

- Czekala, H., S. Havemann, K. Schmidt, T. Rother, and C. Simmer (1999), Comparison of microwave radiative transfer calculations obtained with three different approximations of hydrometeor shape, *J. Quant. Spectrosc. Ra.*, *63*, 545–558.
- Defer, E., C. Prigent, F. Aires, J. R. Pardo, C. J. Walden, O.-Z. Zanifé, J.-P. Chaboureau, and J.-P. Pinty (2007), Development of precipitation retrievals at millimeter and sub-millimeter wavelengths for geostationary satellites, *J. Geophys. Res.*
- Doherty, A. M., T. R. Sreerexha, U. M. O’Keeffe, and S. J. English (2007), Ice hydrometeor microphysical assumptions in radiative transfer models at AMSU-B frequencies, *Q. J. Roy. Meteor. Soc.*
- Doms, G., and U. Schättler (2002), A description of the nonhydrostatic regional model LM. Part I: Dynamics and numerics, *Tech. rep.*, DWD.
- Doms, G., J. Förstner, E. Heise, H.-J. Herzog, M. Raschendorfer, R. Schrodin, T. Reinhardt, and G. Vogel (2004), A description of the nonhydrostatic regional model LM. Part II: Physical parameterization, *Tech. rep.*, DWD.
- Draine, B. T., and P. J. Flatau (2000), Discrete-dipole approximations for scattering calculations, *J. Opt. Soc. Am.*, *11*, 1491–1499.
- Draine, B. T., and P. J. Flatau (2003), *User guide to the Discrete Dipole Approximation code DDSCAT 6.0*, <http://arxiv.org/abs/astro-ph/0300969>.
- Ducrocq, V., D. Ricard, J.-P. Lafore, and F. Orain (2002), Storm-scale numerical rainfall prediction for five precipitating events over France: On the importance of the initial humidity field, *Weather Forecast.*, *17*, 1236–1256.
- English, S., and T. Hewison (1998), A fast generic millimeter-wave emissivity model., in *Proceedings of SPIE*, pp. 288–300.
- Evans, K. F., and G. L. Stephens (1995a), Microwave radiative transfer through clouds composed of realistically shaped ice crystals. Part I: Single scattering properties, *J. Atmos. Sci.*, *52*(11), 2041–2057.
- Evans, K. F., and G. L. Stephens (1995b), Microwave radiative transfer through clouds composed of realistically shaped ice crystals. Part II: Remote sensing of ice clouds, *J. Atmos. Sci.*, *52*(11), 2058–2072.
- Evans, K. F., J. Turk, T. Wong, and G. L. Stephens (1995), A bayesian approach to microwave precipitation profile retrieval, *J. Appl. Meteorol.*, *34*, 260–279.
- Evans, K. F., S. J. Walter, A. J. Heymsfield, and G. M. McFarquhar (2002), Sub-millimeter-wave cloud ice radiometer: Simulations of retrieval algorithm performance, *J. Geophys. Res.*, *107*(D3), AAC 2–1 – 2–21.

- Evans, K. F., M. D. Vaneck, C. Lee, and J. R. Wang (2003), Sub-millimetre-wave remote sensing of cirrus anvil during CRYSTAL-FACE, in *EGS-AGU-EUG Joint Assembly*, EGS.
- Evans, K. F., J. R. Wang, P. E. Racette, G. Heymsfield, and L. Li (2005), Ice cloud retrievals and analysis with the Compact Scanning Submillimeter Imaging Radiometer and the cloud radar system during CRYSTAL-FACE, *J. Appl. Meteorol.*, *44*, 839–859.
- Feist, D. G. (2004), The BERNese Atmospheric Multiple CATalog access tool (BEAMCAT): a tool for users of popular spectral line catalogs, *J. Quant. Spectrosc. Ra.*, *85*(1), 57–97.
- Ferraro, R. R. (1997), SSM/I derived global rainfall estimates for climatological applications, *J. Geophys. Res.*, *102*, 16,715–16,735.
- Ferraro, R. R., F. Weng, N. C. Grody, and L. Zhao (2000), Precipitation characteristics over land from the NOAA-15 AMSU sensor, *Geophys. Res. Lett.*, *27*, 2669–2672.
- Ferraro, R. R., P. Pellegrino, S. J. Kusselson, M. Turk, and S. Kidder (2002), Validation of SSM/I and AMSU derived tropical rainfall potential (TRaP) during the 2001 Atlantic hurricane season. NOAA technical report NESDIS, *Tech. Rep. 105*, U.S. Department of Commerce, NOAA.
- Field, P. R., R. J. Hogan, P. R. A. Brown, A. J. Illingworth, T. W. Choulaton, and R. J. Cotton (2005), Parameterization of ice-particle distributions for mid-latitude stratiform cloud, *Q. J. Roy. Meteor. Soc.*, *131*, 1997–2017.
- Gasiewski, A. J., J. W. Barrett, P. G. Bonanni, and D. H. Staelin (1990), Aircraft-based radiometric imaging of tropospheric temperature and precipitation using the 118.75-GHz oxygen resonance, *J. Appl. Meteorol.*, *29*, 620–632.
- Glickman, T. S. (Ed.) (2000), *Glossary of Meteorology*, 2nd ed., American Meteorological Society, Allen Press.
- Grody, N. C. (1991), Classification of snow cover and precipitation using the special sensor microwave imager, *J. Geophys. Res.*, *96*(D4), 7423–7435.
- Hess, P., and H. Brezowsky (1977), Katalog der Grosswetterlagen Europas, *Berichte des Deutschen Wetterdienstes 113(15)*, Deutscher Wetter Dienst (DWD), Offenbach am Main.
- Heymsfield, A. J., and M. Kajikawa (1986), An improved approach to calculating terminal velocities of plate-like crystals and graupel, *J. Atmos. Sci.*, *44*, 1088–1099.
- Hollinger, J. R., C. Lo, G. Poe, R. Savage, and J. Pierce (1987), *Special Sensor Microwave Imager User's Guide*, Naval Research Laboratory.

- Huffman, G. J., et al. (1997), The Global Precipitation Climatology Project (GPCP) combined precipitation data set, *B. Am. Meteorol. Soc.*, 78(1), 5–20.
- Janssen, M. A. (Ed.) (1993), *Atmospheric remote sensing by microwave radiometry*, John Wiley & sons, inc.
- Jiménez, C., S. A. Bühler, B. Rydberg, P. Eriksson, and K. F. Evans (2007), Performance simulations for a submillimetre-wave cloud ice satellite instrument, *Q. J. Roy. Meteor. Soc.*, 133, 129–149.
- Karbou, F., C. Prigent, L. Eymard, and J. Pardo (2005), Microwave land emissivity calculations using AMSU-A and AMSU-B measurements, *IEEE T. Geosci. Remote*, 43(5), 948–959.
- Kessler, E. (1969), On the distribution and continuity of water substance in atmospheric circulation, *Meteorol. Monogr.*, 10(32), 84 pp.
- Khain, A. P., and I. L. Sednev (1996), Simulation of precipitation formation in the eastern mediterranean coastal zone using a spectral microphysics cloud ensemble model, *Atmos. Res.*, 43, 77–110.
- Kim, M. J., G. M. Skofronick-Jackson, and J. A. Weinman (2004), Intercomparison of millimeter-wave radiative transfer models, *IEEE T. Geosci. Remote*, 42(9), 1882–1890.
- Kim, M. J., M. S. Kulie, C. O’Dell, and R. Bennartz (2007), Scattering of ice particles at microwave frequencies: A physically based parameterization, *J. Appl. Meteorol.*, 46, 615–633.
- Klein, M., and A. J. Gasiewski (2000), Nadir sensitivity of passive millimeter and submillimeter wave channels to clear air temperature and water vapor variations, *J. Geophys. Res.*, 105(D13), 17,481–17,511.
- Kummerow, C. (2001), On the accuracy of the Eddington approximation for radiative transfer in the microwave frequencies, *J. Geophys. Res.*, 98, 2757–2765.
- Kummerow, C., and L. Giglio (1994), A passive microwave technique for estimating rainfall and vertical structure information from space. Part I: Algorithm description, *J. Appl. Meteorol.*, 33, 3–18.
- Kummerow, C., W. Barnes, T. Kozu, J. Shine, and J. Simpson (1998), The Tropical Rainfall Measuring Mission (TRMM) sensor package, *J. Atmos. Ocean. Tech.*, 15, 808–816.
- Kummerow, C., et al. (2001), The evolution of the Goddard PROFiling algorithm (GPROF) for rainfall estimation from passive microwave sensors, *J. Appl. Meteorol.*, 39, 1801–1820.

- Kummerow, C. D., R. A. Mack, and I. M. Hakkarinen (1989), A self-consistency approach to improve microwave rainfall estimates from space, *J. Appl. Meteorol.*, *39*, 1801–1820.
- Kuphaldt, T. R. (2007), Fundamentals of electrical engineering and electronics.
- Lafore, J.-P., et al. (1998), The Méso-NH atmospheric simulation system. Part I: Adiabatic formulation and control simulations, *Ann. Geophys.*, *16*, 90–109.
- Lambrigsten, B. H., W. J. Wilson, and A. B. Tanner (2004), GeoSTAR - a microwave sounder for GOES-R, in *IEEE IGARSS 2004*, vol. 2, pp. 777–780, IEEE Geoscience and Remote Sensing Society (IGARSS), Anchorage, Alaska.
- Lamkaouchi, K., A. Balana, and W. J. Ellison (1997), New permittivity data for sea water (30-100 GHz), *Tech. rep.*, ESA, extension to ESA report 11197/94/NL/CN.
- Levizzani, V., et al. (2001), EURAINSAT - Looking into the future of satellite rainfall estimations, in *Proc. 2001 EUMETSAT Meteorological Satellite Data Users' Conf.*, pp. 375–384, Antalya.
- Liebe, H. J., T. Manabe, and G. A. Hufford (1989), Millimeter-wave attenuation and delay rates due to fog/cloud conditions, *IEEE T. Antenn. Propag.*, *37*, 1617–1623.
- Liebe, H. J., G. A. Hufford, and M. G. Cotton (1993), Propagation modelling of moist air and suspended water/ice particles at frequencies below 1000 GHz, in *Proceedings AGARD 52nd Specialists Meeting of the Electromagnetic Wave Propagation Panel*, pp. 3-1-3-10, AGARD, Palma de Mallorca, Spain.
- Lin, Y.-L., R. D. Farley, and H. D. Orville (1983), Bulk parameterization of snow field in a cloud model., *J. Appl. Meteorol.*, *22*, 1065–1092.
- Liu, G. (2004), Approximation of single scattering properties of ice and snow particles for high microwave frequencies, *J. Atmos. Sci.*, *61*, 2441–2456.
- Liu, G., and J. A. Curry (2000), Determination of ice water path and mass median particle size using multichannel microwave measurements, *J. Appl. Meteorol.*, *39*, 1318–1329.
- Liu, Q., and C. Simmer (1996), Polarization and intensity in microwave radiative transfer, *Beitr. Phys. Atmos.*, *69*(4), 535–545.
- Liu, Q., C. Simmer, and E. Ruprecht (1991), A general analytic expression of the radiation source function for emitting and scattering media within the matrix operator method, *Beitr. Phys. Atmos.*, *64*, 73–82.
- Locatelli, J. D., and P. V. Hobbs (1974), Fall speeds and masses of solid precipitation particles, *J. Geophys. Res.*, *79*, 2185–2197.

- Manabe, T., H. J. Liebe, and G. A. Hufford (1987), Complex permittivity of water between 0 and 30 THz, in *IEEE conference digest 12th International Conference on Infrared and Millimeter Waves*, pp. 229–230, IEEE, Orlando, Florida.
- Mätzler, C. (Ed.) (2006), *Thermal microwave radiation: Applications for remote sensing, Electromagnetic waves*, vol. 52, The Institute of Engineering and Technology, London, United Kingdom.
- McCollum, J. R., and R. R. Ferraro (2003), Next generation of NOAA/NESDIS TMI, SSM/I, and AMSR-E microwave land rainfall algorithms, *J. Geophys. Res.*, 108(D8), 8382.
- McCumber, M., W.-K. Tao, J. Simpson, R. Penc, and S. T. Soong (1991), Comparison of ice-phase microphysical parameterization schemes using numerical simulations of tropical convection, *J. Appl. Meteorol.*, 30, 985–1004.
- Mech, M., S. Crewell, I. Meirold-Mautner, C. Prigent, and J.-P. Chaboureau (2007), Information content of millimeter-wave observations for hydrometeor properties in mid-latitudes, *IEEE T. Geosci. Remote*, 45(7), 2287–2299.
- Meirold-Mautner, I., C. Prigent, J. R. Pardo, J.-P. Chaboureau, J.-P. Pinty, M. Mech, and S. Crewell (2007), Radiative transfer simulations using mesoscale cloud model outputs and comparisons with passive microwave and infrared satellite observations for mid-latitude situations, *J. Atmos. Sci.*
- Melsheimer, C., et al. (2005), Intercomparison of general purpose clear sky atmospheric radiative transfer models for the millimeter/submillimeter spectral range, *Radio Sci.*, 40(RS1007).
- Mie, G. (1908), Beiträge zur Optik trüber Medien speziell kolloidaler Metallösungen, *Ann. Phys.*, 25, 377–445.
- Mishchenko, M. I. (1993), Light scattering by size-shape distributions of randomly oriented axially symmetric particles of a size comparable to a wavelength, *ao*, 32(24), 4652–4666.
- Mishchenko, M. I., L. D. Travis, and D. W. Mackowski (1996), T-matrix computations of light scattering by non-spherical particles: A review, *J. Quant. Spectrosc. Ra.*, 55, 535–575.
- Mishchenko, M. I., L. D. Travis, and A. A. Lacis (Eds.) (2002), *Scattering, absorption and emission of light by small particles*, Academic Press.
- Mishchenko, M. I., L. Liu, and G. Videen (2007), Conditions of the applicability of single-scattering approximations, *Optical Express*, 15(12), 7522–7527.
- Mugnai, A. (2003), EGPM - the proposed European contribution to the Global Precipitation Measurement (GPM) mission, *Geophys. Res. Abstr.*, 5, 12,550.

- Mugnai, A., E. A. Smith, and G. J. Tripoli (1993), Foundation for statistical-physical precipitation retrieval from passive microwave satellite measurements. Part II: Emission-source and generalized weighting function properties of a time-dependent cloud-radiation model, *J. Appl. Meteorol.*, *32*, 17–39.
- Mugnai, A., et al. (2005), Development of an end-to-end tool to simulate the performance of the European contribution to the GPM mission (EGPM-simulator), *Tech. Rep. ESA contract No. 18101/04/NL/GS*, ESA, ESTEC, Netherlands.
- Olson, W. S., et al. (2006), Precipitation and latent heating distributions from satellite passive microwave radiometry. Part I: Improved method and uncertainties, *J. Appl. Meteorol. Clim.*, *45*, 702–720.
- Pardo, J. R., J. Cernicharo, and E. Serabyn (2001), Atmospheric Transmission at Microwaves (ATM): An improved model for mm/submm applications, *IEEE T. Antenn. Propag.*, *49*(12), 2683–1694.
- Petty, G. W. (2006), *A first course in atmospheric radiation*, 2nd ed., Sundog publishing, Madison, Wisconsin.
- Pinty, J.-P., and P. Jabouille (1998), A mixed-phase cloud parameterization for use in a mesoscale non-hydrostatic model: simulations of a squall line and of orographic precipitations, in *Proceedings of the AMS conference on cloud physics*, American Meteorological Society, Everett, Washington.
- Prabhakara, C., G. Dalu, G. L. Liberti, J. J. Nucciarone, and R. Suhasini (1992), Rainfall estimation over ocean from SMMR and SSM/I microwave data, *J. Appl. Meteorol.*, *31*, 532–551.
- Prigent, C., W. B. Rossow, and E. Matthews (1997), Microwave land surface emissivities estimated from SSM/I observations, *J. Geophys. Res.*, *102*, 21,867–21,890.
- Prigent, C., I. Meirold-Mautner, F. Aires, C. J. Walden, N. Viltard, and O.-Z. Zanifé (2005), Study of the potential of sub-millimeter wave observations for precipitation retrieval, *Tech. rep.*, ESTEC.
- Purcell, E. M., and C. R. Pennypacker (1973), Scattering and absorption of light by non spherical dielectric grains, *Astron. J.*, *186*, 705–714.
- Racette, P., R. F. Adler, J. R. Wang, A. J. Gasiewski, D. M. Jackson, and D. S. Zacharias (1996), An airborne millimetre-wave imaging radiometer for cloud, precipitation and atmospheric water vapour studies, *J. Atmos. Ocean. Tech.*, *13*, 610–619.
- Richard, E., S. Cosma, P. Tabary, J.-P. Pinty, and M. Hagen (2003), High-resolution numerical simulations of the convective system observed in the Lago Maggiore area on 17 september 1999 (MAP IOP 2a), *Q. J. Roy. Meteor. Soc.*, *129*, 543–563.

- Rizzi, R., P. Bauer, S. Crewell, M. Leroy, C. Mätzler, W. P. Menzel, B. Ritter, J. E. Russel, and A. Thoss (2006), Cloud, Precipitation and large scale Land surface imaging (CPL) observational requirements for meteorology, hydrology, and climate, [http://www.eumetsat.int/Home/Main/What\\_We\\_Do/Satellites/Future\\_Satellites/Post-EPS/index.htm](http://www.eumetsat.int/Home/Main/What_We_Do/Satellites/Future_Satellites/Post-EPS/index.htm), EUMETSAT position paper, version 1.K.
- Robel, J. (2006), *NOAA KLM User's Guide*, <http://www.ncdc.noaa.gov/oa/pod-guide/ncdc/docs/klm/index.htm>.
- Roberti, L., J. Haferman, and C. Kummerow (1994), Microwave radiative transfer through horizontally inhomogeneous precipitating clouds, *J. Geophys. Res.*, *99*, 16,707–16,718.
- Rossow, W. B., and R. A. Schiffer (1999), Advances in understanding clouds from ISCCP, *B. Am. Meteorol. Soc.*, *80*, 2261–2287.
- Saunders, R., M. Matricardi, and P. Brunel (1999), An improved fast radiative transfer model for assimilation of satellite radiance observations, *Q. J. Roy. Meteor. Soc.*, *125*, 1407–1425.
- Seo, E.-K., and M. I. Biggerstaff (2006), Impact of cloud model microphysics on passive microwave retrievals of cloud properties. Part II: Uncertainty in rain, hydrometeor structure, and latent heating retrievals, *J. Appl. Meteorol. Clim.*, *45*.
- Sihvola, A. (1989), Self-consistency aspects of dielectric mixing theories, *IEEE T. Geosci. Remote*, *27*(4), 403–415.
- Simmer, C. (2004), *Satellitenfernerkundung hydrologischer Parameter der Atmosphäre mit Mikrowellen*, Verlag Dr. Kovač.
- Skofronick-Jackson, G. M., A. J. Gasiewski, and J. R. Wang (2002), Influence of microphysical cloud parameterizations on microwave brightness temperatures, *IEEE T. Geosci. Remote*, *40*(1), 187–196.
- Skofronick-Jackson, G. M., M.-J. Kim, J. A. Weinman, and D.-E. Chang (2004), A physical model to determine snowfall over land by microwave radiometry, *IEEE T. Geosci. Remote*, *42*(5), 1047–1058.
- Smith, E. A., A. Mugnai, H. J. Cooper, G. J. Tripoli, and X. Xiang (1992), Foundation for statistical-physical precipitation retrieval from passive microwave satellite measurements. Part I: Brightness-temperature properties of a time-dependent cloud-radiation model, *J. Appl. Meteorol.*, *31*, 506–531.
- Smith, E. A., P. Bauer, F. S. Marzano, C. D. Kummerow, D. McKague, A. Mugnai, and G. Panegrossi (2002), Intercomparison of microwave radiative transfer models for precipitating clouds, *IEEE T. Geosci. Remote*, *40*, 541–549.

- Sreerekha, T. R., et al. (2005), Development of a RT model for frequencies between 200 and 1000 GHz, *Final report*, ESTEC, contract No. 17632/03/NL/FF.
- Staelin, D. H., A. J. Gasiewski, J. P. Kerekes, M. W. Shields, and F. J. Solman III (1998), Concept proposal for a GEostationary Microwave (GEM) observatory, prepared for the NASA/NOAA Advanced Geostationary Sensor (AGS) Program, MIT, Lexington Mass.
- Steppler, J., G. Doms, U. Schättler, H. W. Bitzer, A. Gassmann, U. Damrath, and G. Gregoric (2003), Meso-gamma scale forecasts using the nonhydrostatic model LM, *Meteorol. Atmos. Phys.*, *82*, 75–96.
- Tanner, A. B., et al. (2004), Prototype development of a Geostationary Synthetic Thinned Aperture Radiometer, GeoSTAR, in *IEEE IGARSS 2004*, IEEE Geoscience and Remote Sensing Society (IGARSS), Pasadena, CA : Jet Propulsion Laboratory, National Aeronautics and Space Administration, 2004.
- Tanner, A. B., et al. (2007), Initial results of the Geostationary Synthetic Thinned Array Radiometer (GeoSTAR) demonstrator instrument, *IEEE T. Geosci. Remote*, *45*(7), 1947–1957.
- Tiedke, M. (1989), A comprehensive mass flux scheme for cumulus parameterization in large-scale models, *Mon. Wea. Rev.*, *117*, 1779–1799.
- Tripoli, G. J., C. M. Medaglia, S. Dietrich, A. Mugnai, G. Panegrossi, S. Pinori, and E. A. Smith (2005), The 9-10 November 2001 Algerian flood: A numerical study, *Bull. Amer. Meteor. Soc.*, *86*, 1229–1235.
- Tsang, L., J. A. Kong, and K. Ding (1985), *Theory of microwave remote sensing*, Wiley-Interscience, New York.
- Ulbrich, U., T. Brücher, A. H. Fink, G. C. Leckebusch, A. Krüger, and J. G. Pinto (2003), The Central European floods of 2002: Part II: Synoptic causes and considerations with respect to climate change, *Weather*, *58*(11), 434–442.
- Wang, J. R., G. Liu, J. D. Spinhirne, P. Racette, and W. D. Hart (2001), Observations and retrievals of cirrus cloud parameters using multichannel millimeter-wave radiometric measurements, *J. Geophys. Res.*, *106*(D14), 15,251–15,263.
- Warren, S. G. (1984), Optical constants of ice from the ultraviolet to the microwave, *Appl. Opt.*, *23*, 1206–1225.
- Waterman, P. C. (1971), Symmetry, unitarity, and geometry in electromagnetic scattering, *Phys. Rev. D*, *3*(4), 825–839.
- Wiedner, M., C. Prigent, J. Pardo, O. Nuissier, J.-P. Chaboureaud, J.-P. Pinty, and P. Mascart (2004), Modeling of passive microwave responses in convective situations using output from mesoscale models: Comparison with TRMM/TMI satellite observations, *J. Geophys. Res.*, *109*, 1–13.

- 
- Wilheit, T. T., A. T. C. Chang, M. S. V. Rao, E. B. Rodgers, and J. S. Theon (1977), A satellite technique for quantitatively mapping rainfall rates over oceans, *J. Appl. Meteorol.*, *16*, 551–560.
- WMO (1992), *International meteorological vocabulary*, 2nd ed., 784 pp., Secretariat of World Meteorological Organization.
- Zängl, G. (2004), Numerical simulations of the 12-13 August 2002 flooding event in eastern Germany, *Q. J. Roy. Meteor. Soc.*, *130*, 1921–1940.



# Danksagung

The field of remote sensing of the atmosphere was not of my interest until I have talked the first time to Prof. Dr. Susanne Crewell. Thanks for inspiring me to work on that interesting field and for supervising me throughout the years. Thanks as well to Dr. Ulrich Löhnert for the discussions on the interaction between passive microwaves and the atmosphere. Special thanks go to Prof. Dr. Clemens Simmer and to Dr. Harald Czekala as the fathers of MWMOD for their help on the code and the discussions we had on radiative transfer.

I thank the French group at l'Observatoire de Paris and especially Dr. Catherine Prigent for providing me with the basic code to couple the models and the very fruitful discussions throughout my studies. Thank goes as well to Dr. Jean-Pierre Chaboureau for providing the Méso-NH model results and to Thorsten Reinhardt for his help on the COSMO-DE model.

I would like to thank Kerstin Ebell and Christoph Selbach for proof-reading. Without their help it would not have been possible to complete this thesis in time. Jan Schween I have to thank for his help on mathematics and the discussions we had on good programming style.

Special thanks go to my friends. Without having a great time with them aside my work, life wouldn't be that much fun. Especially the discussions with Phia on *believing in oneself* resolved all doubt.

Last but not least I'd like to thank my family for the support they gave to me throughout my life.



# Erklärung

Ich versichere, dass ich die von mir vorgelegte Dissertation selbständig angefertigt, die benutzten Quellen und Hilfsmittel vollständig angegeben und die Stellen der Arbeit - einschließlich Tabellen, Karten und Abbildungen -, die anderen Werken im Wortlaut oder dem Sinn nach entnommen sind, in jedem Einzelfall als Entlehnung kenntlich gemacht habe; dass diese Dissertation noch keiner anderen Fakultät oder Universität zur Prüfung vorgelegen hat; dass sie - abgesehen von unten angegebenen Teilpublikationen - noch nicht veröffentlicht worden ist sowie, dass ich eine solche Veröffentlichung vor Abschluß des Promotionsverfahrens nicht vornehmen werde. Die Bestimmungen dieser Promotionsordnung sind mir bekannt. Die von mir vorgelegte Dissertation ist von Prof. Dr. S. Crewell betreut worden.

Köln, den 3. Januar 2008

Mario Mech

## Teilveröffentlichungen

CHABOUREAU, J.-P., N. SÖHNE, J.-P. PINTY, I. MEIROLD-MAUTNER, E. DEFER, C. PRIGENT, J. R. PARDO, M. MECH, AND S. CREWELL, 2008: *A midlatitude cloud database validated with satellite observation*, *J. Atmos. Sci.*, *accepted*.

MECH, M., S. CREWELL, I. MEIROLD-MAUTNER, C. PRIGENT, AND J.-P. CHABOUREAU, 2007: *Information content of millimeter observations for hydrometeor properties in mid-latitudes*, *IEEE Trans. Geosci. Remote Sens.*, **45**, 2287-2299.

MEIROLD-MAUTNER, I., C. PRIGENT, E. DEFER, J. R. PARDO, J.-P. CHABOUREAU, J.-P. PINTY, M. MECH, AND S. CREWELL, 2007: *Radiative transfer simulations using mesoscale cloud model outputs and comparisons with passive microwave and infrared satellite observations for mid-latitude situations*, *J. Atmos. Sci.*, **64**, 1550-1568.



# Lebenslauf

## Lebenslauf

### Persönliche Angaben

Name: Mario Mech  
Anschrift: Aquinostr. 18, 50670 Köln  
Geburtstag: 27. 10. 1974  
Geburtsort: Lahr  
Familienstand: ledig  
Staatsangehörigkeit: deutsch

### Schulbildung

08/1981–07/1985: Grundschule in Seelbach  
08/1985–06/1994: Max-Planck Gymnasium in Lahr  
21. Juni 1994: Abitur am Max-Planck Gymnasium in Lahr

### Zivildienst

01/1995–01/1996: Zivildienst in der individuellen Schwerstbehindertenbetreuung bei der Arbeiterwohlfahrt in Lahr

### Studium

10/1996–07/2002: Studium der Meteorologie an der Ludwig-Maximilians-Universität München  
08. Juli 2002: Meteorologiediplom der Ludwig-Maximilians-Universität München  
Thema der Diplomarbeit: "Modellierung von UV-Strahlung auf Empfänger unterschiedlicher Orientierung"  
seit 03/2004: Promotionsstudium in Meteorologie

## **Berufliche Tätigkeiten**

02/1999–07/2002: Stud. Hilfskraft am Meteorologischen Institut der Universität München

08/2002–02/2004: Wiss. Angestellter am Meteorologischen Institut der Universität München

03/2004–07/2006: Wiss. Angestellter am Meteorologischen Institut der Universität Bonn und dem Meteorologischen Institut der Universität München

seit 08/2006: Wiss. Angestellter am Institut für Geophysik und Meteorologie der Universität zu Köln

Köln, 3. Januar 2008